

ABSTRACT

MITCHELL, EDWIN COLEMAN. Improving and Exploiting Analytical Tools for Real Time Quantitative Studies in Complex Matrices. (Under the direction of Dr. Leslie A. Sombers).

Electrochemical techniques have been used for many years to provide answers to fundamental research questions in challenging environments. For example, coupling fast-scan cyclic voltammetry (FSCV) with carbon-fiber microelectrodes (CFMEs) was groundbreaking in the field of neuroscience because it became possible to directly measure chemical release events occurring in the brain in real time. Over the past twenty years, characterization of FSCV at CFMEs has enabled groundbreaking work in live brain tissue, but many questions remain unanswered, often due to technological limitations. The research presented herein will contribute to the advancement of *in vivo* electrochemical techniques by chemically characterizing the carbon surface upon potential application, describing novel strategies to manipulate the geometry of the electrode, and by investigating complex potential waveforms applied to the electrode.

Carbon fibers are the preferred microelectrode material for *in vivo* electrochemical studies due to a number of advantages when compared to metal electrodes. The electrochemical performance of carbon fibers is dependent on their surface chemistry. To further understand the relationship between carbon surface chemistry and electrochemical performance, Raman spectroscopy was implemented to characterize the chemical nature of the surface of disk-CFMEs in response to electrical potentials. It was found that

preconditioning the carbon surface introduced beneficial microstructural alterations. Static potential waveforms were more effective than dynamic potential waveforms. In addition, this work demonstrates that the carbon microstructure is dynamic in nature and that it quickly responds to applied electrochemical potentials.

Single cells are commonly used as model systems when studying exocytosis. The most common approach has been to couple amperometry with a disk-CFME positioned directly on top of the cell, which allows for the measurement of individual vesicular release events. In this work, a controllable plasma-etching procedure was used to create a CFME with a recessed cavity geometry that was implemented to detect exocytotic events at chromaffin cells. When compared to traditional disk-CFME, the cavity-CFME were able to detect more molecules per release event, suggesting that traditional disk-CFMEs may underestimate vesicular quantal size.

Due to geometrical limitations of the electrode and the challenging recording environment of the cytoplasm, most electrochemical measurements at single cells have been limited to the extracellular environment. In this work, a conical nanoelectrode was insulated using a novel coating procedure and employed to make intracellular chemical measurements. These unprecedented measurements served to distinguish norepinephrine and epinephrine in vesicles that lysed onto the electrode surface. This work also highlights the complementary information that can be gained from voltammetric and amperometric studies.

When analyzing data collected in the complex environment of the brain, principle component regression (PCR) has been effective for distinguishing individual chemical components that contribute to a voltammetric signal. However, PCR is inadequate for

distinguishing the voltammetric signals of hydrogen peroxide and pH shift, as the voltammograms for these species both contain significant oxidation current at ~ 1.3 V. Herein, we present a unique double waveform that can be coupled to a mathematical model to allow for identification and quantification of these two components in a mixed signal.

Overall, the work presented herein provides researchers with new information and unique tools that improve upon current FSCV and CFME technologies. Ultimately, the data presented herein will enable investigation of research questions that could not be addressed previously, due to a lack of technology. Additionally, this work will allow investigators to make more informed decisions with regard to electrode fabrication, and to draw more appropriate conclusions in data analysis.

© Copyright 2017 Edwin Coleman Mitchell

All Rights Reserved

Improving and Exploiting Analytical Tools for Real Time Quantitative Studies in Complex
Matrices

by
Edwin Coleman Mitchell

A dissertation submitted to the Graduate Faculty of
North Carolina State University
in partial fulfillment of the
requirements for the degree of
Doctor of Philosophy

Chemistry

Raleigh, North Carolina

2017

APPROVED BY:

Leslie Sombers
Committee Chair

Edmond Bowden

Gufeng Wang

Owen Duckworth

DEDICATION

This work is dedicated to my Mom, Dad, Papa, my three children and to my wife, Katie.

It is also dedicated to my Granny, who would have loved to have seen me make it this far.

BIOGRAPHY

Edwin Mitchell was born in Fayetteville, NC on October 3, 1989 to his parents Terry and Deborah Mitchell. He attended Cape Fear High School where he graduated in 2007. Edwin completed his undergraduate studies at the University of North Carolina at Chapel Hill where he graduated with a Bachelor of Science in Chemistry in 2011. One week after graduation Edwin was married to his wife, Katie. He then began his doctoral studies at North Carolina State University in August 2011. During this time he has had three children, David, Elisabeth, and Naomi.

ACKNOWLEDGMENTS

There are many people who have helped me through this process and made it possible for me to complete this work.

I want to first thank Dr. Leslie Sombers for her support during my graduate career. I am grateful to all of the Sombers lab members for the help they have provided at various times. I am especially grateful to James Roberts and Lars Dunaway for the long hours they put in to help with culturing cells.

I want to thank Chuck Mooney with the Analytical Instrumentation Facility at NCSU who helped with SEM image collection.

I am thankful for my church family which has been helpful to both me and my wife during this time.

I never would have made it this far without the encouragement from my mom and dad to always do my best in school. Thank you for the continual help that you provide me and my family.

I especially want to thank my wife, Katie, for her patience throughout this time. This process has not always been easy, but your love and support have helped give me the energy to keep going and to make it to where I am now.

TABLE OF CONTENTS

LIST OF TABLES	xi
LIST OF FIGURES	xii
CHAPTER 1: Introduction to Voltammetric Methods Used to Monitor Neuronal Transmission and Requirements for Technique Optimization	1
1.1 Neurons and Chemical Signaling	1
1.2 Neuroscience Research Methods	3
1.3 Analytical Methodologies for Measuring Neurotransmission	4
<u>1.3.1 Electrophysiology</u>	<u>5</u>
<u>1.3.2 Microdialysis</u>	<u>6</u>
<u>1.3.3 Spectroscopic Techniques</u>	<u>7</u>
<u>1.3.4 Electrochemical Methods</u>	<u>7</u>
1.4 Fast-Scan Cyclic Voltammetry	9
1.5 Data Analysis	12
1.6 Carbon-Fiber Microelectrodes	13
1.7 Dissertation Overview	18
1.8 References	21
CHAPTER 2: Spectroelectrochemical Chemical Characterization of the Carbon Fiber Surface in Response to Electrochemical Conditioning	27
2.1 Introduction	27
2.2 Experimental Section	29

<u>2.2.1 Chemicals</u>	29
<u>2.2.2 Electrode Fabrication</u>	29
<u>2.2.3 Flow Injection</u>	30
<u>2.2.4 Electrochemical Data Acquisition</u>	30
<u>2.2.5 Surface Analysis</u>	31
<u>2.2.6 Data Analysis</u>	32
2.3 Results and Discussion	32
<u>2.3.1 Microstructural Characterization with Raman Spectroscopy</u>	32
<u>2.3.2 Dynamic and Static Waveform Potentials Alter the Carbon Surface</u>	37
<u>2.3.3 Dynamic and Static Pretreatments Differentially Affect</u> <u>Electrochemical Performance</u>	41
<u>2.3.4 Rate of Change Comparison</u>	46
<u>2.3.5 Surface Response to Alternating Static Potentials</u>	48
2.4 Conclusions	50
2.5 References	52
CHAPTER 3: Recessed Carbon-Fiber Microelectrodes for Use with Amperometry At Single Cells and FSCV in Brain Slice Preparations	57
3.1 Introduction	57
3.2 Experimental Section	60
<u>3.2.1 Chemicals</u>	60
<u>3.2.2 Microelectrode Fabrication</u>	61
<u>3.2.3 Data Acquisition</u>	61

3.2.4	<u>Fast-Scan Cyclic Voltammetry</u>	62
3.2.5	<u>Raman Spectroscopy</u>	62
3.2.6	<u>Brain Slice Preparation</u>	63
3.2.7	<u>Primary Bovine Chromaffin Cell Culture</u>	63
3.2.8	<u>Single Cell Experiments</u>	64
3.2.9	<u>Amperometry Data Acquisition and Analysis</u>	65
3.2.10	<u>Slow-Scan Cyclic Voltammetry</u>	65
3.2.11	<u>Data Analysis and Statistics</u>	66
3.3	Results and Discussion	66
3.3.1	<u>Etching Carbon-Fiber Microelectrodes</u>	66
3.3.2	<u>Controlling Cavity Depth</u>	69
3.3.3	<u>Electrochemical Characterization</u>	70
3.3.4	<u>Monitoring Neurotransmitter Release in Live Tissue</u>	78
3.3.5	<u>Monitoring Individual Exocytotic Events at Single Cells</u>	80
3.4	Conclusions	84
3.5	References	86
 CHAPTER 4: Intracellular Chemical Measurements Using Nanocone		
	Electrodes	92
4.1	Introduction	92
4.2	Experimental Section	95
4.2.1	<u>Chemicals</u>	95
4.2.2	<u>Electrode Fabrication</u>	95

4.2.3	<u>Flow Injection</u>	96
4.2.4	<u>Electrochemical Data Acquisition</u>	97
4.2.5	<u>Primary Bovine Chromaffin Cell Culture</u>	98
4.2.6	<u>Single Cell Experiments</u>	99
4.2.7	<u>Data Analysis</u>	99
4.3	Results and Discussion	99
4.3.1	<u>Electrode Fabrication</u>	99
4.3.2	<u>Electrochemical Characterization</u>	106
4.3.3	<u>Intracellular Voltammetry</u>	112
4.4	Conclusions	119
4.5	References	120
 CHAPTER 5: A Double Voltammetric Waveform for Distinguishing Overlapping		
	Signals from pH and Hydrogen Peroxide	123
5.1	Introduction	123
5.2	Experimental Section	126
5.2.1	<u>Chemicals</u>	126
5.2.2	<u>Electrode Fabrication</u>	126
5.2.3	<u>Flow Injection</u>	127
5.2.4	<u>Electrochemical Data Acquisition</u>	127
5.2.5	<u>InVivo Data Collection</u>	128
5.2.6	<u>Data Analysis</u>	129
5.3	Results and Discussion	129

5.3.1 <u>H₂O₂ and ΔpH Investigated with Single Waveform Cyclic Voltammetry</u>	129
5.3.2 <u>Cyclic Voltammetry with a Double Waveform</u>	132
5.3.3 <u>Constructing the Training Set</u>	134
5.3.4 <u>pH Subtraction Extended to <i>In vivo</i> Data</u>	137
5.4 Conclusions	139
5.5 References	141
CHAPTER 6: Summary and Outlook	143
APPENDICES	146
APPENDIX A: Supplemental Information to Chapter 3	147
A.1 Supporting Information	147
APPENDIX B: Characterization of Abiotic Manganese Dioxide Reactivity	
Using Voltammetry	149
B.1 Introduction	149
B.2 Experimental Section	151
<u>B.2.1 Chemicals</u>	151
<u>B.2.2 Preparation of Manganese Minerals</u>	151
<u>B.2.3 Electrochemical Data Acquisition</u>	151
<u>B.2.4 Data Analysis</u>	152
B.3 Results and Discussion	152
<u>B.3.1 Preparing the Electrode for Analysis</u>	152

<u>B.3.2 Verification of the MnO₂ Voltammetric Signal</u>	155
<u>B.3.3 Zinc and Arsenic Doped MnO₂</u>	157
<u>B.3.4 Electron Transfer Rate Measurements</u>	159
B.4 Conclusions	162
B.5 References	164

LIST OF TABLES

Table 2.1	Microcrystallite Dimensions for the Different States of the P-55	
	Carbon Fiber	36
Table 2.2	Peak-to-Peak Separation for the Detection of 2 μ M Dopamine.....	45
Table B.1	Calculated electron transfer rates for the reduction of abiotic manganese oxides.....	162
Table B.2	Average manganese oxidation numbers for abiotic manganese oxides	162

LIST OF FIGURES

Figure 1.1	Cellular communication with neurons	3
Figure 1.2	Diagram depicting process for background subtracted FSCV	10
Figure 1.3	Diagram depicting process for constructing color plots used for analysis	13
Figure 1.4	Images of commonly used carbon-fiber microelectrodes	15
Figure 2.1	Experimental design	33
Figure 2.2	Polishing increases disorder on carbon surface.....	35
Figure 2.3	Dynamic and static conditioning paradigms elicit distinct changes to the carbon surface.....	37
Figure 2.4	Surface changes can be visualized using SEM	40
Figure 2.5	Conditioning affects electrochemical performance.....	41
Figure 2.6	Electrochemical conditioning does not increase electrode surface area ...	44
Figure 2.7	Conditioning alters electrochemical response for ascorbic acid	46
Figure 2.8	Static conditioning with positive potentials rapidly changes the carbon surface	47
Figure 2.9	Carbon surface changes are dynamic	49
Figure 3.1	Fabrication of cavity electrodes	68
Figure 3.2	Cavity electrodes	70
Figure 3.3	Electrochemical characterization of recessed carbon-fiber microelectrodes	73

Figure 3.4	Field Emissions SEM and Raman imaging on plasma-etched electrodes.....	75
Figure 3.5	Voltammetric estimation of surface area.....	78
Figure 3.6	Diminished mass transport in live tissue.....	79
Figure 3.7	Amperometric recording of individual exocytotic events at single bovine chromaffin cells.....	81
Figure 4.1	Wet etching provides a facile means for producing conical electrodes.....	101
Figure 4.2	Electrodes are masked and insulated.....	103
Figure 4.3	Scanning electron micrograph of an insulated conical carbon fiber.....	104
Figure 4.4	Wax coating was removed with repeated application of waveform.....	106
Figure 4.5	Electrodes with polymer and wax bilayer coating show a stable response.....	107
Figure 4.6	Electrochemical characterization of dopamine at conical electrodes.....	108
Figure 4.7	Conical electrodes detect individual exocytotic events at single cells.....	109
Figure 4.8	Insertion of an electrode into a single cell.....	110
Figure 4.9	Amperometric detection of intracellular vesicle content.....	111
Figure 4.10	Intracellular voltammetry.....	113
Figure 4.11	Norepinephrine and epinephrine can be distinguished voltammetrically.....	114

Figure 4.12	Chemical identification and quantification of intracellular vesicle content	117
Figure 4.13	Intracellular norepinephrine and epinephrine contents	118
Figure 5.1	Characteristic colorplots and voltammograms for H ₂ O ₂ and ΔpH.....	130
Figure 5.2	Current is linearly related to the amount of species present.....	131
Figure 5.3	Disambiguating H ₂ O ₂ and ΔpH with a double waveform.....	134
Figure 5.4	Building a training set	136
Figure 5.5	Verification of pH subtraction model with <i>in vivo</i> data	139
Figure A.1	Plasma etching apparatus	147
Figure A.2	Cavity carbon-fiber electrodes can be created using FSCV.....	148
Figure B.1	Diagram depicting the process used to prepare the electrode for analysis of MnO ₂	154
Figure B.2	Electrochemical measurements of manganese oxides.....	155
Figure B.3	Current increases linearly with surface coverage.....	156
Figure B.4	Reductive current increases linearly with applied scan rate.....	157
Figure B.5	Voltammetry of metal doped manganese oxides	158
Figure B.6	Peak potential varies with scan rate	160

CHAPTER 1

Introduction to Voltammetric Methods Used to Monitor Neuronal Transmission and Requirements for Technique Optimization

1.1 Neurons and Chemical Signaling

Our understanding of how the nervous system works has come a long way from the days of Cajal, who showed us that the brain is composed of individual cells which are called neurons.¹ We have since come to recognize the brain as the most important organ in our body as it dictates everything from how we move and communicate to how we learn and perceive the world around us. The brain functions primarily through a complex system of electrical and chemical signaling pathways that when altered can modify behavior in significant ways.^{2, 3} There have been many significant advances over the years toward helping us better understand how the brain functions, but we are still woefully lacking a clear understanding of the molecular mechanisms that underlie many neurodegenerative diseases.⁴ As the average age of the population continues to increase⁵ and neurological disorders continue to appear in younger populations⁶, it is clear why it is imperative that we continue to seek a better understanding of how the brain functions.

Of course, the task of understanding the details behind brain functionality is not simple. The human brain contains approximately 100 billion neurons, which are the fundamental cellular unit composing the nervous system.⁷ The basic components of a neuron are illustrated in Figure 1.1. The neuron is a specialized cell consisting of the soma,

dendrites, and axon. The axon from one neuron projects to other neurons where they meet at a junction called the synapse. There are trillions of synapses in the human brain and they can form between the axon of one neuron and either the soma or dendrites of another neuron.⁸ It is at synapses where signals are propagated from one cell to another.

Signal propagation through neurons occurs when the cell receives an electrical impulse called an action potential.⁹ Action potentials are formed when ions cross the cell membrane and cause a depolarization of the neuron. Once an action potential begins it travels down the axon to its terminal region. It is at this point that there is an influx of calcium via the opening of calcium channels and chemical messengers packaged in vesicles are released across the membrane through a process called exocytosis. These released chemicals are referred to as neurotransmitters. Once released into the synaptic cleft the neurotransmitters can bind to receptors on the post-synaptic neuron in order to transmit a specific signal. Neurotransmitters can also be reuptaken into the pre-synaptic cell where they can be repackaged in vesicles, enzymatically degraded, or diffuse into the extracellular space.

This dissertation is centered on the advancement of electrochemical techniques and is focused largely on detecting molecules such as dopamine, which is electroactive. The most widely studied neurotransmitter over the years has been dopamine, which has been implicated in a large variety of behaviors including reward and movement. Despite the attention that has been given to dopamine, there are a large number of neurotransmitters and they can range from small molecules to large peptides.

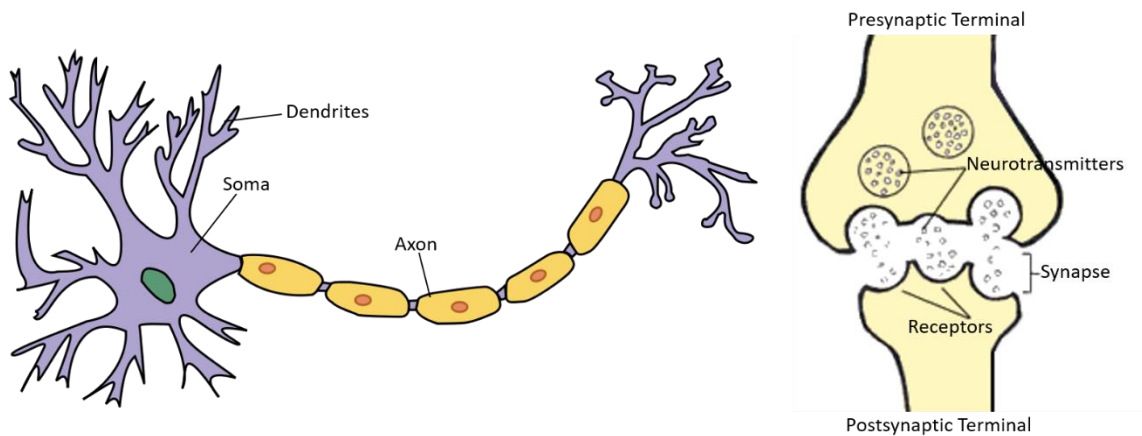


Figure 1.1 Cellular communication with neurons. A neuron is shown with dendrite and axon projections along with a presynaptic and postsynaptic terminal forming a synapse. Vesicles in the terminal of the presynaptic neuron release their contents into the synaptic cleft where they can subsequently bind with receptors on the postsynaptic neuron. (https://commons.wikimedia.org/wiki/Neuron#/media/File:Derived_Neuron_schema_with_no_labels.svg; https://commons.wikimedia.org/wiki/File:Synapse_blank.png)

1.2 Neuroscience Research Methods

It would be ideal if neuroscience research could be easily conducted in human subjects, but there are obvious barriers that limit this kind of work. Research done with humans almost always has to be noninvasive because of the danger associated with inserting sensors into brain tissue. As a means of overcoming this challenge, many researchers opt to use animal models. Animal models can mimic a variety of human conditions and do not carry the same ethical concerns with working on human subjects. With animal models you can get a high number of test subjects, implant sensors in various brain regions, and introduce drugs in order to measure their effects. It is not, however, simple to use animal models and many variables can arise that make these experiments challenging.

Slices from animal brain tissue are another common avenue for conducting neuroscience research.¹⁰ Brain slices can be kept alive in oxygenated buffer solution for several hours which allows time for experiments to be carried out. With brain slices it is possible to visibly place a sensor in a specific region of the brain in order to make measurements. This alleviates a lot of the complications that arise when working with a live animal and the brain circuitry can be less complicated to understand and manipulate. Brain slices do limit the conclusions that can be drawn from a study, however, because interconnected pathways have likely been disconnected during the slicing of the tissue. Single cells in culture, such as PC12 and chromaffin cells, are another environment that has been widely investigated because they offer an easier way of directly measuring phenomena such as exocytosis.¹¹⁻¹³

A flow injection apparatus is a valuable tool that is often used during the development of new electrochemical sensors and for calibration of sensors used *in vivo*.¹⁴ A flow injection apparatus is an *in vitro* system that allows for placement of an electrode within a continuous flow of buffered electrolyte. To replicate neuronal transmission, a high performance liquid chromatography valve is used to inject a short bolus of analyte into the flowing electrolyte. This allows for the analyte to quickly pass over the electrode before being swept away, thereby simulating chemical release events in the brain.

1.3 Analytical Methodologies for Measuring Neurotransmission

Having a clear picture of how the brain functions is of undeniable importance, but research has often been limited by inadequate methods for collecting data. As analytical

technologies developed during the 20th century, doors were opened that made new research avenues possible in the neuroscience field.

A number of methods have been created or adapted for conducting neuroscience research. As with any analytical methodology there are figures of merit that must be considered when assessing the usefulness of a technique for a particular research goal. A few of the key figures of merit to consider with techniques for neuroscience research include chemical selectivity, spatial resolution and temporal resolution.

A high degree of chemical selectivity is required in order to verify the signal you are measuring because the brain is a complicated environment with a myriad of analytes that could potentially be detected. The brain is also composed of many regions with vast functional diversity. Therefore a high degree of spatial resolution is vital for disentangling the role of individual brain regions. In addition, neuronal firing occurs on millisecond time scales, so a high temporal resolution is necessary for monitoring distinct events.

1.3.1 Electrophysiology

One of the oldest methods for measuring neuronal firing is electrophysiology.¹⁵ This technique is often used to monitor the potential across the cell membrane and thereby measure when action potentials occur. This is very useful for recording cellular activity with high temporal resolution and is capable of achieving excellent spatial resolution when coupled with microelectrodes. Analysis of the potential spikes is used to draw conclusions about the neuron that is recorded from but little to no information about the chemical environment can be attained using this technique.

1.3.2 Microdialysis

Microdialysis is a powerful technique for sampling a multitude of neurotransmitters.¹⁶ It is performed by inserting a probe into the brain region of interest and running a perfusion fluid within the membrane of the probe. As the perfusion fluid is pumped through, molecules are able to pass across the semi permeable membrane of the probe and be collected for analysis.¹⁷ Analysis is typically done offline by first separating the molecules with high performance liquid chromatography (HPLC) or capillary electrophoresis (CE).¹⁷ Many different detection methods have been used including UV-Vis, electrochemical, and mass spectrometry.

Excellent chemical selectivity is achieved with microdialysis because of the coupling with HPLC. It is simple enough to correlate peaks with their corresponding molecule on the chromatogram by running known standards. However, microdialysis has limitations associated with spatial and temporal resolution. A typical microdialysis probe is about 200-400 μm in diameter and 1-4 mm in length.¹⁸ This is much larger than individual release sites at synapses, and thus results in wide spatial averaging. The large probe size also damages a significant portion of the tissue surrounding the probe, thereby altering chemical diffusion to the membrane.¹⁹ The perfusion fluid is typically pumped at a rate of 1 $\mu\text{L}/\text{min}$, resulting in sampling intervals on the order of tens of minutes so that enough dialysate can be collected for analysis. While this is ideal for measuring slow changes, this technique is clearly not capable of measuring rapid chemical signaling events.

1.3.3 Spectroscopic Techniques

The main advantage of using a spectroscopic method is that it is possible to implement on human subjects. However, this approach is impractical for small mammals, such as the rat or mouse, unless the subject is anesthetized. Two principle techniques are positron emission tomography (PET) and functional magnetic resonance imaging (fMRI). PET requires the subject to intake a radiolabeled chemical that will emit positrons. The chosen chemical will interact with receptors for a specific neurotransmitter and scanners are able to measure and record this interaction.²⁰ fMRI measures variations in hydrogen spins that occur from changes in blood flow. Such changes indicate areas of brain activity. While it is possible to see a particular region that becomes activated, it is impossible to know what specific neurotransmitters are involved unless some type of pharmacological intervention is done. It is also difficult to incorporate this technique into behavioral studies.

1.3.4 Electrochemical Methods

The first electrochemical experiments done *in vivo* for the purpose of studying neurotransmitters occurred four decades ago by Ralph Adams.^{21, 22} Electrochemistry has proven quite amenable to the field of neuroscience because many neurotransmitters are electroactive. Electrochemical experiments are performed by applying a potential to an electrode and recording the current passing through the circuit. If a molecule is electroactive then it will either lose electrons (oxidize) or gain electrons (reduce) depending on the potential of the electrode. Different molecules will oxidize and reduce to different extents at specific potentials based on the formal potential ($E^{o'}$) of the molecule. The equation used to

describe the thermodynamics of this process is the Nernst Equation which relates the concentration (C) of the analytes to the potential of the electrode (E).

$$\text{Equation 1} \quad E = E^{o'} + \frac{RT}{nF} \ln \left(\frac{C_{\text{oxidized species}}}{C_{\text{reduced species}}} \right)$$

Some of the most commonly studied neurotransmitters such as dopamine, epinephrine, norepinephrine, and serotonin undergo this oxidative and reductive process easily. Additionally, the electrode can even be modified with enzymes so that molecules that are not electroactive, such as acetylcholine, can be detected by their enzymatic products.²³⁻²⁵ While there are many variations of electrochemical methods, for the purpose of this discussion we will limit our consideration to amperometry and voltammetry.

In amperometry the electrode is held at a constant potential in relation to a reference electrode. The holding potential is sufficient to oxidize or reduce the analyte under study. As soon as molecules come into contact with the electrode, current is passed and recorded. Calibration of electrodes with amperometry is not usually performed, but instead the total amount of species present is determined quantitatively by Faraday's law²⁶:

$$\text{Equation 2} \quad Q = nFm$$

where n is the number of electrons that are passed during the redox process. F is Faradays constant, m is the number of moles of the analyte, and Q is the total charge passed through the circuit. The greatest advantage of this technique is that the data collection rate is in the kHz range allowing for high fidelity measurements. For this reason, amperometry is most frequently employed for measuring exocytosis events occurring at single cells. Unfortunately, chemical selectivity is limited with this approach since all the species that

oxidize within the holding potential will be detected. As stated above, any molecules that are electroactive at the holding potential will produce current and will contribute to the total measured signal. This makes it impossible in a complex matrix to say with certainty what species was detected.

With voltammetry, the potential of the electrode is swept across a range of potentials. The potential limits are generally set to contain the oxidation and the reduction potentials of the analyte under study. The current generated at specific potentials from the oxidation and reduction of a molecule during the sweep is plotted against the applied potential, which results in a voltammogram. Molecules will generate voltammograms with different shapes and features that can serve to identify the specific analyte. For this reason, there is much greater chemical selectivity inherent to cyclic voltammetry than amperometry.

1.4 Fast-Scan Cyclic Voltammetry

Fast-scan cyclic voltammetry is a voltammetric technique where the potential is typically swept at a scan rate above 100 V/s. As a comparison, conventional cyclic voltammetry is often performed with scan rates on the order of millivolts per second. The fast scan rate presents both advantages and disadvantages for use of this technique. One advantage is that a single potential sweep is completed very quickly. Waveform limits that are commonly used are -0.4 V to 1.3 V and when implemented at 400 V/s one scan only takes 8.5 ms to complete. This is on a time scale commensurate with neuronal firing. The short duration of time per scan makes it possible to perform repeated scans in quick succession. Voltammograms are usually recorded at 10Hz, meaning that 10 separate

voltammograms are collected every second. This type of experiment allows for dynamic changes in chemical transmission to be monitored over time.

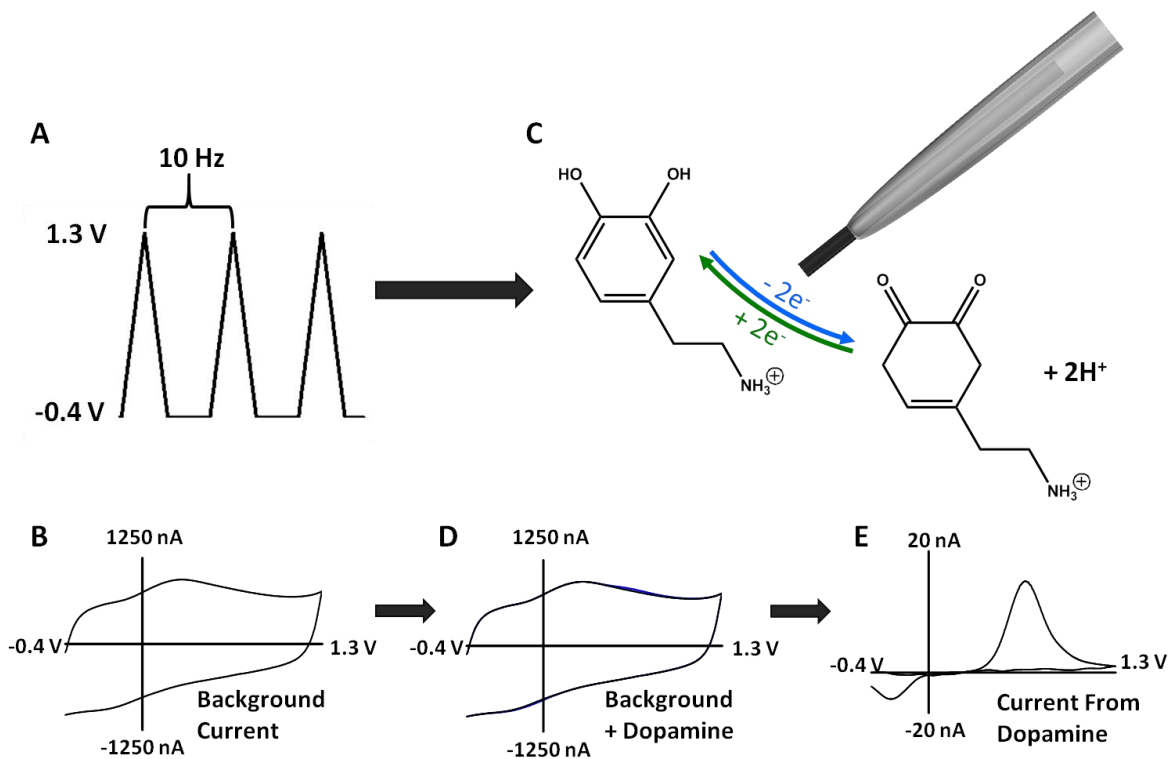


Figure 1.2 Diagram depicting process for background subtracted FSCV. A) A triangular waveform is continually applied at a high repetition rate to the electrode. B) The fast scan rates that are used generate a large background current. C) Analyte, such as dopamine, that pass across the electrode surface undergo traditional redox processes. D) Faradaic current generated from oxidation and reduction of dopamine is added to the background current. E) The background current is subtracted from the faradaic current generated from dopamine to give a characteristic voltammogram.

Another advantage of using this fast scan rate is that it increases the amount of faradaic current that is produced at the electrode when an analyte is oxidized or reduced.²⁶

The equation that describes the relationship between scan rate and analyte peak current is the Randles-Sevcik equation:

$$\text{Equation 3} \quad i_p = (2.69 \times 10^5) n^{\frac{3}{2}} A D^{\frac{1}{2}} C^* v^{\frac{1}{2}}$$

where i_p is the peak current, n is the number of electrons transferred, A is the area of the electrode, D is the diffusion coefficient of the analyte, C^* is the concentration of the analyte in the bulk solution, and v is scan rate. As shown here, the faster the scan rate that is implemented, the greater the current that will be generated, which is advantageous for improving the sensitivity of the technique.

The principle disadvantage of the fast scan rate is that it increases the amount of double-layer charging or background current collected at the electrode. This is illustrated in equation 4.

$$\text{Equation 4} \quad |i_c| = AC_d v$$

The charging current (i_c) is proportional to the area of the electrode (A), the double layer capacitance (C_d), and the scan rate (v). The background current produced at the electrode at these high scan rates is almost 100 times greater than the faradaic current from the analyte. As shown in Figure 1.2, any current generated from the analyte would be virtually impossible to distinguish when it is on top of such a large background current. This detection challenge is overcome through a background subtraction procedure where the background current collected prior to the analyte being detected can be used to subtract out the background current that coincides with the faradaic current from the analyte. This method is possible because the background current is generally stable over tens of seconds. Once the background current is subtracted out to see faradaic current from a particular molecule, any information regarding basal concentration levels is lost. This limits FSCV to only monitoring *changes* in chemical levels.

1.5 Data Analysis

It is common for FSCV experiments to last for 20 seconds or more. A new cyclic voltammogram is collected at a rate of 10 Hz and there are 1000 data points in every voltammogram. For a 20 second experiment this results in 200 voltammograms and 200,000 data points. To aid in data analysis, color plots are used to illustrate anodic and cathodic currents recorded during an experiment.²⁷

Figure 1.3 illustrates the method used to construct color plots for data analysis. First, the cyclic voltammograms are unfolded at the switching potential and concatenated in the order that they are collected. Once all of the data is together, colors are used to represent the current. Greens represent oxidative current and blues represent reductive current. Gold is used to show where there was a negligible change in current recorded. When the data is presented in this way it is easy to recognize at what time an analyte crossed the electrode and underwent electrolysis. From the color plots one can extract the original voltammograms or the current collected at a single potential over time.

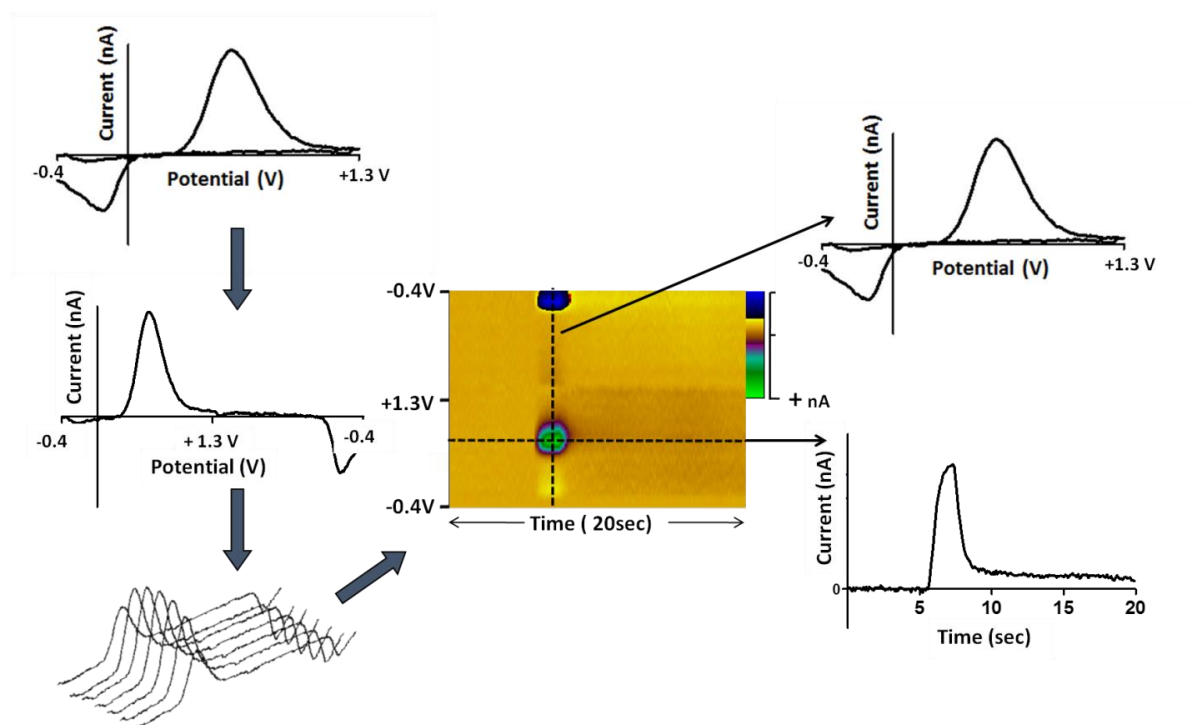


Figure 1.3 Diagram depicting process for constructing color plots used for analysis. Voltammograms are collected and unfolded at the switching potential and plotted in a linear fashion. The voltammograms are subsequently concatenated in the order they were collected in and false color is used to illustrate positive (green) and negative (blue) changes in current, thereby creating the color plot. From the color plot, the original voltammograms can be extracted by taking vertical slices at individual time points. Current verse time profiles at a single potential can also be extracted.

1.6 Carbon-Fiber Microelectrodes

For successful *in vivo* experiments the type of electrode used is just as important as the type of electrochemical technique that is used. FSCV inherently provides excellent temporal resolution and chemical selectivity. However, this says nothing about the spatial resolution needed to study discrete regions of the brain. Due to the unique benefits that they

offer, carbon-fiber microelectrodes (Figure 1.4) have proven to be the electrode of choice for coupling with FSCV.²⁸

Carbon fibers are approximately 10 μm in diameter and as an electrode they are often either cut to 100 μm in length or polished in a disk geometry. This small size provides a number of useful benefits. First, the decreased size reduces the voltage drop across the electrode that is common in larger electrodes. This makes the use of an auxiliary electrode unnecessary and allows for a two electrode system, which is easier to implement *in vivo*.²⁶ In addition the small size makes it possible to sample chemicals from discrete regions located within the brain. If the sensor spans multiple regions of the brain then it is impossible to relate data collected to a specific region. This small sensor provides the spatial resolution that is needed for sampling from the brain. Finally, the small sensor size reduces a lot of damage in tissue upon implantation that would occur with a larger electrode. It has been shown that microdialysis probes increase gliosis compared to carbon-fiber microelectrodes and alter the tissue over 1 mm away from where they were implanted.¹⁹ The small size of the carbon-fiber significantly decreases this damage.²⁹

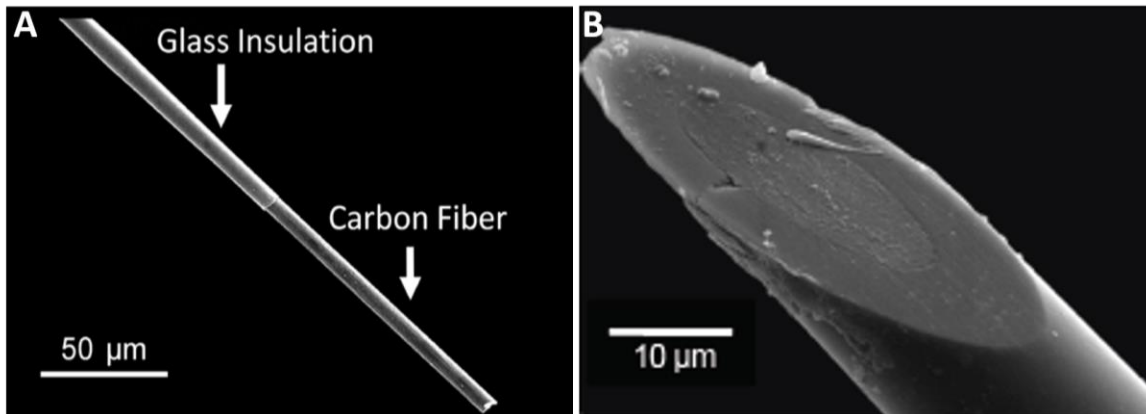


Figure 1.4 Images of commonly used carbon-fiber microelectrodes. A) Cylindrical electrode formed by heat sealing into a glass capillary and cutting the exposed carbon to 100 μm . B) Disk electrode formed by cutting the electrode shown in A at the glass seal, sealing in epoxy, and polishing on a diamond wheel.

Microelectrodes constructed from different metals have also been utilized with FSCV but carbon fiber boasts a number of advantages that make it preferable to metal electrodes.^{28, 30} Carbon fibers resist biofouling better than metals. This is important since experiments are done in the brain where many contaminants are present. Carbon-fibers also have a much wider potential window, are relatively inexpensive, and have a renewable surface.^{31, 32}

Carbon fibers are composed of graphitic sheets that are aligned along the length of the fiber. The graphitic sheets can be oriented in a number of directional patterns including onion, radial, and random orientation.³¹ The arrangement of the fiber can have a large impact on its usefulness. For instance, it is generally considered that the edge plane of the fiber is more electroactive than the basal plane.³³⁻³⁶ In addition to the microstructure of the carbon fiber, it is also known that the surfaces of carbon samples are covered in oxygen functional groups such as hydroxyl, carbonyl, and carboxyl groups.³⁷ The electrochemical performance

of the electrode is also thought to be impacted by the presence of these oxygen groups at the surface.³¹ For example, it has been shown that the detection of dopamine is greatly enhanced when the waveform applied to the electrode reaches +1.3 V and greater.³⁸ It is thought that the higher potential increases the oxygen population by oxidizing the surface, which increases available adsorption sites.

Many research groups have investigated graphitic surfaces seeking to better understand their properties, using techniques such as Raman spectroscopy, X-ray photoelectron spectroscopy (XPS), and various microscopies among other techniques.³⁹⁻⁴⁹ Raman spectroscopy with graphitic samples was first reported on in 1970 and has been widely used since as a means of determining microstructure characteristics.⁵⁰ The sp^2 hybridized carbon in graphitic samples as well as defects in the lattice are both easily identifiable in Raman spectra.^{51, 52} Changes in the microstructure have often been monitored by comparing the ratio of the graphitic and defect like structures in the carbon sample. Part of the work described in **Chapter 2** of this dissertation uses Raman spectroscopy to correlate the microstructural changes in the surface to electrochemical performance.

XPS is a common surface analysis technique that is capable of providing qualitative and semi-quantitative information on various elemental compositions.⁵³ Analysis of single carbon fibers with XPS is difficult however because the size of the spectral beam is often larger than the diameter of the carbon fiber. With XPS the spectral line from C_{1s} is often deconvoluted to determine the contributions from carbon-carbon bonds and carbon-oxygen bonds.⁵⁴ To help provide more quantitative information, carbon surfaces are often labelled with tags that bind to specific oxygen functional groups before analysis with Raman, XPS or

even electrochemical techniques.⁵⁵⁻⁵⁷ Since the tag can be easily measured with the technique it is applicable with, it provides an indirect means of quantifying specific oxygen groups. For instance, the molecule 2,4-dinitrophenylhydrazine is able to specifically bind with quinone like groups. Using this molecule, McCreery and co-workers determined that quinone like groups are found on approximately 1.2% of the carbon atoms at the surface of glassy carbon.⁵⁵

Many attempts have also been made at improving the electrochemical performance of carbon-fiber microelectrodes through various modification methods. One popular method of modifying the electrode is to add some type of coating to the surface.⁵⁸ For instance, Nafion is a cation exchange polymer that has been successfully added to carbon electrodes and implemented with *in vivo* experiments.^{30, 59-61} With Nafion, electrodes display an increased sensitivity toward catecholamines which are positively charged at physiological pH. The Nafion membrane also helps block interferents, such as the anion ascorbic acid, from reaching the electrode surface and confounding the signal.

Membrane coatings can also be used to enable the detection of non-electroactive molecules. Glucose has important biological functions in the brain but can not be detected with normal electrochemical methods because it is not electroactive. However, glucose oxidase can be attached to a carbon fiber by trapping it within a chitosin matrix.⁶² The glucose oxidase is able to enzymatically degrade glucose, creating hydrogen peroxide as a byproduct. Hydrogen peroxide is electroactive and provides an indirect measure for the presence of glucose.

Carbon nanotubes have also shown promise for improving the electrochemical performance of carbon-fiber electrodes. Venton and co-workers have shown that carbon nanotubes can be coated onto carbon-fiber microelectrodes and coupled with FSCV.⁶³⁻⁶⁵ They found that sensitivity toward dopamine was enhanced with electrodes that had the carbon nanotubes attached versus bare carbon fibers. In addition to modifications, it is also possible to replace the carbon fiber material entirely with other carbon materials. For example, microelectrodes have been made recently entirely out of carbon nanotube yarn material. The carbon nanotube yarn electrodes displayed faster apparent electron transfer properties and increased sensitivity to dopamine when compared to traditional carbon-fiber microelectrodes.⁶⁶

As highlighted above, carbon-fiber microelectrodes are a powerful tool for neuroscience related research and much effort has gone into studying and exploiting their characteristic properties. This theme is continued in this dissertation as much of the research presented was aimed at advancing FSCV by better understanding and improving the carbon-fiber electrode.

1.7 Dissertation Overview

The remainder of this dissertation is composed of five additional chapters and highlights research done that expounds on the topics covered in **Chapter 1**.

Chapter 2 describes extensive work done to characterize the surface of disk carbon-fiber microelectrodes. Raman spectroscopy was used to monitor changes in the carbon surface while potential waveforms were simultaneously applied. The surface

characterization was correlated with electrochemical data, providing useful information for developing modified waveforms.

Chapter 3 details the steps taken to create a unique cavity electrode through a plasma etching procedure. This work highlights the application of the cavity electrode for making chemical measurements at both brain slices and single cells and shows how a cavity can provide beneficial information that is lost with traditional disk electrodes.

The first display of intracellular measurements with chromaffin cells using FSCV is described in **Chapter 4**. This work details the fabrication steps taken in constructing a novel nanocone electrode that was capable of penetrating the cell wall in order to make electrochemical measurements. The entire electrode was insulated except for a reproducible length of exposed carbon at the tip, which ensured that sampling was done only in the intracellular space and that the extracellular environment was excluded. Norepinephrine and epinephrine content in vesicles were successfully distinguished intracellularly using FSCV.

One of the challenges that arises when collecting voltammetric data *in vivo* is interpreting the data when separate components are detected simultaneously. **Chapter 5** explains an approach taken to remove the current generated from pH, which overlaps and interferes with the detection of hydrogen peroxide. By using a double waveform, information was collected that made it possible to create a mathematical model that could subtract out the signal generated from a shift in pH. Finally, two appendix sections are included. Appendix A contains supplemental information to support the work in Chapter 3. Appendix B highlights voltammetric measurements of abiotic manganese oxides as part of a

collaborative effort to more fully understand the relationship between structure and reactivity for manganese oxide minerals.

1.8 References

1. (1998) Life and Discoveries of Santiago Ramón y Cajal, http://www.nobelprize.org/nobel_prizes/medicine/laureates/1906/cajal-article.html.
2. Grote, H., and Hannan, A. (2007) Regulators of adult neurogenesis in the healthy and diseased brain, *Clinical and Experimental Pharmacology and Physiology* 34, 533-545.
3. Tayebati, S. (2006) Animal models of cognitive dysfunction, *Mechanisms of Ageing and Development* 127, 100-108.
4. Kazantsev, A. (2007) Cellular pathways leading to neuronal dysfunction and degeneration, *Drug News & Perspectives* 20, 501-509.
5. Ghosh, J. (2006) Human development report 2005: International cooperation at a crossroads: Aid, trade and security in an unequal world., *Development and Change* 37, 1417-1423.
6. Pritchard, C., Mayers, A., and Baldwin, D. (2013) Changing patterns of neurological mortality in the 10 major developed countries - 1979-2010, *Public Health* 127, 357-368.
7. Kadakkuzha, B., and Puthanveetil, S. (2013) Genomics and proteomics in solving brain complexity, *Molecular Biosystems* 9, 1807-1821.
8. Mouton, P., Price, D., and Walker, L. (1997) Empirical assessment of synapse numbers in primate neocortex, *Journal of Neuroscience Methods* 75, 119-126.
9. Kandel, E. R., Schwartz, J. H., and Jessell, T. M. (2000) *Principles of neural science*, 4th ed., McGraw-Hill, Health Professions Division, New York.
10. John, C. E., and Jones, S. R. (2007) *Fast Scan Cyclic Voltammetry of Dopamine and Serotonin in Mouse Brain Slices*, CRC Press/Taylor & Francis, Boca Raton, FL.
11. Chen, G., and Ewing, A. G. (1997) Chemical analysis of single cells and exocytosis, *Critical reviews in neurobiology* 11, 59-90.
12. Schulte, A., and Schuhmann, W. (2007) Single-cell microelectrochemistry, *Angewandte Chemie* 46, 8760-8777.

13. Kim, D., Koseoglu, S., Manning, B. M., Meyer, A. F., and Haynes, C. L. (2011) Electroanalytical eavesdropping on single cell communication, *Anal Chem* 83, 7242-7249.
14. Roberts, J. G., Lugo-Morales, L. Z., Loziuk, P. L., and Sombers, L. A. (2013) Real-time chemical measurements of dopamine release in the brain, *Methods Mol Biol* 964, 275-294.
15. Hodgkin, A. L., and Huxley, A. F. (1939) Action potentials recorded from inside a nerve fibre, *Nature* 144, 710-711.
16. Perry, M., Li, Q., and Kennedy, R. (2009) Review of recent advances in analytical techniques for the determination of neurotransmitters, *Analytica Chimica Acta* 653, 1-22.
17. Watson, C., Venton, B., and Kennedy, R. (2006) In vivo measurements of neurotransmitters by microdialysis sampling, *Analytical Chemistry* 78, 1391-1399.
18. Schlitz, K., and Kennedy, R. (2008) Time-Resolved Microdialysis for In Vivo Neurochemical Measurements and Other Applications, *Annual Review of Analytical Chemistry* 1, 627-661.
19. Clapp-Lilly, K., Roberts, R., Duffy, L., Irons, K., Hu, Y., and Drew, K. (1999) An ultrastructural analysis of tissue surrounding a microdialysis probe, *Journal of Neuroscience Methods* 90, 129-142.
20. Benadiba, M., Luurtsema, G., Wichert-Ana, L., Buchpigel, C., and Busatto, G. (2012) New molecular targets for PET and SPECT imaging in neurodegenerative diseases, *Revista Brasileira De Psiquiatria* 34, S125-S148.
21. ADAMS, R. (1976) PROBING BRAIN CHEMISTRY WITH ELECTROANALYTICAL TECHNIQUES, *Analytical Chemistry* 48, 1126-&.
22. KISSINGEPT, HART, J., and ADAMS, R. (1973) VOLTAMMETRY IN BRAIN-TISSUE - NEW NEUROPHYSIOLOGICAL MEASUREMENT, *Brain Research* 55, 209-213.
23. Dale, N., Pearson, T., and Frenguelli, B. (2000) Direct measurement of adenosine release during hypoxia in the CA1 region of the rat hippocampal slice, *Journal of Physiology-London* 526, 143-155.

24. Llaudet, E., Botting, N., Crayston, J., and Dale, N. (2003) A three-enzyme microelectrode sensor for detecting purine release from central nervous system, *Biosensors & Bioelectronics* 18, 43-52.
25. Cevik, S., Timur, S., and Anik, U. (2012) Biocentri-voltammetric biosensor for acetylcholine and choline, *Microchimica Acta* 179, 299-305.
26. Bard, A. J. F., L. R. (2001) *Electrochemical methods : fundamentals and applications*, 2nd ed., John Wiley, New York.
27. Michael, D., Travis, E. R., and Wightman, R. M. (1998) Color images for fast-scan CV, *Analytical Chemistry* 70, 586a-592a.
28. Robinson, D., Hermans, A., Seipel, A., and Wightman, R. (2008) Monitoring rapid chemical communication in the brain, *Chemical Reviews* 108, 2554-2584.
29. Peters, J., Miner, L., Michael, A., and Sesack, S. (2004) Ultrastructure at carbon fiber microelectrode implantation sites after acute voltammetric measurements in the striatum of anesthetized rats, *Journal of Neuroscience Methods* 137, 9-23.
30. Roberts, J. G., Hamilton, K. L., and Sombers, L. A. (2011) Comparison of electrode materials for the detection of rapid hydrogen peroxide fluctuations using background-subtracted fast scan cyclic voltammetry, *Analyst* 136, 3550-3556.
31. McCreery, R. (2008) Advanced carbon electrode materials for molecular electrochemistry, *Chemical Reviews* 108, 2646-2687.
32. Takmakov, P., Zachek, M., Keithley, R., Walsh, P., Donley, C., McCarty, G., and Wightman, R. (2010) Carbon Microelectrodes with a Renewable Surface, *Analytical Chemistry* 82, 2020-2028.
33. Robinson, R., Sternitzke, K., Mcdermott, M., and McCreery, R. (1991) Morphology And Electrochemical Effects Of Defects On Highly Oriented Pyrolytic-Graphite, *Journal of the Electrochemical Society* 138, 2412-2418.
34. Bowling, R., Packard, R., and McCreery, R. (1989) Activation Of Highly Ordered Pyrolytic-Graphite For Heterogeneous Electron-Transfer - Relationship Between Electrochemical Performance And Carbon Microstructure, *Journal of the American Chemical Society* 111, 1217-1223.
35. McCreery, R. L. (1990) *Carbon Electrodes: Structural Effects on Electron Transfer Kinetics*, Vol. 17, Dekker, New York.

36. Banks, C., and Compton, R. (2005) Edge plane pyrolytic graphite electrodes in electroanalysis: An overview, *Analytical Sciences* 21, 1263-1268.
37. Boehm, H. P. (1994) Some Aspects of the Surface-Chemistry of Carbon-Blacks and Other Carbons, *Carbon* 32, 759-769.
38. Heien, M., Phillips, P., Stuber, G., Seipel, A., and Wightman, R. (2003) Overoxidation of carbon-fiber microelectrodes enhances dopamine adsorption and increases sensitivity, *Analyst* 128, 1413-1419.
39. Roberts, J., Moody, B., McCarty, G., and Sombers, L. (2010) Specific Oxygen-Containing Functional Groups on the Carbon Surface Underlie an Enhanced Sensitivity to Dopamine at Electrochemically Pretreated Carbon Fiber Microelectrodes, *Langmuir* 26, 9116-9122.
40. Hu, I. F., Karweik, D. H., and Kuwana, T. (1985) Activation and Deactivation of Glassy-Carbon Electrodes, *Journal of Electroanalytical Chemistry* 188, 59-72.
41. Pimenta, M. A., Dresselhaus, G., Dresselhaus, M. S., Cancado, L. G., Jorio, A., and Saito, R. (2007) Studying disorder in graphite-based systems by Raman spectroscopy, *Physical Chemistry Chemical Physics* 9, 1276-1291.
42. Wang, Y., Alsmeyer, D. C., and McCreery, R. L. (1990) Raman-Spectroscopy Of Carbon Materials - Structural Basis Of Observed Spectra, *Chemistry of Materials* 2, 557-563.
43. Kozłowski, C., and Sherwood, P. M. A. (1985) X-Ray Photoelectron-Spectroscopic Studies of Carbon-Fibre Surfaces .5. The Effect of Ph on Surface Oxidation, *J Chem Soc Farad T* 1 81, 2745-2756.
44. Pellenbarg, T., Dementev, N., Jean-Gilles, R., Bessel, C., Borguet, E., Dollahon, N., and Giuliano, R. (2010) Detecting and quantifying oxygen functional groups on graphite nanofibers by fluorescence labeling of surface species, *Carbon* 48, 4256-4267.
45. Wildgoose, G. G., Abiman, P., and Compton, R. G. (2009) Characterising chemical functionality on carbon surfaces, *J Mater Chem* 19, 4875-4886.
46. Pantano, P., and Kuhr, W. G. (1991) Characterization of the Chemical Architecture of Carbon-Fiber Microelectrodes .1. Carboxylates, *Analytical Chemistry* 63, 1413-1418.

47. Alsmeyer, D. C., and McCreery, R. L. (1992) In situ Raman Monitoring of Electrochemical Graphite-Intercalation and Lattice Damage in Mild Aqueous Acids, *Analytical Chemistry* 64, 1528-1533.
48. Proctor, A., and Sherwood, P. M. A. (1983) X-Ray Photoelectron Spectroscopic Studies of Carbon-Fiber Surfaces .2. The Effect of Electrochemical Treatment, *Carbon* 21, 53-59.
49. Kozłowski, C., and Sherwood, P. M. A. (1984) X-Ray Photoelectron Spectroscopic Studies of Carbon-Fiber Surfaces .4. The Effect of Electrochemical Treatment in Nitric-Acid, *J Chem Soc Farad T* 1 80, 2099-&.
50. Tuinstra, F., and Koenig, J. (1970) Raman Spectrum Of Graphite, *Journal of Chemical Physics* 53, 1126-&.
51. Mildred S. Dresselhaus, A. J., Mario Hofmann, Gene Dresselhaus, Riichiro Saito. (2010) Perspectives on Carbon Nanotubes and Graphene Raman Spectroscopy, *Nano Letters* 10, 751-758.
52. Matthews, M., Pimenta, M., Dresselhaus, G., Dresselhaus, M., and Endo, M. (1999) Origin of dispersive effects of the Raman D band in carbon materials, *Physical Review B* 59, R6585-R6588.
53. Turner, N. H., and Schreifels, J. A. (2000) Surface analysis: X-ray photoelectron spectroscopy and auger electron spectroscopy, *Analytical Chemistry* 72, 99r-110r.
54. Blyth, R. I. R., Buqa, H., Netzer, F. P., Ramsey, M. G., Besenhard, J. O., Golob, P., and Winter, M. (2000) XPS studies of graphite electrode materials for lithium ion batteries, *Appl Surf Sci* 167, 99-106.
55. Fryling, M. A., Zhao, J., and McCreery, R. L. (1995) Resonance Raman Observation of Surface Carbonyl Groups on Carbon Electrodes Following Dinitrophenylhydrazine Derivatization, *Analytical Chemistry* 67, 967-975.
56. Collier, W. G., and Tougas, T. P. (1987) Determination of Surface Hydroxyl-Groups on Glassy-Carbon with X-Ray Photoelectron-Spectroscopy Preceded by Chemical Derivatization, *Analytical Chemistry* 59, 396-399.
57. Thorogood, C. A., Wildgoose, G. G., Jones, J. H., and Compton, R. G. (2007) Identifying quinone-like species on the surface of graphitic carbon and multi-walled carbon nanotubes using reactions with 2,4-dinitrophenylhydrazine to provide a voltammetric fingerprint, *New J Chem* 31, 958-965.

58. Singh, Y. S., Sawarynski, L. E., Dabiri, P. D., Choi, W. R., and Andrews, A. M. (2011) Head-to-Head Comparisons of Carbon Fiber Microelectrode Coatings for Sensitive and Selective Neurotransmitter Detection by Voltammetry, *Analytical Chemistry* 83, 6658-6666.
59. Gerhardt, G. A., Oke, A. F., Nagy, G., Moghaddam, B., and Adams, R. N. (1984) Nafion-coated electrodes with high selectivity for CNS electrochemistry, *Brain Res* 290, 390-395.
60. Qi, L. J., Thomas, E., White, S. H., Smith, S. K., Lee, C. A., Wilson, L. R., and Sombers, L. A. (2016) Unmasking the Effects of L-DOPA on Rapid Dopamine Signaling with an Improved Approach for Nafion Coating Carbon-Fiber Microelectrodes, *Analytical Chemistry* 88, 8129-8136.
61. Brazell, M. P., Kasser, R. J., Renner, K. J., Feng, J., Moghaddam, B., and Adams, R. N. (1987) Electrocoating Carbon-Fiber Microelectrodes with Nafion Improves Selectivity for Electroactive Neurotransmitters, *Journal of Neuroscience Methods* 22, 167-172.
62. Lugo-Morales, L. Z., Loziuk, P. L., Corder, A. K., Toups, J. V., Roberts, J. G., McCaffrey, K. A., and Sombers, L. A. (2013) Enzyme-modified carbon-fiber microelectrode for the quantification of dynamic fluctuations of nonelectroactive analytes using fast-scan cyclic voltammetry, *Anal Chem* 85, 8780-8786.
63. Swamy, B. E. K., and Venton, B. J. (2007) Carbon nanotube-modified microelectrodes for simultaneous detection of dopamine and serotonin in vivo, *Analyst* 132, 876-884.
64. Xiao, N., and Venton, B. J. (2012) Rapid, Sensitive Detection of Neurotransmitters at Microelectrodes Modified with Self-assembled SWCNT Forests, *Analytical Chemistry* 84, 7816-7822.
65. Ross, A. E., and Venton, B. J. (2012) Nafion-CNT coated carbon-fiber microelectrodes for enhanced detection of adenosine, *Analyst* 137, 3045-3051.
66. Schmidt, A. C., Wang, X., Zhu, Y. T., and Sombers, L. A. (2013) Carbon Nanotube Yarn Electrodes for Enhanced Detection of Neurotransmitter Dynamics in Live Brain Tissue, *Acs Nano* 7, 7864-7873.

CHAPTER 2

Spectroelectrochemical Characterization of the Carbon Fiber Surface in Response to Electrochemical Conditioning

This work was completed in collaboration with: Dunaway, L.E., McCarty, G.S., and Sombers, L.A.

2.1 Introduction

Fast scan cyclic voltammetry (FSCV) continues to grow in popularity for neuroscience research because it offers considerable advantages over other electrochemical techniques. FSCV through the current voltage response enables analytes identification unlike competing electrochemical techniques, such as amperometry or chronoamperometry. The approach also provides excellent sensitivity^{1, 2} and data can be collected with millisecond temporal resolution due to the fast scan rates employed. For these reasons, FSCV is well suited for measuring neurochemical release events that happen on the millisecond time scale in the complex chemical environment of the brain.³⁻⁶ Despite these benefits, the technique is only valuable if it is coupled to an equally powerful sensing platform, such as carbon-fiber microelectrodes.

Carbon-fiber microelectrodes (CFMs) are fabricated from individual carbon fibers that are available in a range of sizes, most commonly from 5-30 μm . The carbon fiber is typically sealed in glass and polished or cut to length. The small size of these sensors provides the spatial resolution needed for measurements in discrete brain regions. They are

inexpensive and easily fabricated, offer a wide potential window, and resist biofouling.⁷⁻¹⁰ These properties have made CFMs the preferred sensor for bioanalytical studies over metal electrodes. They have even been shown to have a renewable surface when a sufficiently positive potential is applied.^{11, 12} These electrodes are effective at detecting a large variety of common neurotransmitters.^{3, 13-15} The carbon fiber surface has also proven amenable to various coatings such as Nafion, a well characterized cation exchange polymer, or chitosan with entrapped glucose oxidase to enable detection of non-electroactive glucose.¹⁶⁻¹⁸

Most carbon fibers are derived either from polyacrylonitrile or a mesophase pitch based source subjected to a series of heating processes that result in graphitization of the carbon.^{19, 20} The choice of precursor material and differences in the graphitization process give rise to structural variations that result in intrinsic differences in electrical conductivity, thermal conductivity, strength, and other properties across fiber types.^{19, 20} These properties can be improved by electrochemically pretreating the carbon surface.²¹⁻²⁴ For instance, repetitive excursions to potentials as high as +3.0 V enhances detection of dopamine (but can lead to unstable electrode performance)²⁵. Indeed, the literature contains many demonstrations of improved performance in the adsorption controlled detection of molecules such as dopamine after scanning a carbon electrode to a sufficiently positive potential (~1.3-1.5 V), as this treatment alters the carbon structure and increases the population of oxygen containing functional groups on the surface.^{11, 26-32} However, the chemical and physical effects of an applied potential on the carbon surface are generally not well understood. For instance, it is unclear what role, if any, negative potentials have on the carbon structure. To gain insight into how potential driven modifications to the carbon structure and surface

chemistry affect electrode performance, this work characterizes the surface using Raman spectroscopy during application of static and dynamic waveforms, and correlates measured changes with both electrochemical performance and physical changes evident in scanning electron micrographs. A range of positive potential limits (+1.0 - +1.4 V) are investigated, as are conditioning schemes that use a single potential, in order to generate insight to the effects of these treatments on the electrode surface. The results can be utilized to inform the development of new waveforms to overcome limitations when electrochemically targeting complex molecules, or those that are present in low concentrations.

2.2 Experimental Section

2.2.1 Chemicals

All chemicals were purchased from Sigma Aldrich Co. (St. Louis, MO) and were used without additional processing. Aqueous solutions were made using doubly deionized water (Barnstead Easy Pure II, Dubuque, IA). Unless otherwise noted, all electrochemical experiments were carried out in Tris buffered electrolyte (15 mM Tris, 3.25 mM KCl, 1.20 mM CaCl₂, 1.2 mM MgCl₂, 2 mM Na₂SO₄, 1.25 mM NaH₂PO₄, and 145 mM NaCl) with a pH of 7.4.

2.2.2 Electrode Fabrication

Elliptical carbon-fiber microdisk electrodes were constructed using pitch based p-55 fibers as previously described.¹⁰ Briefly, a single carbon fiber was aspirated into a glass capillary (1.0 mm x 0.5 mm, A-M Systems, Carlsburg, WA) and a micropipette puller was

used (Narishige, Tokyo, Japan) to form a tapered seal. The carbon fiber was then cut at the glass seal and dipped in epoxy and dried in an oven. The electrode was subsequently polished at 30° before use. An electrolyte solution (4 M potassium acetate, 150 mM KCl) was used to backfill the electrode and a lead was inserted to establish an electrical connection with the fiber.

2.2.3 Flow Injection

Electrochemical data were collected using a flow injection apparatus that was housed within a custom built Faraday cage to reduce interference from outside noise. The working electrode was positioned in the electrochemical cell using a micromanipulator (World Precision Instruments, Inc., Sarasota, FL). Buffered electrolyte was passed continuously over the working and reference electrode at 1 mL/min using a syringe pump (New Era Pump Systems, Inc., Wantagh, NY). A digital valve interface (Valco Instruments Co., Inc., Houston, TX) was used to control an air actuator connected to a six-port HPLC valve in order to make two second bolus injections of analyte across the working electrode. Electrode sensitivity was determined from calibrations of dopamine using three concentrations.

2.2.4 Electrochemical Data Acquisition

All potentials were reported versus a Ag/AgCl reference electrode. Analyte detection was accomplished using triangular waveforms applied at 400 V/s with an application frequency of 10 Hz, a lower potential limit of -0.4 V, and upper potential limits ranging from +1.0 to +1.4 V. Triangular waveform potentials were applied and current transduction was

accomplished using custom instrumentation (University of North Carolina at Chapel Hill, Department of Chemistry, Electronics Facility). Waveforms were output using a DAC/ADC card (NI 6251 M) with TH-1 software (ESA, Chelmsford, MA). Static potentials were applied to the electrodes using a waveform generator (Agilent 33220A). The flow injection system was coordinated with the electrochemical experiment using a second card (NI 6711). Background subtraction and signal averaging was software controlled. Electrode areas were compared by measuring the limiting current generated from the reduction of hexaamineruthenium(III) chloride with scan rates of 100 mV/s (WaveNano, Pine Instruments Company, Durham, NC). Analysis was done with Aftermath software (Version 1.4.7714, Pine Instruments Company). Solutions were prepared as previously shown and were deoxygenated with argon prior to use.³³ Electrodes were conditioned with dynamic waveforms in phosphate-buffered saline (0.1 M PBS) at pH 7.4 prior to limiting current analysis.

2.2.5 Surface Analysis

Raman spectra were collected for 30 seconds with a 60x objective using a custom spectrometer that has been described previously.³⁴ All spectra were collected while the carbon fiber was immersed in Tris buffer solution (pH 7.4). Images of the polished electrode surface were captured using a scanning electron microscope (Hitachi S-3200N) with a 5kV accelerating voltage. To enhance signal-to-noise, electrodes were sputtered with a 60/40 gold/palladium alloy prior to analysis.

2.2.6 Data Analysis

Data in figures is shown as the mean \pm standard error of the mean. Data in tables is presented as mean \pm standard deviation. Graphical and statistical analysis was performed with Graph Pad Prism 5 (GraphPad Software, Inc., La Jolla, CA). Electrode response time was calculated as the time it took to rise from 10% to 90% of the maximum peak current for an injection. All analysis of Raman spectra was done using Matlab (The Mathworks, Inc., Natick, MA). Background intensity was subtracted and spectra were lowered to the baseline using a spline fitting procedure. Intensity values used to calculate the I_D/I_G and $I_{D'}/I_G$ were taken from peak fitting parameters of the three peaks shown. The D peak ($\sim 1330\text{ cm}^{-1}$), G peak ($\sim 1580\text{ cm}^{-1}$), and D' peak ($\sim 1620\text{ cm}^{-1}$) were fit using a Lorentzian, Breit-Wigner-Fano, and Gaussian peak shape respectively.^{35, 36}

2.3 Results and Discussion

2.3.1 Microstructural Characterization with Raman Spectroscopy

Polished p-55 carbon-fiber microelectrodes were characterized with Raman spectroscopy using the experimental design shown in Figure 2.1. An electrochemical cell was positioned above the objective so that the electrode could be immersed in buffered electrolyte during Raman data collection. This in situ approach was advantageous in that it eliminated the need to transport the electrode through the air and possibly alter the surface chemistry. It also allowed for collection of spectral data during application of an electrochemical waveform to the electrode. Spectra collected in this manner best describe changes to the carbon fiber that occur during an electrochemical experiment.

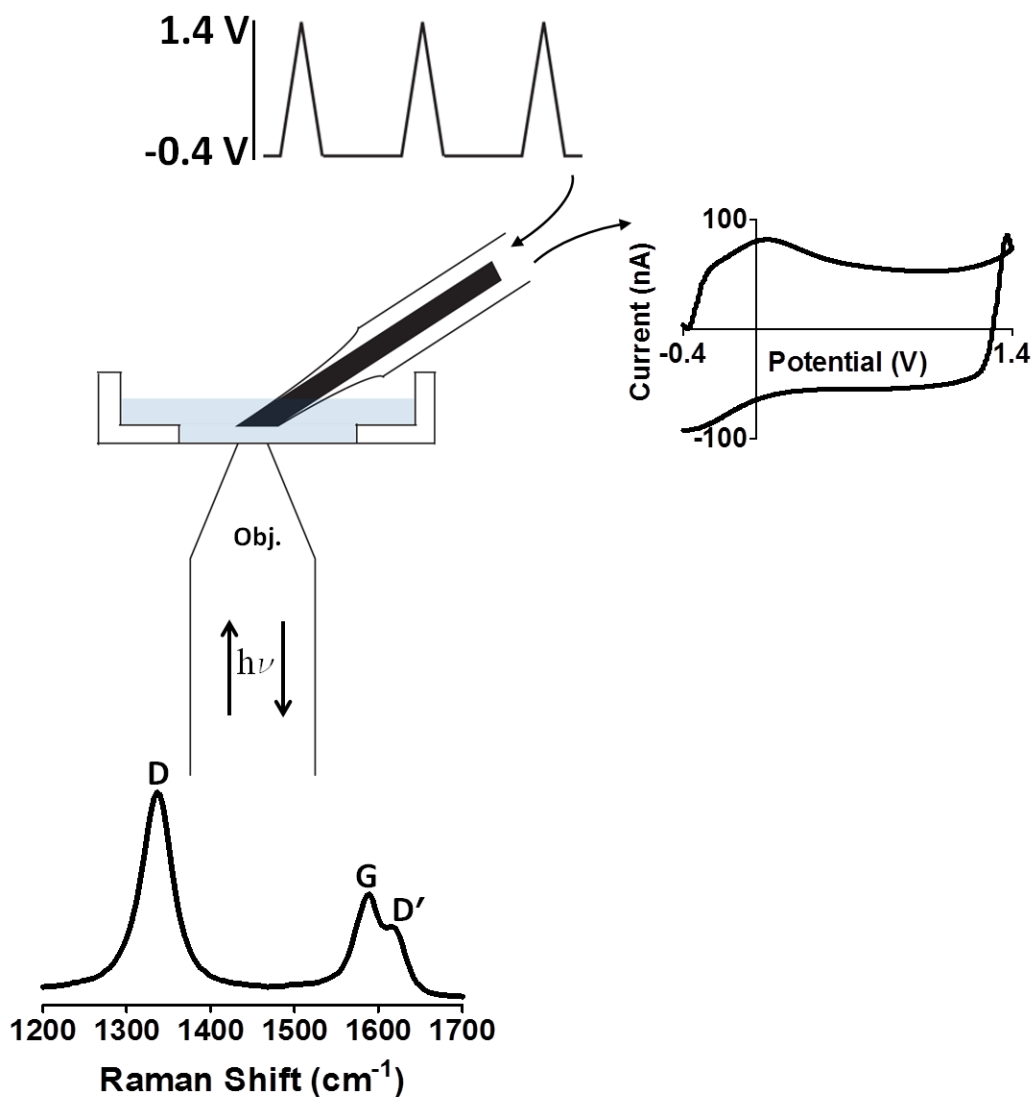


Figure 2.1 Experimental design. Raman spectra were collected for carbon fibers during electrochemical conditioning.

A representative spectrum from the analysis of a p-55 carbon fiber microelectrode is shown in the bottom of Figure 2.1. Three peaks are clearly identifiable. These comprise the characteristic Raman response for graphitic systems.³⁷⁻³⁹ A peak positioned at around 1580 cm^{-1} arises from sp^2 hybridized carbon stretches and is referred to as the ‘graphitic’ or G

peak. The peaks at approximately 1330 cm^{-1} and 1610 cm^{-1} have been related to a breaking of the symmetry in the graphitic lattice. For this reason they are referred to as ‘disorder related’ and are labeled D and D’, respectively. The ratio of D and G peaks (I_D/I_G) is commonly used as a measure of graphitic disorder in the system. In a graphitic sample that has long range crystalline order, the D and D’ peaks will be low or undetected. As the highly organized graphitic structure is disrupted, the disorder related peaks grow in intensity and I_D/I_G increases. This continues until a high level of amorphous carbon is present, at which point I_D/I_G decreases.⁴⁰⁻⁴² These trends make I_D/I_G a convenient and sensitive measurement to use for monitoring relative changes in the carbon structure. Therefore, the ratios of the disorder to graphitic peaks are used in this paper to compare structural changes that occur at the surface in response to the application of different potentials.

The p-55 carbon fiber surface was first analyzed in the absence of an applied potential to determine how the structural morphology varies at different positions on the fiber. Carbon fibers were analyzed at a spot on the side of the fiber, or at the tip (freshly cut with a scalpel blade). The spectra were normalized to the G peak to highlight differences in I_D/I_G (Figure 2.2). There is a significant increase ($p < 0.01$, $n = 4$, two-tailed t test) in I_D/I_G at the tip of the fiber (1.48 ± 0.11) versus the side (1.22 ± 0.07), which corresponds well with the skin-core morphologies that have been described elsewhere.⁴³ The surface of a freshly polished tip was likewise analyzed. The spectra show a significant increase in I_D/I_G (2.02 ± 0.11) over the tip and the side ($p < 0.01$, $n = 4$ tip and side, $n = 6$ polished, one-way ANOVA, Tukey post hoc).

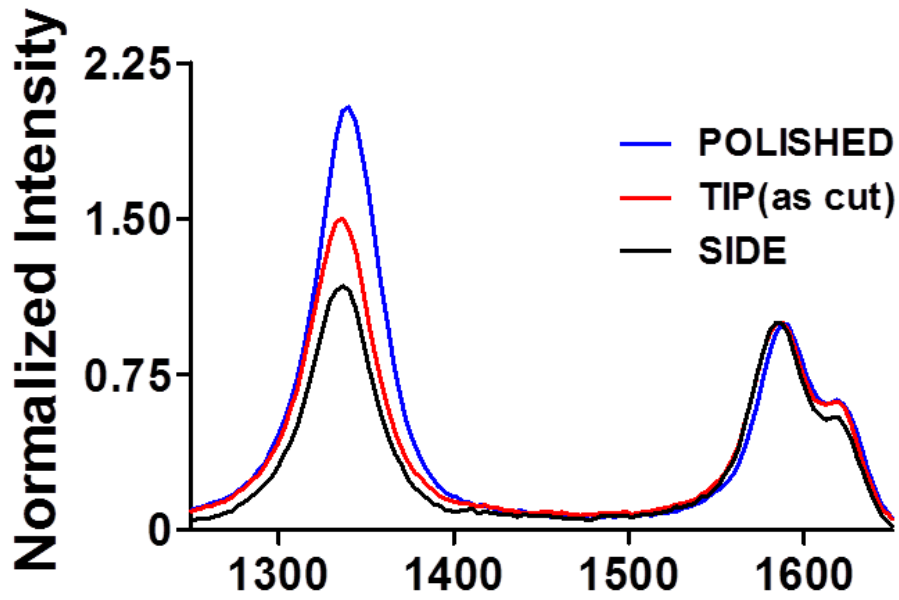


Figure 2.2 Polishing increases disorder on carbon surface. Representative spectra collected at the side, tip (as cut), and polished carbon fiber surfaces.

Previous studies have demonstrated a linear relationship between I_D/I_G and the crystallite dimension along the a-axis (L_a), such that as L_a decreases there is an increase in I_D/I_G .^{38-41, 44} The equation that relates I_D/I_G to L_a is written as:

$$L_a(\text{nm}) = (2.4 \times 10^{-10}) \lambda_{laser}^4 \left(\frac{I_D}{I_G} \right)^{-1}, \quad (1)$$

where λ_{laser} is the wavelength of the laser in nm.³⁸ Using this equation, L_a was estimated for the side, tip, and polished surfaces of the carbon fiber (Table 1). The polished surface has L_a dimensions that are approximately 7 and 12 nm shorter than the freshly cut tip and side respectively. These results indicate two important things: 1) Raman analysis is useful in distinguishing microstructural differences in our sample, and 2) polishing the electrode

surface induces crystallite defects (disorder) to the carbon structure, consistent with previous work.⁴⁵

Table 2.1 Microcrystallite Dimensions for the Different States of the P-55 Carbon Fiber

Surface Type	L_a (nm)
Side	31.5 ± 1.8
Tip (as cut)	26.0 ± 1.9
Polished	19.1 ± 1.1

2.3.2 Dynamic and Static Waveform Potentials Alter The Carbon Surface

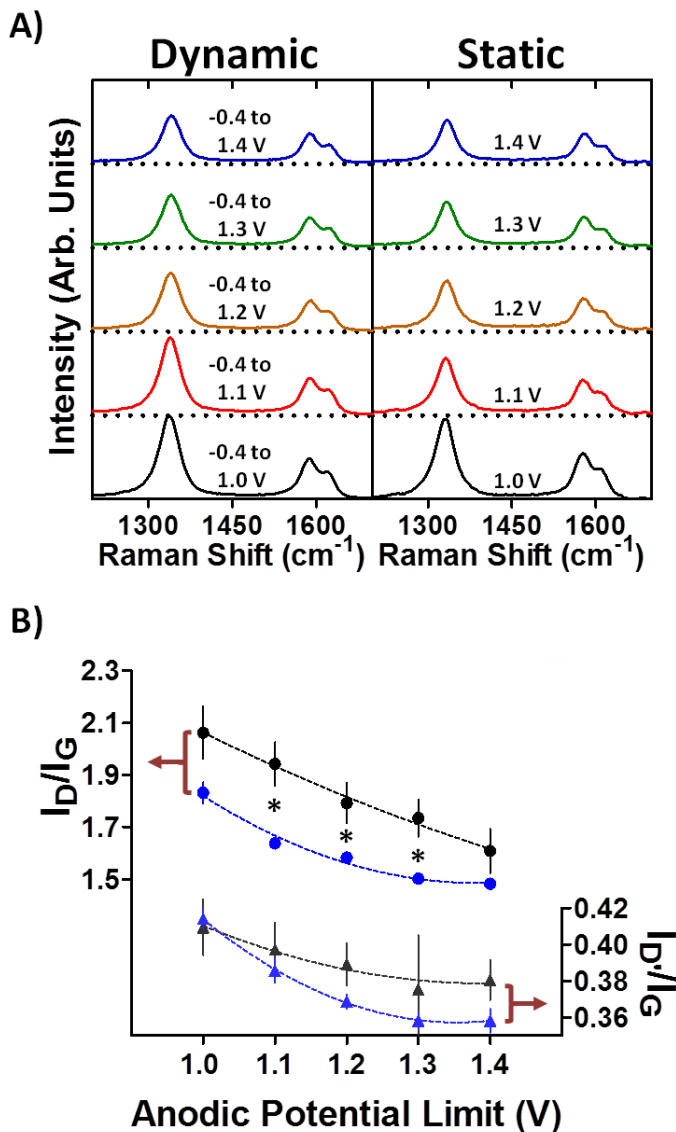


Figure 2.3 Dynamic and static conditioning paradigms elicit distinct changes to the carbon surface. A) Representative spectra of the carbon fiber surface during application of dynamic (left panel) and static (right panel) potentials. Spectra are offset for clarity. A decrease in the disorder related peak intensities can be seen. B) Plot of I_D/I_G (dots) and I_D/I_G (triangles) vs. dynamic (black) and static (blue) potential limits. There are significant differences between I_D/I_G resulting from dynamic and static conditioning (* $p < 0.05$, two-tailed t-test, $n = 4$ static, $n = 4$ dynamic)

To mimic preconditioning methods commonly used in voltammetric experiments, dynamic waveforms with holding potentials of -0.4 V and switching potentials ranging from +1.0 to +1.4 V were applied for 20 minutes at a frequency of 60 Hz to freshly polished electrodes immersed in Tris buffer. In order to isolate the effect of the positive switching potential, another set of electrodes was subjected to static waveforms ranging from +1.0 to +1.4 V for 10 minutes. Representative spectra are presented in Figure 2.3A. Each demonstrates the three bands characteristic of graphitic materials (vide supra); however, the intensity of the D and D' bands decreases as the magnitude of the applied potential (dynamic or static) is increased. Figure 2.3B plots the magnitude of I_D/I_G and $I_{D'}/I_G$ versus the highest potential applied to the electrode. Both ratios decrease as the potential is increased when either dynamic waveforms (data plotted vs. switching potential) or static potentials are applied to the electrode. Despite similar trends, there is a significant difference in I_D/I_G between static and dynamic waveforms for potentials of +1.1 to +1.3 V ($p < 0.05$, $n = 4$ dynamic, $n = 4$ static). This difference decreases as potentials increase, demonstrating a growing similarity in the surface characteristics of the carbon.

At first glance, the decreasing trend in I_D/I_G observed with an increased oxidation of the surface is surprising, but it is important to remember that the carbon surface starts the experiment in a highly disordered state from polishing (Figure 2.2). It has been shown that carbon fibers can etch away and lose mass when oxidizing potentials are applied for extended times, likely due to formation of carbon dioxide.^{11, 46} With this in mind, it seems probable that the outermost layer of carbon is being removed leaving behind layers of carbon that, while oxidized, are more ordered than the freshly polished surface. This idea is supported by

the electron micrographs shown in Figure 2.4. Immediately after polishing, the electrode surface does not exhibit distinguishing features indicative of short range ordering of the carbon (Figure 2.4A). After application of +1.4 V for 10 minutes, a more ordered carbon microstructure is evident (Figure 2.4B). When combined with the corresponding Raman spectra, these images suggest that polishing disturbs the graphitic layers, leaving carbon flakes packed tightly together in a highly disordered arrangement. In contrast, electrochemical oxidation alters the carbon, leading to distinguishing features at the surface.

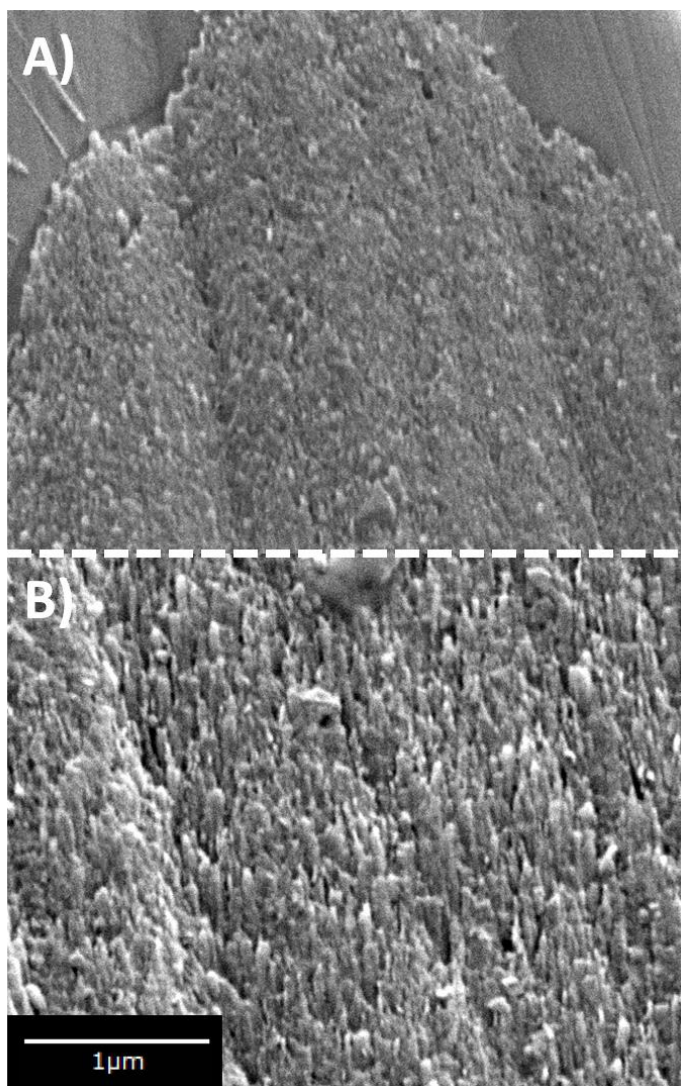


Figure 2.4 Surface changes can be visualized using SEM. Scanning electron micrographs of A) freshly polished carbon fiber surface and B) polished carbon surface after conditioning with a static +1.4 V for 10 minutes.

2.3.3 Dynamic and Static Pretreatments Differentially Affect Electrochemical Performance

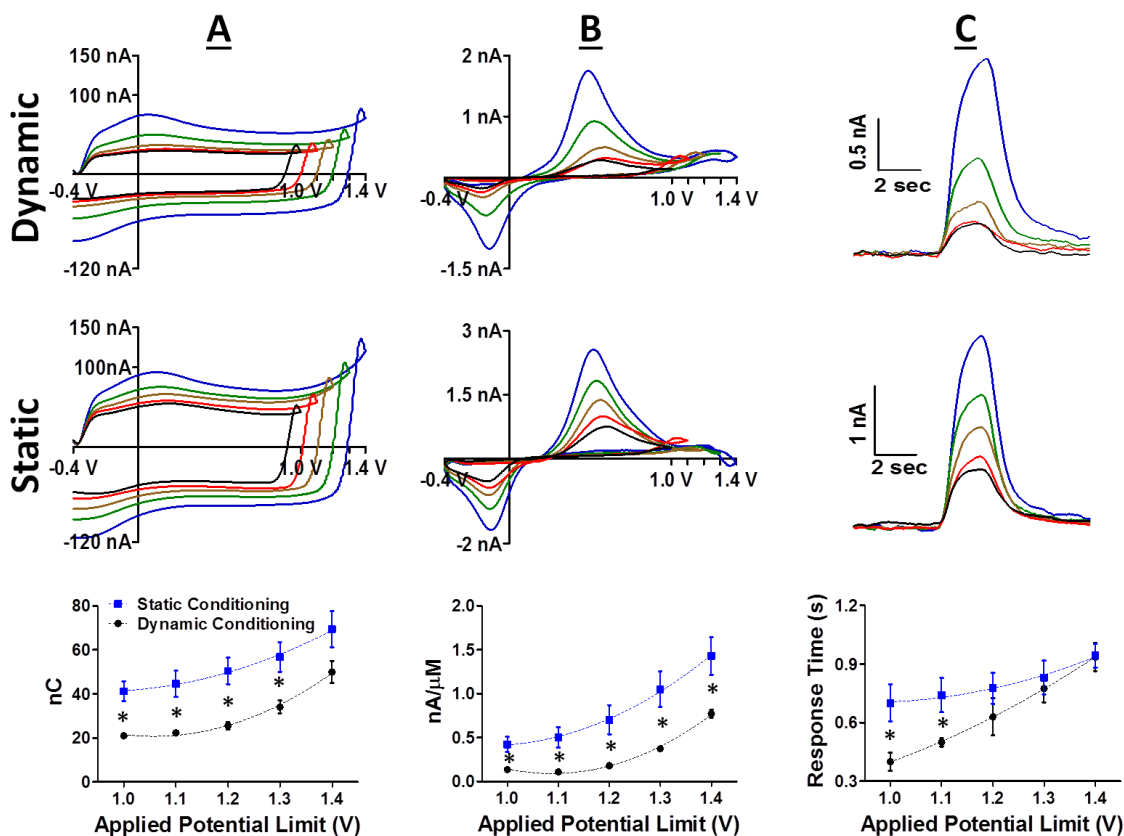


Figure 2.5 Conditioning affects electrochemical performance. Voltammetric data collected after dynamic (top) and static (middle) conditioning. Holding potential was -0.4V , and switching potentials varied from $+1.0\text{ V}$ to $+1.4\text{ V}$. A) Averaged background current (400 V/sec , 10 Hz). The charge (integrated current) for the quinone related peak on the background is plotted versus the applied potential limit in the bottom panel. B) Averaged background subtracted voltammograms for detection of $2\text{ }\mu\text{M}$ dopamine. The bottom panel plots sensitivity for these conditioning paradigms determined from the calibration of dopamine for three concentrations (1 , 1.5 , and $2\text{ }\mu\text{M}$). C) Averaged current vs. time traces. The bottom panel illustrates response time (10%-90% rise time). Static and dynamic conditioning paradigms significantly affect background charge, sensitivity to dopamine, and responsivity. (* $p < 0.05$, two-tailed t test, $n = 8$ (static), $n = 6$ (dynamic)).

Experiments were done to see how the structural changes described above correlate with electrochemical performance. Electrodes were conditioned with either a dynamic (60 Hz for 20 minutes) or static waveform (1 minute), and then a triangular waveform with a positive potential limit equal to the limit used for conditioning was used for data collection. The collection waveforms ranged from -0.4 to +1.0 up to +1.4 V with a scan rate of 400 V/sec. It has been shown previously that the magnitude of the background current is predictive of electrode sensitivity.⁴⁷ As expected, the background currents increased as the switching potential was raised for both dynamically and statically conditioned electrodes (Figure 2.5A). The background current is a combination of capacitive current and current generated from redox processes, most likely quinone like oxygen groups, at the carbon surface.⁴⁸ The area under the quinone related peak was integrated to estimate the population of oxygen on the surface of the electrode. The data suggest that the electrodes that were conditioned statically were significantly more oxidized ($p < 0.05$, one-tailed t test, $n = 6$ dynamic, $n = 8$ static) than those that were dynamically preconditioned, except for the +1.4 switching potential. Oxygen populations for dynamically preconditioned electrodes remained relatively low until potentials of +1.3 and +1.4 V were reached.

The electrochemical response to dopamine was also examined (Figure 2.5 B and C). As expected, the response to dopamine increased as the positive limit increased, matching the trend in the background current. Sensitivity to dopamine was significantly greater for electrodes that were statically versus dynamically conditioned ($p < 0.05$, one-tailed t test, $n = 6$ dynamic, $n = 8$ static). The response time of the electrode is a particularly important parameter when trying to monitor molecular dynamics in real time, and it has been shown

that response time slows as oxidation of the surface is increased.^{28, 49} Figure 2.5C plots response time against the positive potential limit. The response times are slowed as the positive limit is increased for both sets of conditioned electrodes. Interestingly, the response time for static preconditioning is slow even when the lower potentials of +1.0 and +1.1 V are used. This again highlights the structural modifications and oxidation that occur at the carbon surface, even at these lower potentials.

It is plausible that the increased sensitivity to dopamine that develops as the positive potential limit is increased might be the result of an increase in electrode surface area, due to surface roughening or a similar phenomenon. To test this hypothesis, voltammograms for hexaamineruthenium(III) chloride were collected on electrodes that were freshly polished, and then again on the same electrodes after dynamic conditioning for 20 minutes at 60 Hz. The equation for limiting current is:

$$i_{lim} = nF A m_o C \quad (2)$$

where n is the number of electrons transferred, F is Faradays constant, m_o is the mass transfer coefficient, C is the concentration of the redox species in the bulk solution, and A is the area of the electrode.⁵⁰ As shown in equation 2, the limiting current is directly related to the area of the electrode so increases in the surface area should be reflected in increases in the limiting current. However, no significant difference was evident between limiting currents collected at freshly polished vs dynamically conditioned electrodes ($p > 0.05$, paired t-test, $n=3$). While it is possible that very small changes in area would not be detected due to error associated with the measurement⁵¹, the data here suggest that the differences in electrochemical performance between these groups likely stem from small microstructural

and chemical changes at the surface of the carbon electrode, rather than from gross increases in electrode surface area.

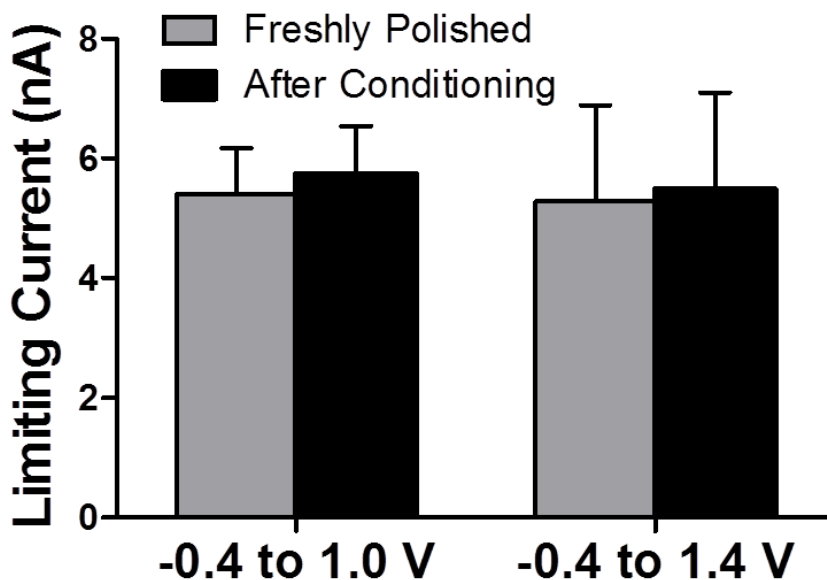


Figure 2.6 Electrochemical conditioning does not increase electrode surface area. Limiting current from reduction of hexamineruthenium(III) chloride was collected at electrodes after polishing (grey) and after conditioning the polished electrodes with +1.0 and +1.4 V dynamic waveforms (black). No significant difference was detected ($p > 0.05$, paired t-test, $n = 3$ for both conditioning methods).

Electrochemically conditioning carbon electrodes has previously been shown to increase the electron transfer rate for a variety of molecules, including DA and ascorbic acid.^{28, 45, 52-54} The data presented here (Figure 2.5, Table 2.2) show that the peak-to-peak separation for dopamine decreases as the positive switching potential is increased. This

indicates that the surface becomes better suited for dopamine oxidation and reduction as the positive potential limit is extended. The detection of ascorbic acid was also characterized on the same set of electrodes (Figure 2.7). When using dynamically preconditioned electrodes, the oxidation wave for ascorbic acid does not become well defined until limits of +1.4 V are applied. However, statically conditioned electrodes show a clear oxidation peak for ascorbic acid even when the positive potential limit only extended to +1.0 V. This interesting result indicates that lower potentials (+1.0 V) are sufficient to prepare the surface for oxidation of ascorbic acid when statically applied.

Table 2.2 Peak-to-Peak Separation for the Detection of 2 μ M Dopamine

Conditioning Method	1.0 V	1.1 V	1.2 V	1.3 V	1.4 V
Dynamic	0.77 ± 0.05	0.78 ± 0.04	0.73 ± 0.03	$0.67 \pm 0.04^*$	$0.60 \pm 0.02^*$
Static	0.74 ± 0.09	0.7 ± 0.1	0.68 ± 0.06	$0.64 \pm 0.05^*$	$0.62 \pm 0.05^*$

* $p < 0.05$, one-way Anova, $n=6$ (dynamic), $n=9$ (static), Tukey post hoc, values compared to +1.0 V

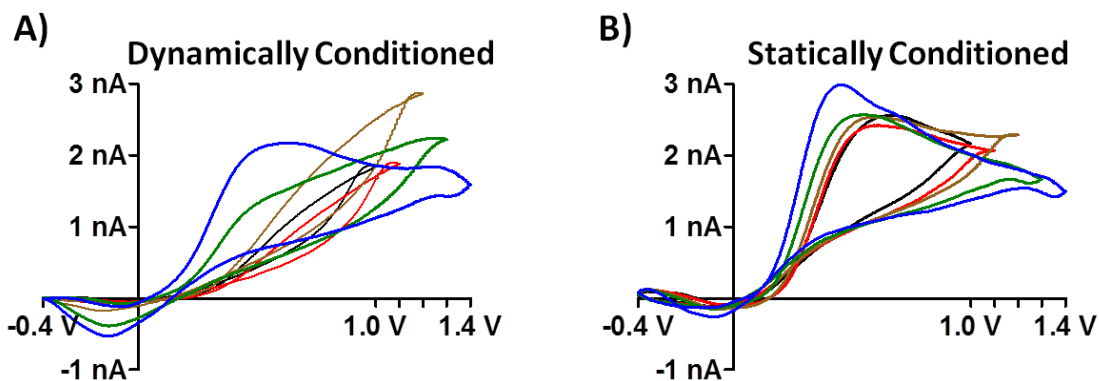


Figure 2.7 Conditioning alters electrochemical response for ascorbic acid. Averaged background subtracted voltammograms collected for 200 μM ascorbic acid using electrodes conditioned with A) dynamic and B) static potentials. Holding potential was -0.4 V and switching potentials vary from $+1.0\text{ V}$ (black), $+1.1\text{ V}$ (red), $+1.2\text{ V}$ (gold), $+1.3\text{ V}$ (green), to $+1.4\text{ V}$ (blue).

2.3.4 Rate of Change Comparison

In an effort to determine how quickly the preconditioning process changes the surface properties of the carbon, Raman spectra were collected at several time points during the course of preconditioning (Figure 2.8).

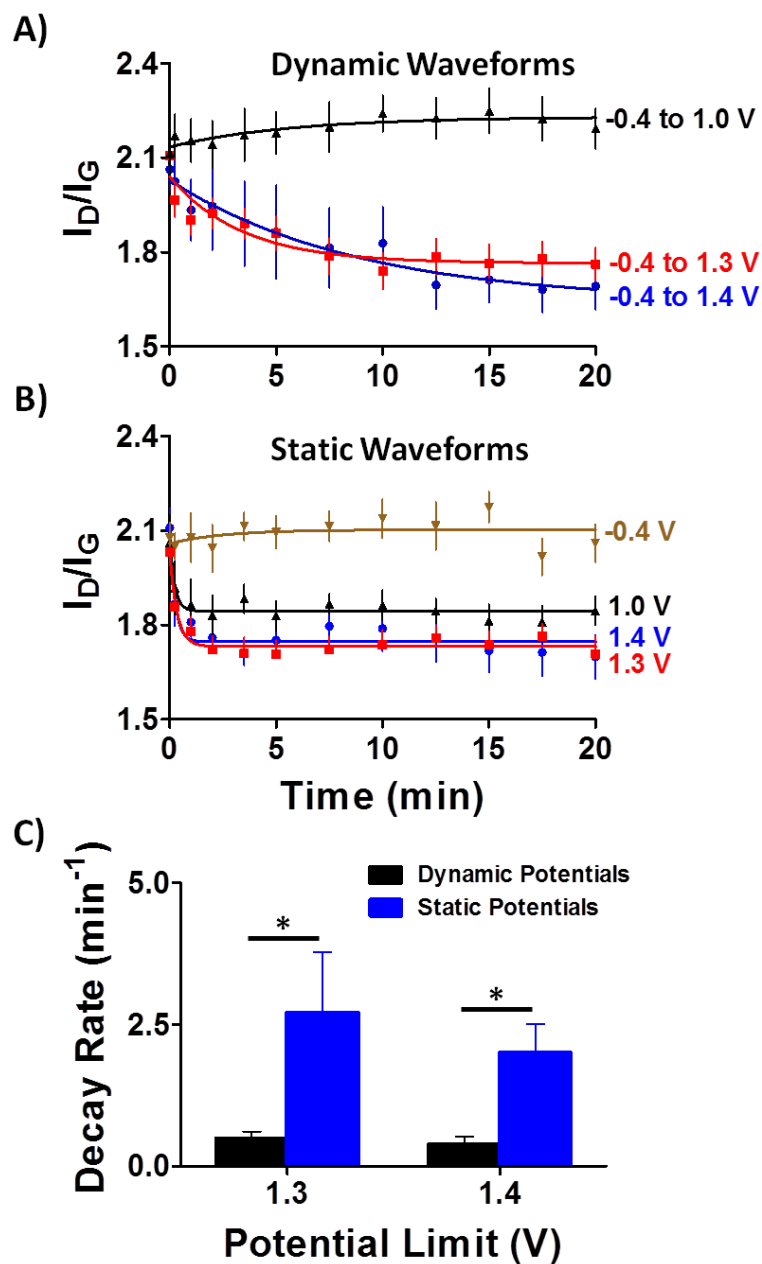


Figure 2.8 Static conditioning with positive potentials rapidly changes the carbon surface. Plots of I_D/I_G as a function of time for conditioning using A) dynamic waveforms and B) static waveforms. C) Rate constants determined from fit of the data in (A) and (B).

As expected, microstructural changes at dynamically conditioned electrodes (Figure 2.8A) occur more slowly than those at statically conditioned electrodes (Figure 2.8B). Indeed, the rate of decay, as determined from the fit of the data, demonstrates that static conditioning using +1.3 V (* $p < 0.05$, two-tailed t-test, $n=5$ static, $n=9$ dynamic) and +1.4 V (* $p < 0.05$, two-tailed t-test, $n=7$ static, $n=7$ dynamic) changes the surface significantly faster than dynamic conditioning with these potential limits (Figure 2.8C). It is worth noting that dynamic conditioning at +1.0 V and static conditioning at -0.4 V lead to no noticeable changes in the carbon microstructure whereas static conditioning with +1.0 V generates structural changes similar to those observed in response to higher applied potentials.

2.3.5 Surface Response to Alternating Static Potentials

The data presented herein clearly demonstrate that the structure of the carbon surface is changed by potentials ranging from -0.4V – +1.4V; potentials that are commonly used in voltammetry. When performing voltammetric experiments, alternating negative and positive potentials are applied over the course of an experiment. In order to investigate if the carbon surface dynamically responds to repetitive changes in the applied potential, +1.4 and -0.4 V were applied in an alternating pattern and spectra were collected over time (Figure 2.9).

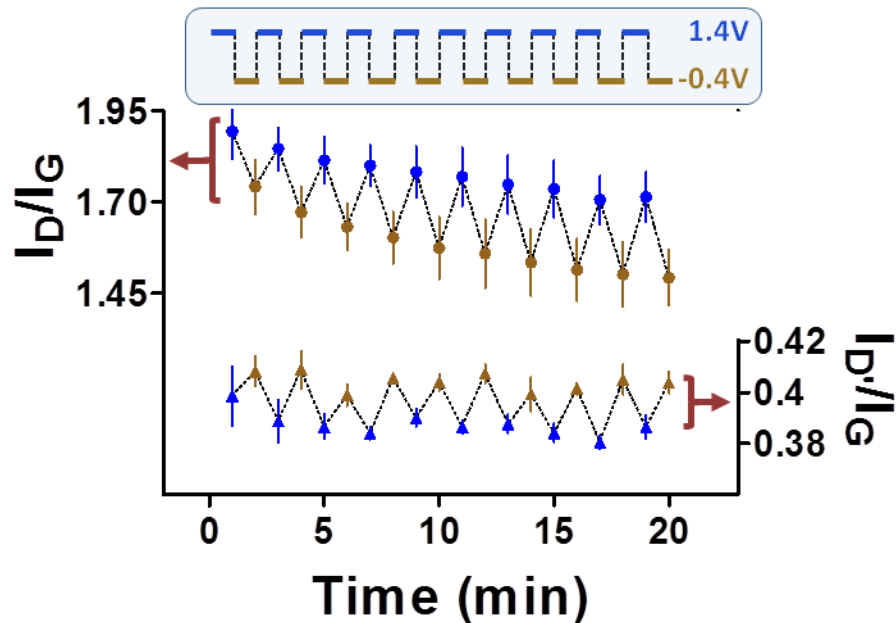


Figure 2.9 Carbon surface changes are dynamic. Plots of I_D/I_G (left y-axis) and $I_{D'}/I_G$ (right y-axis) as a function of time as static potentials of +1.4 and -0.4 V were alternately applied to the electrode (top).

Both I_D/I_G and $I_{D'}/I_G$ oscillate in response to the alternating potential. These data demonstrate that the carbon surface undergoes rapid structural reorganization as potential is applied, repeatedly alternating between a relatively ordered state, and one that exhibits greater disorder in the carbon lattice (increased I_D/I_G ratio). Importantly, these data highlight the dynamic nature of the graphitic layers in the carbon fiber. Rather than reaching a state of equilibrium, the carbon surface constantly responds to the positive and negative potentials applied in repetitive voltammetric sweeps.

2.4 Conclusions

The electrochemical performance of carbon fiber microelectrodes is highly dependent on the surface characteristics of the fiber. Using Raman spectroscopy we have shown that the carbon surface dynamically responds to applied potentials, and that positive potentials are more effective than negative potentials at eliciting a microstructural response (Figure 2.3, 2.9). In addition, static potentials are more effective than dynamic waveforms at eliciting microstructural changes to the carbon surface (Figure 2.3), changes which result in enhanced electrochemical performance (Figures 2.5, 2.7) even for lower statically applied potentials. For example, conditioning with a static potential of +1.0 V is sufficient to enable the voltammetric detection of ascorbic acid; however, conditioning with a dynamic waveform with a positive potential limit of 1.0 V is not. Likewise, conditioning with a static +1.0 V leads to a surface structure resembling that attained after conditioning with dynamic waveforms with a larger positive potential limit (Figures 2.3, 2.8).

Static waveforms are also more efficient than dynamic waveforms at eliciting structural changes (Figure 2.8), because the amount of time that the electrode is exposed to the more positive potentials likely underlies the observed differences in structure and electrochemical performance. Importantly, the carbon surface is a dynamic entity that continuously responds to the applied potential (Figure 2.9). These continual changes to the graphitic surface are likely a result of surface species, such as oxygen functional groups, repeatedly oxidizing and reducing due to the applied potential. Overall these data provide valuable insight into the surfaces of carbon-fiber microelectrodes in response to commonly applied potentials. We believe that the information presented herein will provide a guide to

electrochemical researchers working with carbon fiber microelectrodes as they determine what waveforms to use for their experiments.

2.5 References

1. Bucher, E. S., and Wightman, R. M. (2015) Electrochemical Analysis of Neurotransmitters, *Annual Review of Analytical Chemistry* 8, 239-261.
2. Kile, B. M., Walsh, P. L., McElligott, Z. A., Bucher, E. S., Guillot, T. S., Salahpour, A., Caron, M. G., and Wightman, R. M. (2012) Optimizing the Temporal Resolution of Fast-Scan Cyclic Voltammetry, *Acs Chemical Neuroscience* 3, 285-292.
3. Robinson, D., Hermans, A., Seipel, A., and Wightman, R. (2008) Monitoring rapid chemical communication in the brain, *Chemical Reviews* 108, 2554-2584.
4. Robinson, D. L., and Wightman, R. M. (2007) Rapid Dopamine Release in Freely Moving Rats, *Front Neuroeng* 1, 17-34.
5. Garris, P. A., and Wightman, R. M. (1995) *Regional Differences in Dopamine Release, Uptake, and Diffusion Measured by Fast-Scan Cyclic Voltammetry*, The Human Press Inc, Totowa, New Jersey.
6. Robinson, D. L., Venton, B. J., Heien, M. L. A. V., and Wightman, R. M. (2003) Detecting subsecond dopamine release with fast-scan cyclic voltammetry in vivo, *Clin Chem* 49, 1763-1773.
7. Armstrong-James, M., and Millar, J. (1979) Carbon fibre microelectrodes, *J Neurosci Methods* 1, 279-287.
8. Huffman, M. L., and Venton, B. J. (2009) Carbon-fiber microelectrodes for in vivo applications, *Analyst* 134, 18-24.
9. Wightman, R. (2006) Probing Cellular Chemistry in Biological Systems with Microelectrodes, *Science* 311, 1570-1574.
10. Kawagoe, K. T., Zimmerman, J. B., and Wightman, R. M. (1993) Principles of Voltammetry and Microelectrode Surface-States, *Journal of Neuroscience Methods* 48, 225-240.
11. Takmakov, P., Zachek, M., Keithley, R., Walsh, P., Donley, C., McCarty, G., and Wightman, R. (2010) Carbon Microelectrodes with a Renewable Surface, *Analytical Chemistry* 82, 2020-2028.
12. Keithley, R. B., Takmakov, P., Bucher, E. S., Belle, A. M., Owesson-White, C. A., Park, J., and Wightman, R. M. (2011) Higher Sensitivity Dopamine Measurements with Faster-Scan Cyclic Voltammetry, *Analytical Chemistry* 83, 3563-3571.

13. Schmidt, A. C., Dunaway, L. E., Roberts, J. G., McCarty, G. S., and Sombers, L. A. (2014) Multiple scan rate voltammetry for selective quantification of real-time enkephalin dynamics, *Anal Chem* 86, 7806-7812.
14. Jackson, B. P., Dietz, S. M., and Wightman, R. M. (1995) Fast-scan cyclic voltammetry of 5-hydroxytryptamine, *Anal Chem* 67, 1115-1120.
15. John, C. E., and Jones, S. R. (2007) *Fast Scan Cyclic Voltammetry of Dopamine and Serotonin in Mouse Brain Slices*, CRC Press/Taylor & Francis, Boca Raton, FL.
16. Roberts, J. G., Hamilton, K. L., and Sombers, L. A. (2011) Comparison of Electrode Materials for the Detection of Rapid Hydrogen Peroxide Fluctuations Using Background-Subtracted Fast Scan Cyclic Voltammetry, *Analyst* 136, 3550-3556.
17. Lugo-Morales, L. Z., Loziuk, P. L., Corder, A. K., Toups, J. V., Roberts, J. G., McCaffrey, K. A., and Sombers, L. A. (2013) Enzyme-Modified Carbon-Fiber Microelectrode for the Quantification of Dynamic Fluctuations of Nonelectroactive Analytes Using Fast-Scan Cyclic Voltammetry, *Analytical Chemistry* 85, 8780-8786.
18. Gerhardt, G. A., Oke, A. F., Nagy, G., Moghaddam, B., and Adams, R. N. (1984) Nafion-coated electrodes with high selectivity for CNS electrochemistry, *Brain Res* 290, 390-395.
19. Liu, Y. D., and Kumar, S. (2012) Recent Progress in Fabrication, Structure, and Properties of Carbon Fibers, *Polym Rev* 52, 234-258.
20. Huang, X. (2009) Fabrication and Properties of Carbon Fibers, *Materials* 2, 2369-2403.
21. Birkin, P. R., and SilvaMartinez, S. (1997) Determination of heterogeneous electron transfer kinetics in the presence of ultrasound at microelectrodes employing sampled voltammetry, *Analytical Chemistry* 69, 2055-2062.
22. Jaworski, R. K., and McCreery, R. L. (1994) Laser Activation of Carbon Microdisk Electrodes - Surface Oxide Effects on Ru(Nh3)6(2+/3+) Kinetics, *Journal of Electroanalytical Chemistry* 369, 175-181.
23. Hu, I. F., Karweik, D. H., and Kuwana, T. (1985) Activation and Deactivation of Glassy-Carbon Electrodes, *Journal of Electroanalytical Chemistry* 188, 59-72.
24. McCreery, R. (2008) Advanced carbon electrode materials for molecular electrochemistry, *Chemical Reviews* 108, 2646-2687.

25. Gonon, F. G., Fombarlet, C. M., Buda, M. J., and Pujol, J. F. (1981) Electrochemical Treatment of Pyrolytic Carbon-Fiber Electrodes, *Analytical Chemistry* 53, 1386-1389.
26. Roberts, J., Moody, B., McCarty, G., and Sombers, L. (2010) Specific Oxygen-Containing Functional Groups on the Carbon Surface Underlie an Enhanced Sensitivity to Dopamine at Electrochemically Pretreated Carbon Fiber Microelectrodes, *Langmuir* 26, 9116-9122.
27. Royce C. Engstrom, V. A. S. (1984) Characterization of Electrochemically Pretreated Glassy Carbon Electrodes, *Analytical Chemistry* 56, 136-141.
28. Heien, M., Phillips, P., Stuber, G., Seipel, A., and Wightman, R. (2003) Overoxidation of carbon-fiber microelectrodes enhances dopamine adsorption and increases sensitivity, *Analyst* 128, 1413-1419.
29. Swain, G. M., and Kuwana, T. (1991) Electrochemical Formation of High Surface-Area Carbon-Fibers, *Analytical Chemistry* 63, 517-519.
30. Swain, G. M., and Kuwana, T. (1992) Anodic Fracturing and Vacuum Heat-Treated Annealing of Pitch-Based Carbon-Fibers, *Analytical Chemistry* 64, 565-568.
31. Pihel, K., Walker, Q. D., and Wightman, R. M. (1996) Overoxidized polypyrrole-coated carbon fiber microelectrodes for dopamine measurements with fast-scan cyclic voltammetry, *Analytical Chemistry* 68, 2084-2089.
32. Hafizi, S., Kruk, Z. L., and Stamford, J. A. (1990) Fast Cyclic Voltammetry - Improved Sensitivity to Dopamine with Extended Oxidation Scan Limits, *Journal of Neuroscience Methods* 33, 41-49.
33. Baur, J. E., and Wightman, R. M. (1991) Diffusion-Coefficients Determined with Microelectrodes, *Journal of Electroanalytical Chemistry* 305, 73-81.
34. Zachek, M., Takmakov, P., Moody, B., Wightman, R., and McCarty, G. (2009) Simultaneous Decoupled Detection of Dopamine and Oxygen Using Pyrolyzed Carbon Microarrays and Fast-Scan Cyclic Voltammetry, *Analytical Chemistry* 81, 6258-6265.
35. Ferrari, A. C., and Robertson, J. (2000) Interpretation of Raman spectra of disordered and amorphous carbon, *Physical Review B* 61, 14095-14107.

36. Mcculloch, D. G., and Praver, S. (1995) The Effect of Annealing and Implantation Temperature on the Structure of C Ion-Beam-Irradiated Glassy-Carbon, *Journal of Applied Physics* 78, 3040-3047.
37. Chieu, T., Dresselhaus, M., and Endo, M. (1982) Raman Studies Of Benzene-Derived Graphite Fibers, *Physical Review B* 26, 5867-5877.
38. Pimenta, M. A., Dresselhaus, G., Dresselhaus, M. S., Cancado, L. G., Jorio, A., and Saito, R. (2007) Studying disorder in graphite-based systems by Raman spectroscopy, *Physical Chemistry Chemical Physics* 9, 1276-1291.
39. Tuinstra, F., and Koenig, J. (1970) Raman Spectrum Of Graphite, *Journal of Chemical Physics* 53, 1126-&.
40. Ferrari, A., and Robertson, J. (2000) Interpretation of Raman spectra of disordered and amorphous carbon, *Physical Review B* 61, 14095-14107.
41. Ferrari, A. C. (2007) Raman spectroscopy of graphene and graphite: Disorder, electron-phonon coupling, doping and nonadiabatic effects, *Solid State Communications* 143, 47-57.
42. Mildred S. Dresselhaus, A. J., Mario Hofmann, Gene Dresselhaus, Riichiro Saito. (2010) Perspectives on Carbon Nanotubes and Graphene Raman Spectroscopy, *Nano Letters* 10, 751-758.
43. Y. Huang, R. J. Y. (1995) Effect of Fibre Microstrucutre Upon the Modulus of Pan- and Pitch-Based Carbon Fibres, *Carbon* 33, 97-107.
44. Diane S. Knight, W. B. W. (1988) Characterization of Diamond Films By Raman Spectroscopy, *Journal of Materials Research* 4, 385-393.
45. Ronals Rice, C. A., Richard McCreery. (1989) Fast Heterogenous Electron Transfer Rates For Glassy Carbon Electrodes Without Polishing or Activation Procedures, *Jouranal of Electroanalytcial Chemistry* 263, 163-169.
46. Charles A. Goss, J. C. B., Eugene A. Irene, Royce W. Murray. (1993) Imaging the Incipient Electrochemical Oxidation of Highly Oriented Py, *Analytical Chemistry* 65, 1378-1389.
47. James G. Roberts, J. V. T., Eyob Eyualem, Gregory S. McCarty, and Leslie A. Sombers. In Situ Electrode Calibration Strategy for Voltammetric Measurements In Vivo, *Analytical Chemistry*.

48. Adam K. Dengler, R. M. W., Gregory S. McCarty. (2015) Microfabricated Collector-Generator Electrode Sensor For Measuring Absolute pH and Oxygen Concentrations, *Analytical Chemistry* 87, 10556-10564.
49. Jian-Xing Feng, M. B., Kenneth Renner, Richard Kasser, Ralph N. Adams. (1987) Electrochemical Pretreatment of Carbon Fibers for in Vivo Electrochemistry: Effects on Sensitivity and Response Time, *Analytical Chemistry* 59, 1863-1867.
50. Bard, A. J. F., L. R. (2001) *Electrochemical methods : fundamentals and applications*, 2nd ed., John Wiley, New York.
51. Watkins, J. J., Chen, J., White, H. S., Abruna, H. D., Maisonhaute, E., and Amatore, C. (2003) Zeptomole voltammetric detection and electron-transfer rate measurements using platinum electrodes of nanometer dimensions, *Anal Chem* 75, 3962-3971.
52. Engstrom, R. C. (1982) Electrochemical Pretreatment of Glassy Carbon Electrodes, *Analytical Chemistry* 54, 2310-2314.
53. Ladislav Falat, H.-Y. C. (1983) Electrocatalysis of Ascorbate and NADH at a Surface Modified Graphite-Epoxy Electrode, *Jouranal of Electroanalytical Chemistry* 157, 393-397.
54. Paul M. Kovack, M. R. D., R. Mark Wightman. (1986) Electrochemistry at Partially Blocked Carbon-Fiber Microcylinder Electrodes, *Journal of Physical Chemistry* 90, 4612-4617.

CHAPTER 3

Recessed Carbon-Fiber Microelectrodes for Use with Amperometry at Single Cells and FSCV in Brain Slice Preparations

This work was completed in collaboration with: Dunaway, L.E., Schmidt, A.C., Roberts, J.G., Shogren, T.J., Zach, M.P., and Sombers, L.A.

3.1 Introduction

Carbon-fiber microelectrodes (CFME) have been utilized to monitor exocytosis from single chromaffin cells in culture since 1990 by Wightman and colleagues^{1, 2}, discerning individual neurotransmitter release events and the conditions required for release. Further extensive research has been done by Ewing at PC12 cells³⁻⁵, examining neurotransmitter content^{6, 7}, spatial heterogeneity of exocytosis along the cell membrane^{8, 9}, dynamics of the fusion pore¹⁰⁻¹³, diffusion of neurotransmitters¹⁴, and catecholamine storage¹¹. Recently, Ewing *et. al* have developed a new method deemed intracellular vesicle electrochemical cytometry, performing amperometry with a conical nanotip microelectrode inside the cytoplasm of a cell.⁷ By comparing the contents of the vesicles inside of the cell to the measured content released by the vesicles upon exocytosis, they support the hypothesis that upon binding of the vesicle to the cell membrane, the fusion pore does not in fact open up entirely, resulting in incomplete release of the vesicular contents.

To monitor aspects of cellular neurotransmitter release via amperometry, the electrode placed on the cell surface is held at a potential sufficient to oxidize catecholamines being released from vesicles, typically in the range of +0.65 to +0.8 V. Owing to the excellent temporal resolution and sensitivity inherent to this technique, single-vesicle exocytosis can be resolved when the electrode is held immediately adjacent to the cell in an artificial synapse configuration. In addition to work at single cells, CFME's have been used for real-time detection of neurotransmitters in living brain tissue since the 1980's.^{15, 16} Background-subtracted fast-scan cyclic voltammetry (FSCV) provides the appropriate selectivity for the detection of neurotransmitter dynamics in the complex environment of the brain, while still retaining outstanding sensitivity and temporal resolution. Since its inception, FSCV has emerged as one of the leading techniques used for the detection of dopamine dynamics in the brain, and is used by several neuroscience research groups around the world. While initially implemented for the detection of dopamine, it has been further developed to allow for detection of various other monoamines, oxygen, hydrogen peroxide, adenosine, and even opioid peptides, in real time.

Traditionally, carbon-fiber microelectrodes are constructed with either cylindrical¹⁷⁻²⁰ or disk geometries.^{15, 21-24} Consideration of electrode geometry is critical in experimental design, as disk electrodes sample from a smaller area and provide better spatial resolution, while cylinder-shaped electrodes are capable of sampling the surrounding environment with greater sensitivity due to their increased surface area compared to the planer surface of a disk electrode. Experiments at single cells require an electrode capable of sampling from an area on the same order as the size of the cell, typically less than 20 μm in diameter²⁵. Thus, disk

electrodes are the preferred tool for these experiments, with a diameter of 5-10 μm . The decreased sensitivity of the disk, compared to a cylindrical electrode, is compensated for by using low-noise instruments to better resolve exocytotic events. Still, many events occur near the limit of detection, and the technique could benefit from a more sensitive electrode, particularly when investigations to elucidate fusion pore dynamics depend on the absolute detection of all neurotransmitters released from the vesicles.

A recessed carbon-fiber disk geometry (cavity) would be advantageous for this and a variety of applications, as a cavity helps to confine the analyte proximal to the sensing surface²⁶⁻²⁸ (Figure 3.1D). A recessed sensing surface is also shielded from convection, allowing detection of electroactive molecules with less contribution from outside forces.^{26, 29} In theory, this should allow for more efficient and sensitive detection of individual exocytosis events. Further, when used in conjunction with FSCV for detecting chemically reversible reactions, such as the oxidation of dopamine and subsequent reduction of its product dopamine-*ortho*-quinone, retaining the analyte near the sensing surface allows for detection of the same molecule multiple times, thus amplifying the signal (Figure 3.1 E,F)³⁰⁻³².

Recessed cavity microelectrodes have been constructed by others through combinations of complex fabrication techniques, often involving oxidative etching, various types of lithography, layer-by-layer deposition, and/or ion etching^{30, 33-35} While cavity electrodes offer numerous advantages over traditional disk electrodes, a simpler fabrication method is necessary in order for them to become more widely-employed in various research laboratories. In this work, single carbon-fiber microelectrodes are etched using a simple and straight-forward plasma-etching strategy developed in-house, generating a plasma by

applying a high potential across an air gap. This method reliably produces electrodes with a controllable cavity depth, which are characterized and compared to traditional disk electrodes herein using FSCV. Scanning electron microscopy, Raman spectroscopy, and traditional slow-scan voltammetry are utilized to study structural changes that occur during the etching process. The cavity electrodes are tested in an acute brain slice to evaluate their performance in complex tissue, and also compared to disk electrodes at single cells, detecting more molecules per release event than the widely used disk electrode. This suggests that current approaches to measuring exocytotic release at disk electrodes result in an overall underestimation of quantal size. There is still much to be learned about the dynamics and fundamental nature of exocytosis, and having a tool to more fully describe neurotransmitter release events will offer more reliable data to improve models and our overall understanding of quantal release.

3.2 Experimental Section

3.2.1 Chemicals

All chemicals were purchased from Sigma-Aldrich (St. Louis, MO) and used as received, unless otherwise specified. FSCV experiments were carried out in phosphate-buffered saline (0.1 M PBS) at physiological pH 7.4. Brain slice experiments were carried out in aCSF saturated with 95% O₂ and 5% CO₂, at physiological pH 7.4. aCSF consisted of 124 mM NaCl, 26 mM NaHCO₃, 3.7 mM KCl, 1.3 mM NaH₂PO₄, 2.4 mM CaCl₂, 1.3 mM MgCl₂, and 10 mM glucose. All aqueous solutions were made from doubly deionized water >18 MΩ·cm (Millipore, Billerica, MA).

3.2.2 Microelectrode Fabrication.

The microdisk electrodes were fabricated from T-650 carbon fibers as previously described.³⁶ Briefly, the disk electrodes were prepared by sealing standard carbon-fiber cylinder electrodes with epoxy (301 Epoxy; Epoxy Technology, Inc., Billerica, MA), curing overnight at 105°C, and polishing the electrode tip to the glass insulation at a 45° angle using a diamond dust-embedded micropipette beveling wheel (BV-10; Sutter Instrument Co., Novato, CA). Wet etching was performed in a flow injection apparatus, applying a waveform with a holding potential of +2.5 V and a negative ramp to +1.5 V, then returning to +2.5 V at 10 Hz. Plasma etching was performed in a custom-made apparatus (see Appendix A, Figure A.1). The carbon-fiber electrode (positive lead) and a conical stainless steel electrode (negative lead) were sealed in a glass chamber with a tip separation of ~1 cm. A picoammeter (Keithley Instruments, Inc., Cleveland, OH) was used to monitor the passage of current. The applied DC potential was sourced from a linear power supply (Lambda Electronics, Inc., Melville, NY) and regulated using a high voltage power supply (Bertan High Voltage Corp, Hicksville, NY). Custom written LabVIEW® software was used to control the applied potential.

3.2.3 Data Acquisition

All *in vitro* FSCV data were collected in a custom-built flow injection apparatus housed within a Faraday cage. A syringe pump (New Era Pump Systems, Inc., Wantagh, NY) supplied a continuous buffer flow of 1 mL/min across both the working and reference electrode. The working electrode was lowered into the electrochemical cell *via* a

micromanipulator (World Precision Instruments, Inc., Sarasota, FL). Bolus injections of analyte were accomplished using a six-port HPLC valve and air actuator controlled by a digital valve interface (Valco Instruments Co., Inc., Houston, TX).

3.2.4 Fast-Scan Cyclic Voltammetry

A triangular waveform was used for analyte detection. The applied potential ranged from -0.4 to +1.3 V, scanned at a rate of 400 V/s, and applied at a frequency of 10 Hz. The waveform was output using a custom-built instrument for potential application to the electrochemical cell and current transduction (University of North Carolina at Chapel Hill, Department of Chemistry, Electronics Facility). HDCV software (University of North Carolina at Chapel Hill, Department of Chemistry)³⁷ was used for waveform output with a DAC/ADC card (NI 6363). Signal processing (background subtraction and signal averaging) was software-controlled.

3.2.5 Raman Spectroscopy

Raman analysis was done using a custom spectrometer previously described.³⁸ To mimic the electrochemical environment, spectra were collected while the carbon-fiber electrodes were immersed in PBS solution. A 60x objective was used with collection times of 60 seconds. Prior to plasma etching, spectra were taken of carbon-fiber electrodes after polishing and electrochemical conditioning. The electrodes were subsequently etched and reconditioned and spectra were recollected at the same set of electrodes.

3.2.6 Brain Slice Preparation

Male Sprague-Dawley rats (250-300 g, Charles River Laboratories, Raleigh, NC) were decapitated after being deeply anesthetized with urethane (1.5 g/kg, i.p.). The brain was rapidly removed, mounted, and placed in cold aCSF. 400 μm thick coronal slices were cut with a vibratome (World Precision Instruments, Sarasota, FL). The slices were allowed to rest in aCSF for at least one hour, and were subsequently placed in a recording chamber (Warner Instruments, Hamden, CT) and superfused with buffered aCSF maintained at 34 °C for at least another hour. The working electrode and bipolar stimulating electrode placements were made with the aid of a microscope (Nikon Instruments, Inc., Melville, NY), and the microelectrodes were positioned about 50 μm below the surface of the slice. Electrical stimulation of nerve terminals consisted of five 500 μA biphasic pulses at 60 Hz using a pulse width of 4 msec. Animal care and use was in complete accordance with institutional guidelines and IACUC.

3.2.7 Primary Bovine Chromaffin Cell Culture

Six bovine adrenal glands were obtained to establish primary culture, and immediately trimmed of excess fat and submerged in ice-cold W3 buffer (145 mM NaCl, 5.4 mM KCl, 1 mM NaH_2PO_4 , 11.2 mM glucose, and 15 mM HEPES). Glands were perfused with cold W3 through the adrenal vein until the fluid coming out was clear and free of blood. The glands were trimmed of fat and perfused with warm W3, then incubated at 37 °C for 10 minutes and washed with W3, repeated three times. Next, glands were perfused with a digestion mixture containing 0.035 mg/mL DNAase and 1.4 mg/mL collagenase in W3 and

incubated for 15 minutes, again three times. After the first wash, nystatin (5mL/L) was added to W3 solution and this was used for the remainder of the steps involving W3. Glands were then dissected, removing and finely mincing the medullae. Minced medullae were placed in stirred digestion mixture for 30 minutes, filtered, and centrifuged at 1500 RPM to pellet the cells. Pellets were resuspended in W3 and mixed with a Percoll gradient. The Percoll gradient containing suspended cells was centrifuged at 10,000 RPM to separate red blood cells, chromaffin cells, and cellular debris. The chromaffin cell layer was collected and filtered through a 40 μ m sterile nylon filter. The filtrate was added to DMEM (Dulbecco's Modified Eagle Medium) and centrifuged at 800 RPM to pellet the cells. Supernatant was removed and pellets were resuspended in DMEM containing 10% FBS and 1% 100X Pen-strep. Using a hemocytometer, cells were diluted to a density of 3×10^5 cells/mL and plated on 35 mm culture dishes, with 2 mL in each dish.

3.2.8 Single Cell Experiments

Cells were prepared for the experiment by replacing the medium with an isotonic buffer containing calcium (150 mM NaCl, 5 mM KCl, 1.2 mM MgCl₂, 5 mM glucose, 10 mM HEPES, and 2 mM CaCl₂ at pH 7.4). The electrodes were lowered onto individual cells, maneuvering the electrode downward until the cell surface was slightly perturbed by the electrode. Exocytosis was stimulated with a 3 second, 20 psi pulse (Picospritzer II; General Valve Corporation, Fairfield, NJ) of high potassium isotonic stimulating buffer (55 mM NaCl, 100 mM KCl, 1.2 mM MgCl₂, 5 mM glucose, 10 mM HEPES, and 2 mM CaCl₂) using a micropipette polished to a 15 μ m opening. The culture dish containing the cells was

maintained at 37 °C during the experiment using a culture dish incubator (DH-35iL; Warner Instruments, LLC., Camden, CT).

3.2.9 Amperometry Data Acquisition and Analysis

Electrodes were held at +0.8 V vs. Ag/AgCl (World Precision Instruments, Inc., Sarasota, FL) using a patch-clamp amplifier (Axopatch 200B; Molecular Devices, LLC., Sunnyvale, CA). Amperometric output was filtered at 1 kHz using an internal four-pole low-pass Bessel filter and digitized at 2 kHz using an Axon Digidata 1440A (Molecular Devices). The amplifier was set to Whole Cell ($\beta = 1$) configuration in voltage-clamp mode. Data were collected and stored using Axoscope software (version 10.4.1.9; Molecular Devices). Peaks with intensity exceeding three times the standard deviation of the noise were identified as exocytotic spikes using Mini Analysis software (version 6.0.3, Synaptosoft). These spikes were evaluated for peak area (femtocoulombs), $t_{1/2}$ (milliseconds), and i_{\max} (picoamperes). All peaks identified by the program were visually inspected, and artifacts or other misidentified peaks were excluded from the analysis. Double peaks were separated into their constituent peaks. Peaks manually excluded or reevaluated (double peaks) accounted for approximately 5% of the total number of peaks identified by the program.

3.2.10 Slow-Scan Cyclic Voltammetry

Data were collected in 0.1 M NaPO₄, pH 7.0, using a WaveNano potentiostat (Pine Instruments Company, Durham, NC). The applied waveform ran from +200 mV to -800 mV and back, at a sweep rate of 100 mV/s. This scan rate proved to be low enough to maintain

steady state in all conditions. The cycle was performed twice on each electrode, with a rest period between segments of 1 second. Data were analyzed using Aftermath software (version 1.4.7714, Pine Instruments Company) to obtain the steady state current.

3.2.11 Data Analysis and Statistics

All data presented are shown as the mean \pm standard error of the mean (SEM). Unpaired *t* tests were used to determine the significance of means between two groups. Statistical and graphical analyses were carried out using GraphPad Prism 5 (GraphPad Software, Inc., La Jolla, CA).

3.3 Results and Discussion

3.3.1 Etching Carbon-Fiber Microelectrodes

Previous research¹⁹ has demonstrated that the surface of a carbon-fiber microelectrode (CFME) is etched in solution when potentials $\geq +1.3$ V vs. Ag/AgCl are applied, and the etching rate increases with application of higher potentials. Thus, it stands to reason that a carbon-fiber disk electrode could be etched to form a recessed disk (cavity) geometry by applying a sufficient potential. In the present work, cavity electrodes were initially fabricated from T-650 carbon-fiber disk electrodes by applying a waveform in PBS with a holding potential of +2.5 V, and scanning down to +1.5 V and back up to +2.5 V at 400 V/s, repeating at 10 Hz (see Appendix A, Figure A.2). Though some degree of success was achieved, this method was inconsistent in creating reproducible electrodes. When etching electrodes in solution, gases evolved from the electrode surface (observed through a

microscope, data not shown), leading to damage in the glass insulation. Furthermore, application of such high potentials in solution results in a high level of background noise inherent to the electrode, as shown in Figure A.2. Following the inability to make reliable electrodes in this fashion, a plasma-etching technique was developed that enables reproducible fabrication of cavity microelectrodes. The electrochemical performance of these electrodes is consistent across multiple electrodes, and superior to that of carbon-fiber microdisk electrodes.

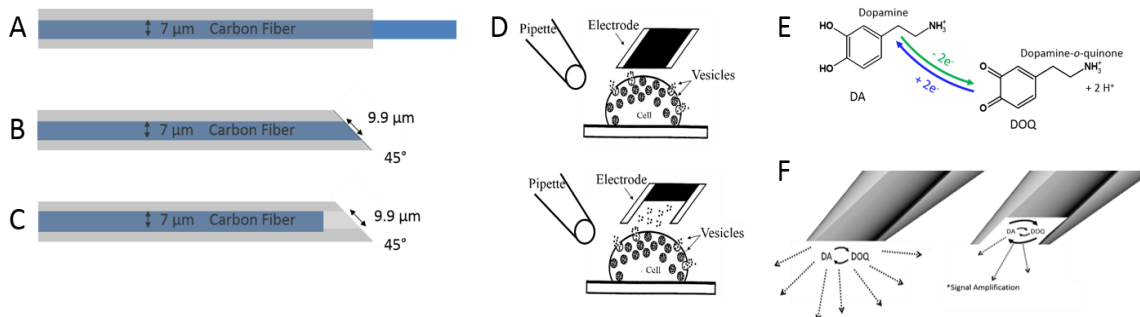


Figure 3.1 Fabrication of cavity electrodes. (A-C) Etching scheme. Cylinder electrodes are fabricated (A), sealed with epoxy, and polished to a 45° angle (B). By applying a high voltage across a 1 cm air gap, these electrodes are etched to ablate the carbon and create a cavity (C). (D) Schematic comparing cavity electrode and disk electrodes placed on a single cell, with the cavity allowing for restricted mass transport of molecules from the surface. (E) Electrochemical oxidation of dopamine to dopamine-*o*-quinone and subsequent reduction back to dopamine. (F) Restricting diffusion at the electrode surface allows for detection of the same redox pair multiple times when using FSCV (redox cycling), amplifying the signal.

Figure 3.1 A-C provides a simple step-by-step progression for reliable fabrication of cavity electrodes. Carbon-fiber microelectrodes are placed into the plasma etching chamber, such that a 1 cm gap is established between the carbon-fiber tip and a stainless steel electrode (Figure A.1). A potential is applied and increased in 25 V increments at a frequency of 4 Hz, while monitoring the passage of current between the electrodes. Once the target current is reached, it is retained for a predetermined length of time (5-30 seconds, depending on experimental needs), resulting in formation of a plasma between the electrodes that etches the carbon fiber, leaving the glass insulation intact and creating a cavity (1C).

3.3.2 Controlling Cavity Depth

Scanning electron micrographs are shown of a representative electrode with a 15 μm cavity (Figure 3.2A-D). Using a high-voltage beam reveals the position of the carbon underneath the glass insulation, while a low voltage beam images the surface of the glass insulation. The depth of the cavity is dependent on both the target current and the duration of etching time. Typically, the target current is reached at a potential of ~ 6 kV. While multiple target currents were evaluated, 15 μA yielded the most controllable and reproducible results. Even though the applied potential remains constant once the target is reached, the measured current fluctuates within a few μA of the target (Figure 3.2E). The amount of time the potential is applied proportionally affects the distance the carbon-fiber recessed. Integrating the measured current with respect to the etching time yields the total charge (mC) passed through the electrode. Figure 3.2F plots this charge versus the distance etched. The linear relationship ($r^2 = 0.83$, $n = 38$ electrodes) allows for precise control of cavity depth. Interestingly, other types of carbon-fibers have different etch rates. Pitch-based P-55 carbon-fibers etch at a slower rate than polyacrylonitrile (PAN) based T-650 carbon-fibers (data not shown).

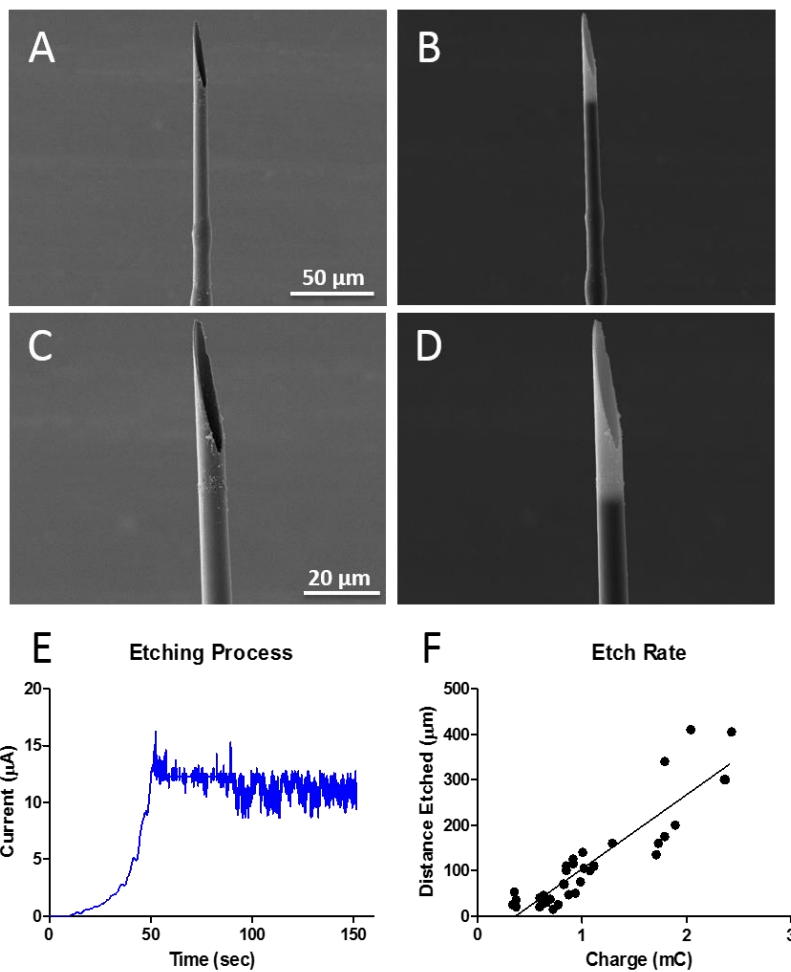


Figure 3.2 Cavity electrodes. (A-D) Variable pressure SEM images of a representative electrode etched to a 15 μm cavity depth. Panels A and C are collected with a 5.0 kV beam, and panels B and D with a 20.0 kV beam. (E) Representative current vs. time trace collected as the potential is increased and then held once the target current (15 μA) is reached. (F) The amount of charge passed through each electrode correlates linearly with the distance etched ($r^2 = 0.83$, $n = 38$)

3.3.3 Electrochemical Characterization

Broadly speaking, traditional carbon-fiber electrodes have been well characterized, especially for the detection of dopamine.^{17, 39, 40} Thus, the performance of the recessed

carbon-fiber electrodes was compared to carbon-fiber disk electrodes made of the same substrate, using FSCV. Compared to disk electrodes, the cavity electrodes generate greater charging current by approximately 15-fold (Figure 3.3A). However, the disk electrodes have a slightly larger geometric surface area due to their elliptical shape, when compared to the presumed circular shape of the sensing surface in the cavity CFME (Figure 3.1). In theory, charging current (i) is related to surface area by capacitance (C_d) of the electrode, which is proportional to surface area (Equation 2)⁴¹, through Equation 1⁴²:

$$i = \nu C_d (1 - e^{-\frac{t}{R_s C_d}}) \quad (1)$$

where R_s is solution resistance, and t is time.

$$C = \epsilon \frac{A}{d} \quad (2)$$

where C is capacitance, ϵ is permittivity, A is area of the plates of a capacitor, and d is distance between the plates.

While geometric surface area cannot account for the substantially increased charging current at the cavity electrode, there may be discrete changes at the surface that contribute to an increased capacitance that facilitates more efficient electron transfer at the etched sensing surface of the electrode. Sensitivities are compared using calibration plots for detection of dopamine, with concentrations ranging from 0.25 μM to 2 μM (Figure 3.3B). The sensitivity inherent to the cavity electrode ($5.23 \pm 0.22 \text{ nA}/\mu\text{M}$) is significantly higher than that inherent to the disk electrodes ($1.86 \pm 0.13 \text{ nA}/\mu\text{M}$, $p < 0.05$, $n = 11$). The ratio of the peak reductive and oxidative currents was also significantly greater ($p < 0.01$) for recessed carbon-fiber electrodes (0.65 ± 0.03 , $n = 11$) when compared to disk electrodes (0.39 ± 0.04 , $n = 3$), as

shown in Figure 3.3C. This is due to decreased mass transport at the sensing surface, as more dopamine-*o*-quinone would efficiently diffuse away at an electrode with disk geometry before being reduced back to dopamine. The effects of this diminished mass transport are also evident in the current vs. time trace extracted at the peak oxidation potential (Figure 3.3D). Current returns to baseline 10 to 12 seconds after oxidation using the disk electrodes, but remains above the baseline for a longer period of time (~20 seconds) with the recessed electrodes.

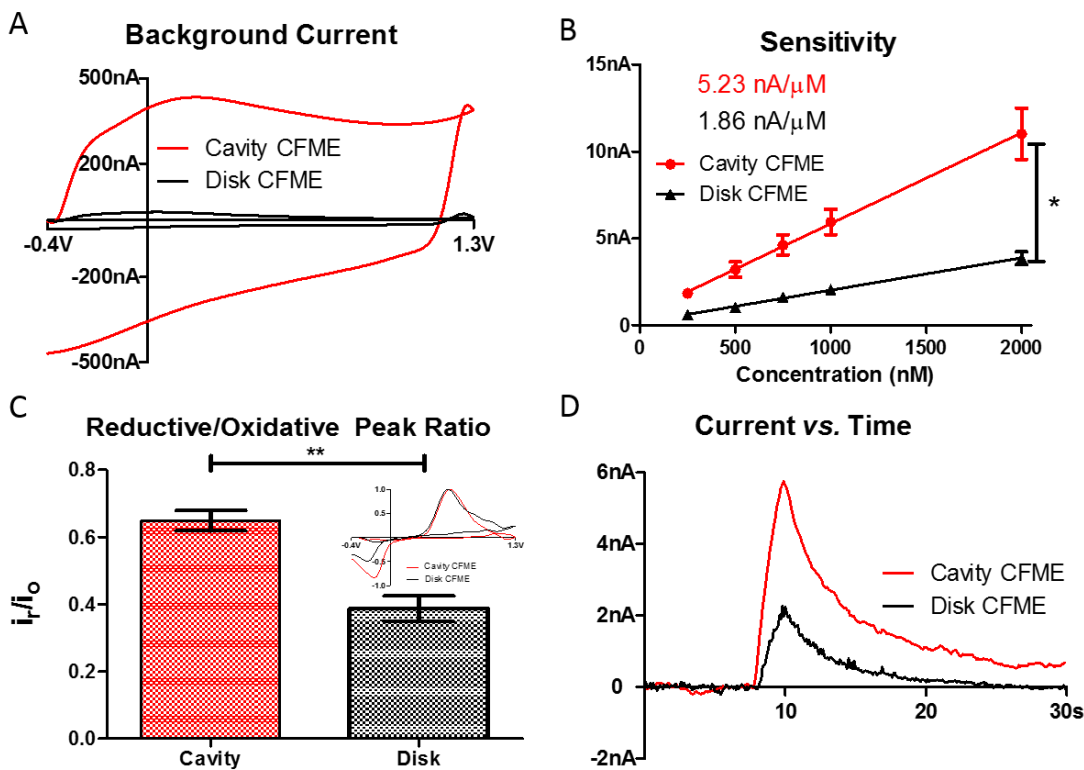


Figure 3.3 Electrochemical characterization of recessed carbon-fiber microelectrodes. (A) The background charging current is larger at cavity electrodes compared to disk electrodes. (B) Calibration plot shows that cavity electrodes are significantly more sensitive than disk electrodes (ANCOVA, $p < 0.05$, $n = 11$). (C) Bar graph showing reductive/oxidative peak ratio. Normalized representative voltammograms overlaid in the inset (Unpaired t-test, $p < 0.01$, $n = 11, 3$). (D) Current vs. time trace extracted at peak oxidation potential for 1 μM DA that shows decreased mass transfer within the cavity.

Multiple methods were used to study the surface characteristics of the etched and non-etched carbon. Field emission SEM provides a way to visually inspect the effects of plasma etching on the surface of the fiber. To prevent the glass insulation from shielding the carbon in the image, an uninsulated carbon fiber was etched and imaged with SEM. As seen in Figure 3.4A and 4B, this method of plasma etching appears to increase the roughness of

the fiber surface. This translates to an increase in the true surface area of the carbon in the cavity electrode, which could contribute to the increased sensitivity inherent to these electrodes.

Raman spectroscopy was employed to gain insight into the microstructure of the carbon fiber (Figure 3.4C, D). Spectra were collected at electrodes prior to and after plasma etching. Very broad peaks were observed in the spectra, which are indicative of a highly disordered surface.⁴³⁻⁴⁵ The two peaks observed are related to the sp² hybridized graphitic structure and to a breaking of symmetry along the graphitic lattice, and are referred to as the G and D peaks, at approximately 1560 and 1360 cm⁻¹, respectively. More detailed discussions related to the origins of these peaks have been presented elsewhere.⁴⁶⁻⁴⁸ The G and D peaks were fit using Lorentzian line shapes. In addition, as described by Ribeiro-Soares *et al*⁴³, two Gaussian line shapes peaks were fit at 1253 and 1520 cm⁻¹ to account for the broadening of the D and G peaks.⁴³ The I_D/I_G ratio was calculated by adding the widths of the D related bands and dividing by the sum of the widths of the G related bands. An estimate for the crystallite size was made using equation 9 in reference 46.

The data presented in Figure 3.4 suggest that the average crystallite dimension of the carbon is 8 ± 3 nm. In order to be consistent with the calibration experiments described in Figure 3.3, the fibers were cycled with the triangular waveform in PBS prior to imaging, both before and after etching. The electrodes were carefully positioned so that spectra were collected from the etched portion of the fiber. Interestingly, despite visible changes in the surface structure evident in SEM images, no significant differences were observed by Raman imaging before and after the etching procedure (p>0.05, two-tailed paired t-test, n=3). This

highlights that it is likely the cycling following the etching procedure, rather than the etching itself, that affects the microstructure of the carbon.

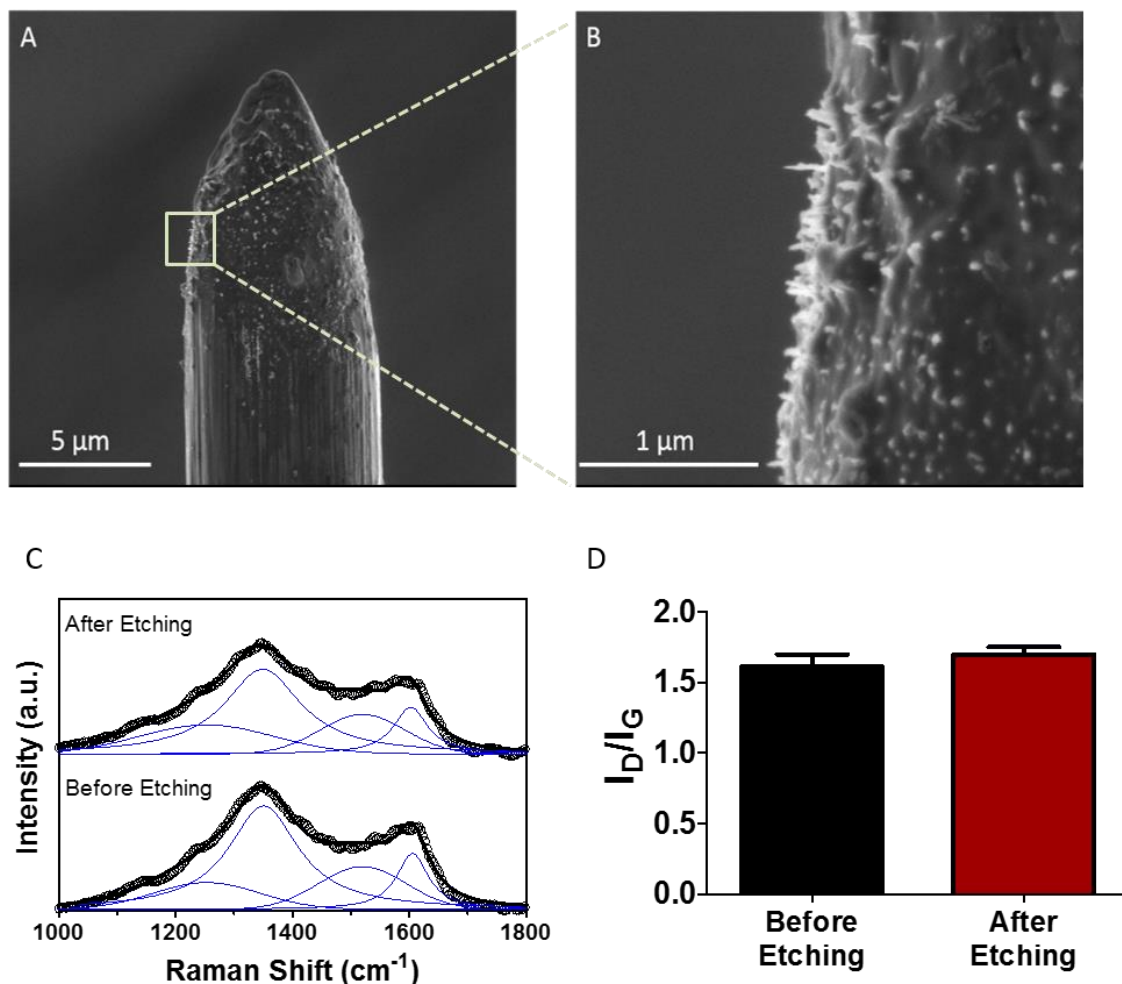


Figure 3.4 Field Emissions SEM and Raman imaging on plasma-etched electrodes. (A) Plasma-etched electrode with tip exposed for imaging. The roughened tip where the etching is taking place visually contrasts with the smooth side of the fiber. (B) 100,000x magnification of the etched tip. (C) Representative spectra (black) and fitted peaks (blue) of a polished and electrochemically conditioned carbon fiber electrode before and after the plasma etching procedure. (D) The ratio of peak amplitudes (I_D/I_G) is unchanged by the etching process ($p > 0.05$, two-tailed paired t-test, $n = 3$).

Another possible cause for the increased sensitivity of the cavity electrodes is an increase in surface area at the microscopic level. Peak current in cyclic voltammetry is described by the Randles-Sevcik equation (Equation 3), whereby peak current is proportional to sensing area of the electrode.

$$i_p = 0.4463nFAC \left(\frac{nFvD}{RT} \right)^{1/2} \quad (3)$$

where i_p is peak current, n is number of electrons transferred, F is the Faraday constant, A is sensing area of the electrode, C is concentration, v is scan rate, D is diffusion coefficient, R is the gas constant, and T is temperature.

Assuming a circular geometry, a 7 μm carbon fiber should generate a geometric surface area of 38.5 μm^2 , while a polished (45°) created from the same fiber should have an elliptical surface area of 54.4 μm^2 . Slow-scan cyclic voltammetry (100 mV/s) was utilized to estimate the area of the active sensing surface of cavity and standard micro-disk electrodes. Steady-state cyclic voltammograms were collected for 1 mM $\text{Ru}(\text{NH}_3)_6^{3+}$. Through the steady state current, the surface area of the electrode was found using the equation for steady state current at a microdisk electrode⁴²:

$$i = 4nFDCr \quad (4)$$

where i is the measured current, n is the number of electrons transferred, F is the Faraday constant, D is the diffusion coefficient, C is the concentration of the analyte species, and r is the radius of the electrode. The diffusion coefficient for $\text{Ru}(\text{NH}_3)_6\text{Cl}_3$ used in calculations is $5.48 \times 10^{-6} \text{ cm}^2/\text{s}$.⁴⁹ Once the radius of the electrode was found using equation 4, the surface area was calculated as the area of a circle.

Surface areas for disk electrodes, as well as cavity electrodes with a recessed length of 5, 15 and 20 μm were calculated and are shown in Figure 3.5. The experimentally determined surface area is likely greater than the geometric surface area due to the increased surface roughness. Notably, there is no significant difference in the measured surface area between a disk electrode and cavity electrode, despite the fact that the cavity electrode should have a surface area only 70% of that of a disk. Determining surface area by the steady-state voltammetric limiting current relies on the assumption of a particular geometry, in this case a microdisk. When the actual geometry of the electrode deviates from the geometry assumed by equation 4, this technique can be insufficiently sensitive to distinguish subtle differences in surface area⁵⁰. The disk electrodes examined herein are beveled at a 45° angle, while the cavity electrodes have a glass shroud around the sensing surface. Both of these deviations from the flat-disk geometry alter the mass-transport regime, which likely masks any differences in limiting current in the voltammograms. Thus, increased surface area remains a possible contributor to the heightened sensitivity of the cavity electrodes over disk electrodes. Additionally, it is well-established that plasma-etching of carbon results in a higher oxygen-functionalization on the surface⁵¹⁻⁵⁵, and this is likely a contributor to the heightened sensitivity of these electrodes.⁵⁶

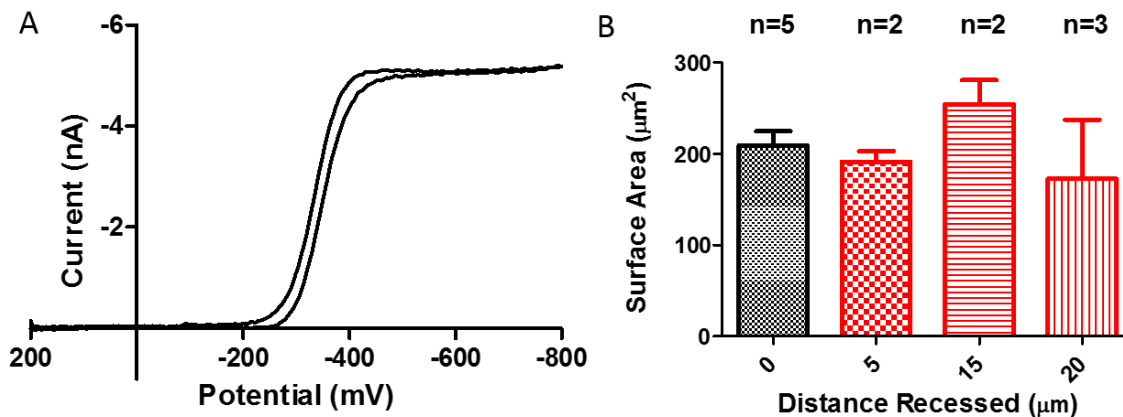


Figure 3.5 Voltammetric estimation of surface area. (A) Representative voltammogram collected on an etched cavity electrode. (B) Measured surface area using cyclic voltammetry in $\text{Ru}(\text{NH}_3)_6^{3+}$ for unetched disk electrode (black) and cavity electrodes (red) recessed 5, 15, and 20 μm . There is no significant difference in surface area (1-way ANOVA, $p > 0.05$, $n = 5, 2, 2, \text{ and } 3$, respectively).

3.3.4 Monitoring Neurotransmitter Release in Live Tissue

To assess the performance of the recessed carbon-fiber microelectrodes in tissue, a cavity electrode ($\sim 10 \mu\text{m}$ recessed) was placed into an acute rat brain slice encompassing the striatum, a region rich in dopaminergic terminals. A bi-polar stimulating electrode was placed in the vicinity of the working electrode and five biphasic electrical pulses (500 μA applied at 60 Hz) were used to evoke dopamine release. A representative colorplot is shown in Figure 3.6A, in which time is plotted on the x-axis, the applied potential on the y-axis, and the change in current from the background is depicted in false color. The time of electrical stimulation is indicated by the red arrow, and the release of approximately 2 μM dopamine was detected with a pre-calibrated electrode. The inset shows a voltammogram extracted at the vertical white line (white trace), overlaid with a normalized voltammogram collected in

the same preparation using a cylindrical carbon-fiber electrode (black trace), typically used for this type of experiment. The increased reductive/oxidative peak ratio is evident, similar to voltammograms collected *in vitro*. Figure 3.6B shows the normalized current vs. time trace extracted at the potential of dopamine oxidation, indicated by the horizontal white line in panel A. Much like the *in vitro* results, the current does not return to baseline after peak oxidation current is reached, demonstrating reduced mass transport of the evoked dopamine molecules in the cavity, relative to the trace collected using an unshielded cylindrical carbon-fiber electrode (also shown in Figure 3.6B). Importantly, these results show that the recessed electrodes can be used for studies in live brain tissue.

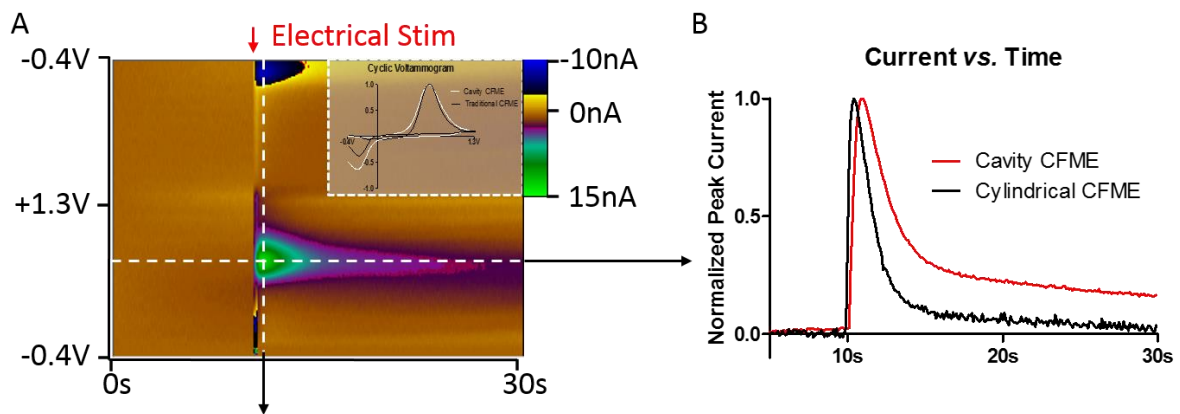
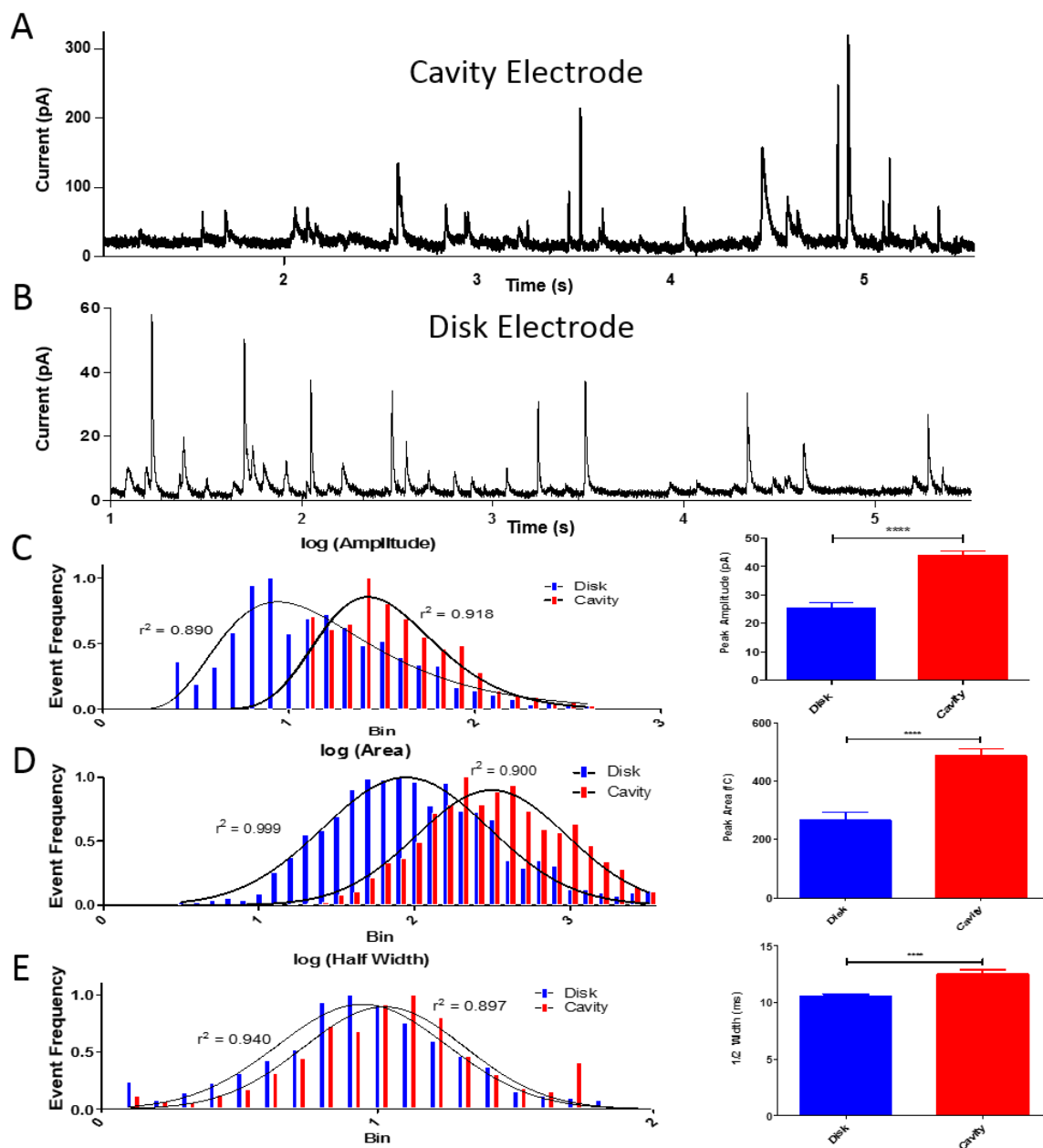


Figure 3.6 Diminished mass transport in live tissue. (A) A representative colorplot showing electrically stimulated (red arrow) dopamine release in striatal region of an acute brain slice. Inset: Normalized voltammograms comparing the data collected in this experiment (extracted at vertical white line) to data collected on a cylindrical CFME in the same preparation. (B) Normalized current vs. time traces showing the different response times of electrode geometries in this preparation. The response time is reflected in the rising portion of the current vs. time trace, showing slowed mass transport to the cavity electrode compared to a cylinder electrode.

3.3.5 Monitoring Individual Exocytotic Events at Single Cells

Finally, cavity electrodes were utilized for amperometry experiments at single bovine chromaffin cells in culture, detecting individual exocytotic events. These cells house dense core vesicles that contain catecholamines, and as such they are a widely used model for studying neurotransmission. Exocytosis was stimulated by picospritzing 100 mM K^+ solution onto the cell, and individual vesicular exocytotic events were monitored by holding the electrode at +0.8 V, such that released catecholamine molecules were oxidized at the electrode surface (Figure 3.7A and 3.7B). The number of molecules detected can be calculated using Faraday's law, $Q = nNF$, where Q is the charge measured under the peak, n is number of electrons transferred per oxidation event, N is number of molecules, and F is Faraday's constant. Experiments were performed using the traditional microdisk electrode, as well as with cavity electrodes recessed to a 5 μm depth. Average peak area, peak amplitude, and half-width were calculated for roughly 1,000 events at disk electrodes and cavity electrodes, and the data are plotted as histograms (Figure 3.7).

Figure 3.7 Amperometric recording of individual exocytotic events at single bovine chromaffin cells. (A) Representative amperometric trace collected on cavity electrode. (B) Representative amperometric trace collected on disk electrode. (C) Log transform of peak amplitude (pA) for disk (blue) and cavity (red) electrodes. Disk: mean = 25.5 ± 1.7 N=1387. Cavity: mean = 44.0 ± 1.6 N=845. $p < 0.0001$ (unpaired t-test), fit with log(Gaussian) regression, $r^2=0.890$ and 0.916 for disk and cavity, respectively. (D) Log transform of peak area (fC) for disk and cavity electrodes. Disk: mean = 265 ± 28.3 N=1387. Cavity: mean = 488 ± 21.2 N=845. $p < 0.0001$ (unpaired t-test), fit with Gaussian regression, $r^2=0.999$ and 0.900 for disk and cavity, respectively. (E) Log transform of peak half-width (msec) for disk and cavity electrodes. Disk: mean = 10.50 ± 0.209 N=1387. Cavity: mean = 12.50 ± 0.354 N=845. $p < 0.0001$ (unpaired t-test). Histograms are fit with Gaussian regression, $r^2=0.940$ and 0.897 for disk and cavity, respectively.



When compared to the traditional disk electrodes, cavity electrodes recorded exocytosis events with a higher amplitude (Figure 3.7C), larger area (Figure 3.7D), and greater half-width (Figure 3.7E). Half width is defined as peak width at half of maximum amplitude. When using amperometry, redox cycling does not occur as the potential is held at a constant oxidizing potential. Increased electron-transfer kinetics at the electrode are also not a likely explanation for the observed differences, since the peak area (charge) is directly attributed to the number of molecules detected. All molecules that collide with the electrode surface are expected to be consumed, so according to Faraday's law, the only explanation is that the cavity electrodes are detecting more molecules per event than the disk electrodes. Again, this is a result of the cavity confining molecules in the vicinity of the electrode surface, compared to the disk electrode where some molecules may diffuse away without reaching the electrode surface for oxidation. This shows that when doing amperometry at single cells with disk electrodes, some molecules that are released go undetected, leading to an underestimation of quantal size of the vesicles.

3.4 Conclusions

Recessed carbon-fiber microelectrodes were successfully and reproducibly fabricated by a plasma-etching procedure developed in-house. This approach allows normal CFME's to be made into cavity electrodes that are reliable and adaptable for use with FSCV and amperometry in various live-tissue preparations. The cavity electrodes are more sensitive to common analytes, such as dopamine when used with FSCV, and perform well in the brain slice preparation.

Additionally, when used with amperometry at single cells, cavity electrodes detect more molecules per release event than traditional disk electrodes. Raman spectroscopy revealed that the character of the microcrystalline carbon domains at the electrode surface are altered by electrochemical conditioning, but not significantly altered by the plasma-etching process. Scanning electron microscopy demonstrates a roughened surface at the plasma-etched electrodes, which likely increases the sensing surface area. Voltammetric data acquisition gains the added benefit of redox cycling resulting in signal amplification, evident by the increased reductive/oxidative peak ratio for the cavity electrodes over disk electrodes.

These electrodes have the potential to reveal new and important insights into cellular exocytosis, since they may detect events that were unresolved by traditional disk electrodes. In addition, these electrodes offer a more accurate estimation of the quantal size of each vesicle, compared to disk electrodes. An accurate estimation of quantal size is of the utmost importance with current research looking into fusion pore dynamics, and whether exocytosis results in full release of a vesicle's contents. These cavity electrodes combine the strengths of cylinder electrodes and disk electrodes for use with FSCV in the brain, offering higher

sensitivity than disk electrodes, with better spatial resolution than cylinder electrodes. This presents a major step forward in creating more sensitive electrodes without necessitating a complicated polymer coating procedure, while outperforming traditional carbon-fiber microelectrodes in both amperometry and FSCV experiments.

3.5 References

1. Leszczyszyn, D. J., Jankowski, J. A., Viveros, O. H., Diliberto, E. J., Jr., Near, J. A., and Wightman, R. M. (1990) Nicotinic receptor-mediated catecholamine secretion from individual chromaffin cells. Chemical evidence for exocytosis, *J Biol Chem* 265, 14736-14737.
2. Wightman, R. M., Jankowski, J. A., Kennedy, R. T., Kawagoe, K. T., Schroeder, T. J., Leszczyszyn, D. J., Near, J. A., Diliberto, E. J., Jr., and Viveros, O. H. (1991) Temporally resolved catecholamine spikes correspond to single vesicle release from individual chromaffin cells, *Proc Natl Acad Sci U S A* 88, 10754-10758.
3. Chen, T. K., Luo, G., and Ewing, A. G. (1994) Amperometric monitoring of stimulated catecholamine release from rat pheochromocytoma (PC12) cells at the zeptomole level, *Anal Chem* 66, 3031-3035.
4. Zerby, S. E., and Ewing, A. G. (1996) The latency of exocytosis varies with the mechanism of stimulated release in PC12 cells, *J Neurochem* 66, 651-657.
5. Zerby, S. E., and Ewing, A. G. (1996) Electrochemical monitoring of individual exocytotic events from the varicosities of differentiated PC12 cells, *Brain Res* 712, 1-10.
6. Omiatek, D. M., Cans, A. S., Heien, M. L., and Ewing, A. G. (2010) Analytical approaches to investigate transmitter content and release from single secretory vesicles, *Anal Bioanal Chem* 397, 3269-3279.
7. Li, X., Majdi, S., Dunevall, J., Fathali, H., and Ewing, A. G. (2015) Quantitative measurement of transmitters in individual vesicles in the cytoplasm of single cells with nanotip electrodes, *Angewandte Chemie* 54, 11978-11982.
8. Zhang, B., Adams, K. L., Lubner, S. J., Eves, D. J., Heien, M. L., and Ewing, A. G. (2008) Spatially and temporally resolved single-cell exocytosis utilizing individually addressable carbon microelectrode arrays, *Anal Chem* 80, 1394-1400.
9. Wang, J., and Ewing, A. G. (2014) Simultaneous study of subcellular exocytosis with individually addressable multiple microelectrodes, *Analyst* 139, 3290-3295.
10. Sombers, L. A., Hancher, H. J., Colliver, T. L., Wittenberg, N., Cans, A., Arbault, S., Amatore, C., and Ewing, A. G. (2004) The effects of vesicular volume on secretion through the fusion pore in exocytotic release from PC12 cells, *The Journal of neuroscience : the official journal of the Society for Neuroscience* 24, 303-309.

11. Dong, Y., Ning, G., Ewing, A. G., and Heien, M. L. (2014) Pituitary adenylate cyclase activating polypeptide modulates catecholamine storage and exocytosis in PC12 cells, *PloS one* 9, e91132.
12. Mellander, L. J., Trouillon, R., Svensson, M. I., and Ewing, A. G. (2012) Amperometric post spike feet reveal most exocytosis is via extended kiss-and-run fusion, *Sci Rep* 2, 907.
13. Trouillon, R., and Ewing, A. G. (2013) Amperometric measurements at cells support a role for dynamin in the dilation of the fusion pore during exocytosis, *Chemphyschem* 14, 2295-2301.
14. Trouillon, R., Lin, Y., Mellander, L. J., Keighron, J. D., and Ewing, A. G. (2013) Evaluating the diffusion coefficient of dopamine at the cell surface during amperometric detection: disk vs ring microelectrodes, *Anal Chem* 85, 6421-6428.
15. Dayton, M. A., and Wightman, R. M. (1980) Carbon-Fiber Microelectrodes as Invivo Voltammetric Probes of Endogenous Chemical Transmitter Concentration, *Clin Res* 28, A798-A798.
16. Armstrongjames, M., and Millar, J. (1979) Carbon-Fiber Micro-Electrodes, *J Neurosci Meth* 1, 279-287.
17. Roberts, J. G., Lugo-Morales, L. Z., Loziuk, P. L., and Sombers, L. A. (2013) Real-time chemical measurements of dopamine release in the brain, *Methods Mol Biol* 964, 275-294.
18. Cahill, P. S., Walker, Q. D., Finnegan, J. M., Mickelson, G. E., Travis, E. R., and Wightman, R. M. (1996) Microelectrodes for the measurement of catecholamines in biological systems, *Anal Chem* 68, 3180-3186.
19. Takmakov, P., Zachek, M. K., Keithley, R. B., Walsh, P. L., Donley, C., McCarty, G. S., and Wightman, R. M. (2010) Carbon microelectrodes with a renewable surface, *Anal Chem* 82, 2020-2028.
20. John, C. E., and Jones, S. R. (2007) Fast Scan Cyclic Voltammetry of Dopamine and Serotonin in Mouse Brain Slices, In *Front Neuroeng* (Michael, A. C., and Borland, L. M., Eds.), Boca Raton (FL).
21. Logman, M. J., Budygin, E. A., Gainetdinov, R. R., and Wightman, R. M. (2000) Quantitation of in vivo measurements with carbon fiber microelectrodes, *J Neurosci Methods* 95, 95-102.

22. Roberts, J. G., Moody, B. P., McCarty, G. S., and Sombers, L. A. (2010) Specific oxygen-containing functional groups on the carbon surface underlie an enhanced sensitivity to dopamine at electrochemically pretreated carbon fiber microelectrodes, *Langmuir : the ACS journal of surfaces and colloids* 26, 9116-9122.
23. Xiao, N., and Venton, B. J. (2012) Rapid, sensitive detection of neurotransmitters at microelectrodes modified with self-assembled SWCNT forests, *Anal Chem* 84, 7816-7822.
24. Michael, A. C., and Justice, J. B., Jr. (1987) Oxidation of dopamine and 4-methylcatechol at carbon fiber disk electrodes, *Anal Chem* 59, 405-410.
25. Plattner, H., Artalejo, A. R., and Neher, E. (1997) Ultrastructural organization of bovine chromaffin cell cortex-analysis by cryofixation and morphometry of aspects pertinent to exocytosis, *The Journal of cell biology* 139, 1709-1717.
26. Bond, A. M., Luscombe, D., Oldham, K. B., and Zoski, C. G. (1988) A Comparison of the Chronoamperometric Response at Inlaid and Recessed Disk Microelectrodes, *J Electroanal Chem* 249, 1-14.
27. Godino, N., Borrisse, X., Munoz, F. X., del Campo, F. J., and Compton, R. G. (2009) Mass Transport to Nanoelectrode Arrays and Limitations of the Diffusion Domain Approach: Theory and Experiment, *J Phys Chem C* 113, 11119-11125.
28. Fang, D., Jiang, D., Lu, H., Chiel, H. J., Kelley, T. J., and Burgess, J. D. (2009) Observation of Cellular Cholesterol Efflux at Microcavity Electrodes, *J Am Chem Soc* 131, 12038-+.
29. Henry, C. S., and Fritsch, I. (1999) Microfabricated recessed microdisk electrodes: characterization in static and convective solutions, *Anal Chem* 71, 550-556.
30. Ma, C. X., Contento, N. M., Gibson, L. R., and Bohn, P. W. (2013) Redox Cycling in Nanoscale-Recessed Ring-Disk Electrode Arrays for Enhanced Electrochemical Sensitivity, *Acs Nano* 7, 5483-5490.
31. Hu, M. J., and Fritsch, I. (2016) Application of Electrochemical Redox Cycling: Toward Differentiation of Dopamine and Norepinephrine, *Analytical Chemistry* 88, 5574-5578.
32. Hu, M. J., and Fritsch, I. (2015) Redox Cycling Behavior of Individual and Binary Mixtures of Catecholamines at Gold Microband Electrode Arrays, *Analytical Chemistry* 87, 2029-2032.

33. Tokuda, K., Morita, K., and Shimizu, Y. (1989) Cyclic Voltammetry at Microhole Array Electrodes, *Analytical Chemistry* 61, 1763-1768.
34. He, D. W., Yan, J. W., Zhu, F., Zhou, Y., Mao, B. W., Oleinick, A., Svir, I., and Amatore, C. (2016) Enhancing Bipolar Redox Cycling Efficiency of Plane-Recessed Microelectrode Arrays by Adding a Chemically Irreversible Interferent, *Anal Chem*.
35. Morita, K., and Shimizu, Y. (1989) Microhole Array for Oxygen-Electrode, *Analytical Chemistry* 61, 159-162.
36. Kawagoe, K. T., Zimmerman, J. B., and Wightman, R. M. (1993) Principles of Voltammetry and Microelectrode Surface-States, *Journal of Neuroscience Methods* 48, 225-240.
37. Bucher, E. S., Brooks, K., Verber, M. D., Keithley, R. B., Owesson-White, C., Carroll, S., Takmakov, P., McKinney, C. J., and Wightman, R. M. (2013) Flexible Software Platform for Fast-Scan Cyclic Voltammetry Data Acquisition and Analysis, *Analytical Chemistry* 85, 10344-10353.
38. Zachek, M., Takmakov, P., Moody, B., Wightman, R., and McCarty, G. (2009) Simultaneous Decoupled Detection of Dopamine and Oxygen Using Pyrolyzed Carbon Microarrays and Fast-Scan Cyclic Voltammetry, *Analytical Chemistry* 81, 6258-6265.
39. Lemos, J. C., Wanat, M. J., Smith, J. S., Reyes, B. A., Hollon, N. G., Van Bockstaele, E. J., Chavkin, C., and Phillips, P. E. (2012) Severe stress switches CRF action in the nucleus accumbens from appetitive to aversive, *Nature* 490, 402-406.
40. Roitman, M. F., Wheeler, R. A., Wightman, R. M., and Carelli, R. M. (2008) Real-time chemical responses in the nucleus accumbens differentiate rewarding and aversive stimuli, *Nat. Neurosci.* 11, 1376-1377.
41. Boylestad, R. L. (2000) *Introductory circuit analysis*, 9th ed., Prentice Hall, Upper Saddle River, N.J.
42. Bard, A. J., and Faulkner, L. R. (2001) *Electrochemical methods : fundamentals and applications*, 2nd ed., Wiley, New York.
43. Ribeiro-Soares, J., Oliveros, M. E., Garin, C., David, M. V., Martins, L. G. P., Almeida, C. A., Martins-Ferreira, E. H., K. Takai, T. E., Magalhaes-Paniago, R., Malachias, A., Jorio, A., Archanjo, B. S., Achete, C. A., and Cancado, L. G. (2015) Structural Analysis of Polycrystalline Graphene Systems by Raman Spectroscopy, *Carbon* 95, 646-652.

44. Ferrari, A., and Robertson, J. (2000) Interpretation of Raman spectra of disordered and amorphous carbon, *Physical Review B* 61, 14095-14107.
45. McCulloch, D. G., and Prawer, S. (1995) The Effect of Annealing and Implantation Temperature On the Structure of C Ion-Beam-Irradiated Glassy Carbon, *Journal of Applied Physics* 78, 3040-3047.
46. Ferrari, A. C. (2007) Raman spectroscopy of graphene and graphite: Disorder, electron-phonon coupling, doping and nonadiabatic effects, *Solid State Communications* 143, 47-57.
47. Pimenta, M. A., Dresselhaus, G., Dresselhaus, M. S., Cancado, L. G., Jorio, A., and Saito, R. (2007) Studying disorder in graphite-based systems by Raman spectroscopy, *Physical Chemistry Chemical Physics* 9, 1276-1291.
48. Wang, Y., Alsmeyer, D. C., and McCreery, R. L. (1990) Raman-Spectroscopy Of Carbon Materials - Structural Basis Of Observed Spectra, *Chemistry of Materials* 2, 557-563.
49. Baur, J. E., and Wightman, R. M. (1991) Diffusion-Coefficients Determined with Microelectrodes, *Journal of Electroanalytical Chemistry* 305, 73-81.
50. Watkins, J. J., Chen, J., White, H. S., Abruna, H. D., Maisonhaute, E., and Amatore, C. (2003) Zeptomole voltammetric detection and electron-transfer rate measurements using platinum electrodes of nanometer dimensions, *Anal Chem* 75, 3962-3971.
51. Naseh, M. V., Khodadadi, A. A., Mortazavi, Y., Pourfayaz, F., Alizadeh, O., and Maghrebi, M. (2010) Fast and clean functionalization of carbon nanotubes by dielectric barrier discharge plasma in air compared to acid treatment, *Carbon* 48, 1369-1379.
52. Coen, M. C., Keller, B., Groening, P., and Schlapbach, L. (2002) Functionalization of graphite, glassy carbon, and polymer surfaces with highly oxidized sulfur species by plasma treatments, *Journal of Applied Physics* 92, 5077-5083.
53. Dongil, A. B., Bachiller-Baeza, B., Guerrero-Ruiz, A., Rodriguez-Ramos, I., Martinez-Alonso, A., and Tascon, J. M. D. (2011) Surface chemical modifications induced on high surface area graphite and carbon nanofibers using different oxidation and functionalization treatments, *J Colloid Interf Sci* 355, 179-189.
54. Yang, L. F., Shi, Z., and Yang, W. H. (2014) Enhanced capacitive deionization of lead ions using air-plasma treated carbon nanotube electrode, *Surf Coat Tech* 251, 122-127.

55. Epifanio, M., Inguva, S., Kitching, M., Mosnier, J. P., and Marsili, E. (2015) Effects of atmospheric air plasma treatment of graphite and carbon felt electrodes on the anodic current from *Shewanella* attached cells, *Bioelectrochemistry* 106, 186-193.
56. Roberts, J. G., Moody, B. P., McCarty, G. S., and Sombers, L. A. (2010) Specific Oxygen-Containing Functional Groups on the Carbon Surface Underlie an Enhanced Sensitivity to Dopamine at Electrochemically Pretreated Carbon Fiber Microelectrodes, *Langmuir : the ACS journal of surfaces and colloids* 26, 9116-9122.

CHAPTER 4

Intracellular Chemical Measurements Using Nanocone Electrodes

This work was completed in collaboration with: Roberts, J.G., and Sombers, L.A.

4.1 Introduction

Single cells have been used extensively as models for studying exocytosis, the primary method by which cellular communication occurs.¹⁻³ During exocytosis, vesicles containing chemical messengers fuse with the cell membrane where they subsequently release all or a portion of their contents into the extracellular space.^{4, 5} These messengers are then able to bind with receptors on the surface of neighboring cells to propagate and regulate chemical communication. Since electrochemical approaches are able to provide excellent temporal and spatial resolution they have proven popular for studying this system.

Carbon-fiber microelectrodes are the most commonly used electrode substrate when studying the dynamics of exocytosis at single cells. In general, these disk electrodes are approximately 10 μm in diameter and sealed in a glass capillary and the exposed carbon surface is placed directly on top of the cell.⁶ This positioning of the electrode limits molecular diffusion and increases the likelihood of measuring release events. Although it is less common, attempts have been made at acquiring electrochemical measurements *in* the cell cytosol. For example, 2 μm platinum disk electrodes have been inserted into giant snail neurons and voltammetry was used to monitor transport of dopamine bathed onto the cell as

it crossed the cell membrane.⁷ However, the slow scan rates employed significantly limited the temporal resolution and precluded qualitative analyte identification.

The ability to make intracellular measurements greatly expands the dimensionality of chemical information about the release, uptake, and packaging of neurotransmitters. One key aspect for the limited attempts of researchers at obtaining intracellular measurements extends largely from the difficulty of developing a stable electrode with the proper geometry to enable placement inside a single cell without causing extensive damage. As noted above, the diameter of carbon fibers are approximately 10 μm , which is roughly the same size as many cells, therefore it is necessary to reduce the size of the electrode in order to fit within the confines of the cell. Ewing et. al. have recently implanted a flame etched carbon-fiber electrode within the cytosol of PC12 cells.⁸ When implanted, they observed amperometric spikes that resembled individual vesicular exocytosis events, which was perplexing. It was determined that the vesicles could collide with the electrode and subsequently lyse, releasing their contents onto the electrode surface.^{9, 10} By comparing the amount of neurotransmitter released intracellularly to that measured during exocytosis with a classic extracellular amperometric measurement of exocytosis, they determined that only a portion of the vesicle content is released during the exocytosis process in PC12 cells.

Electrochemical measurements made at single cells generally use amperometric detection, where the potential is held constant. Amperometry provides excellent sensitivity for measuring low quantities of analyte, and is unmatched in its temporal response, which is needed for measuring fast exocytotic events. However, this electrochemical technique provides almost no qualitative information as to what analyte is being detected.

Voltammetry on the other hand, by dynamically scanning through a range of potentials to drive redox reactions, leads to oxidation and/or reduction peaks that can be used for analyte identification. This chemical selectivity is important because cells contain many different electroactive compounds and it is imperative to identify what molecule is detected. For example, voltammetry has proven capable of distinguishing and quantifying both serotonin and histamine released from mast cells.^{11, 12} Similarly, chromaffin cells are known to contain both norepinephrine and epinephrine, which are capable of being detected electrochemically. These two neurotransmitters are structurally similar, and the enzymatic conversion of norepinephrine to epinephrine takes place within the cell via phenylethanolamine N-methyltransferase (PNMT).^{13, 14} It has been shown that this conversion does not occur with 100 percent efficiency, and that a single chromaffin cell can contain a mixture of norepinephrine and epinephrine.^{15, 16} Amperometric detection of exocytosis events at chromaffin cells can quantify the total content released; however, conclusions cannot be drawn about the concentration of these individual analytes. Voltammetry, however, is able to provide sufficient selectivity between norepinephrine and epinephrine and has been used to distinguish between the two molecules during exocytotic release events.¹⁶⁻¹⁸

In this work, we developed a method to create carbon-fiber microelectrodes with a novel ‘nanocone’ geometry. The length of the exposed electrode surface area was controllable. These innovative electrodes were then used to penetrate the cell wall of chromaffin cells and to subsequently identify and quantify intracellular vesicle content. Intracellular measurements using voltammetry with slow scan rates have been attempted

before, but to our knowledge, fast scan cyclic voltammetry (FSCV) has never been shown intracellularly.^{7, 19, 20} We sought to advance this field by adding a voltammetry technique with chemical selectivity, and highlight the utility of FSCV for making measurements intracellularly. Additionally, we used an extended voltammetric waveform to successfully distinguish the release of norepinephrine and epinephrine from vesicles as they adsorbed and lysed onto the electrode surface in the cytosol. The capability to qualitatively identify cytosolic neurotransmitters in real time has never been shown before and will permit exciting new studies about the dynamics of the vesicular packaging of these molecules and the effects of pharmacology on single cells from a new perspective.

4.2 Experimental Section

4.2.1 Chemicals

All chemicals were purchased from Sigma Aldrich Co. (St. Louis, MO) and used without additional processing. Aqueous solutions were made using doubly deionized water (Barnstead Easy Pure II, Dubuque, IA). Experiments done in a flow injection apparatus were carried out in phosphate-buffered saline (0.1 M PBS) at pH 7.4.

4.2.2 Electrode Fabrication

Cylindrical carbon-fiber microelectrodes were constructed using t-650 carbon fibers as previously described.²¹ Briefly, a single carbon fiber was aspirated into a glass capillary (1.0 mm x 0.5 mm, A-M Systems, Carlsburg, WA). A tapered seal was subsequently formed by using a micropipette puller (Narishige, Tokyo, Japan). An electrical connection was made

with the fiber by coating a lead in silver paint (Silver Print II, GC Electronics) and inserting it into the back of the electrode. The exposed carbon fiber was next etched into a conical geometry by rapidly dipping and extracting the electrode into 4 M KOH while applying a +7 V potential (3B Scientific, U33020, Tucker, GA) to the carbon electrode, versus a platinum wire. The formulation for the polymer insulation has been previously described.²² The tip of the electrode was masked, to prevent insulation, by inserting it into a conductive silicon rubber (SSP1529 0.080, Specialty Silicone Products, Ballston Spa, NY, generous gift provided courtesy of Marian Inc. Salem, VA). A micromanipulator was used to raise the silicon rubber mask onto the electrode surface. The depth of the masked portion of the electrode was monitored by measuring the impedance of the electrode/rubber interface with a lock-in amplifier (7280, Ametek, Inc., Berwyn, PA). After the electrode was masked to the desired depth, the phenolic polymer insulation solution was electrodeposited onto the exposed carbon surface. A +4 V potential was applied to the carbon electrode, versus a platinum electrode, for 14 minutes. The electrode was removed from the mask and oven dried at 150 °C for 30 minutes. For electrode images, the electrodes were coated with a 60/40 gold/palladium alloy prior to imaging with a scanning electron microscope.

4.2.3 Flow Injection

Electrochemical data were collected using a flow injection apparatus that was housed within a custom built Faraday cage to reduce noise interference. The working electrode was positioned in the electrochemical cell using a micromanipulator (World Precision Instruments, Inc., Sarasota, FL). Buffered electrolyte was passed continuously over the

working and reference electrode at 1 mL/min using a syringe pump (New Era Pump Systems, Inc., Wantagh, NY). A digital valve interface (Valco Instruments Co., Inc., Houston, TX) was used to control an air actuator connected to a six-port HPLC valve in order to introduce two-second bolus injections of analyte across the working electrode.

4.2.4 Electrochemical Data Acquisition

All potentials were reported versus a Ag/AgCl (World Precision Instruments, Inc., Sarasota, FL) reference electrode. Analyte detection with FSCV was accomplished using triangular waveforms applied with an application frequency of 10 Hz. Waveform potentials were applied and current transduction was accomplished using custom instrumentation (University of North Carolina at Chapel Hill, Department of Chemistry, Electronics Facility). Waveforms were output using a DAC/ADC card (NI 6251 M) with TH-1 software (ESA, Chelmsford, MA). The flow injection system was coordinated with the electrochemical experiment using a second card (NI 6711). Background subtraction and signal averaging was software controlled. For amperometry experiments, electrodes were held at +850 mV using a patch-clamp amplifier (Axopatch 200B, Molecular Devices, LLC., Sunnyvale, CA). Current output was filtered with a four-pole low-pass Bessel filter. An Axon Digidata 1440A (Molecular Devices) was used to digitize data at 2 kHz. The amplifier was set to voltage-clamp mode in Whole Cell ($\beta = 1$) configuration. Axoscope software (version 10.4.1.9, Molecular Devices) was used to collect the amperometric data.

4.2.5 Primary Bovine Chromaffin Cell Culture

Bovine adrenal glands were obtained from a local slaughterhouse to establish primary culture. Adrenal glands were immediately trimmed of excess fat, perfused with cold W3 through the adrenal vein, and submerged in ice-cold W3 buffer (145 mM NaCl, 5.4 mM KCl, 1 mM NaH₂PO₄, 11.2 mM glucose, and 15 mM HEPES) until they were in the lab to be further processed. The glands were then trimmed of remaining fat and perfused with warm W3, incubated at 37 °C for 10 minutes and washed with W3. This wash was repeated three times. Glands were then perfused with a digestion mixture containing 0.035 mg/mL DNAase and 1.4 mg/mL collagenase in W3 and incubated for 15 minutes. This perfusion was repeated three more times. Nystatin (5 mL/L) in W3 solution was used for the remainder of the steps involving W3. The medullae were then removed from the glands, finely minced, placed in warm digestion mixture, and stirred for 30 minutes. The digested solution was filtered (100 µm) and centrifuged to pellet the cells. Pellets were resuspended in W3 and mixed with a Percoll gradient (90% Percoll, 10% 10x W3 solution). The Percoll gradient was centrifuged to separate red blood cells, chromaffin cells, and cellular debris. The chromaffin cell layer, formed in the middle, was collected and filtered through a 40 µm sterile nylon filter. The filtrate was added to DMEM (Dulbecco's Modified Eagle Medium) and centrifuged to pellet the cells. Supernatant was removed and the pellets were resuspended in DMEM containing 10% FBS and 1% 100X Pen-strep. Cells were then plated on 35 mm culture dishes, and placed in the incubator for at least three days prior to experimentation. Cell media was changed every two days.

4.2.6 Single Cell Experiments.

Cells were prepared for electrochemical measurements by replacing the medium with an isotonic buffer (150 mM NaCl, 5 mM KCl, 1.2 mM MgCl₂, 5 mM glucose, 10 mM HEPES, and 2 mM CaCl₂ at pH 7.4). To elicit exocytosis, a high potassium isotonic stimulating buffer (55 mM NaCl, 100 mM KCl, 1.2 mM MgCl₂, 5 mM glucose, 10 mM HEPES, and 2 mM CaCl₂) was loaded into a micropipette and puffed onto the cell with a 3 second, 20 psi pulse (Picospritzer II; General Valve Corporation, Fairfield, NJ). The culture dish containing the cells was maintained at 37 °C using a culture dish incubator (DH-35iL; Warner Instruments, LLC., Camden, CT). Images of cells were collected on an inverted microscope (Olympus IMT-2) using a 40x objective.

4.2.7 Data Analysis

Amperometric peak areas were quantified using Mini Analysis software (version 6.0.3, Synaptosoft). The limit of detection was defined as three times the standard deviation of the noise. Data is reported as the mean \pm standard error of the mean. Graphical and statistical analysis was performed with Graph Pad Prism 5 (GraphPad Software, Inc., La Jolla, CA).

4.3 Results and Discussion

4.3.1 Electrode Fabrication

In order to successfully place the electrode within the cell cytosol it was necessary to both reduce the size of the electrode and alter its geometry so that it could penetrate the cell

wall. Single chromaffin cells have diameters of approximately 20 μm whereas carbon fibers have a diameter of approximately 10 μm .²³ Various techniques for reducing electrode size, such as flame etching, have been proposed elsewhere with varying success.²⁴⁻²⁶ For this work we chose to use a wet etching procedure that has proven to be effective, reproducible, and easily implemented (Figure 4.1). The carbon fiber electrode was lowered into a solution of 4M potassium hydroxide, while a positive potential of 7 V was applied to the electrode. The electrode was then removed from the solution where the applied potential was sufficient to rapidly etch the carbon. The dipping of the electrode is essential to form a conical geometry, as the tip of the electrode experiences a longer etch time than the rest of the carbon surface. If the voltage is higher or the plunging speed is slow, the immersed section of the fiber etches completely to create a blunt end.

An optical image of a representative electrode after the etching procedure is shown in Figure 4.1B. It can be seen how the fiber tapers toward the tip of the electrode to form a conical geometry with a sharp point. With this modified electrode design it became feasible to insert the electrode into cells.

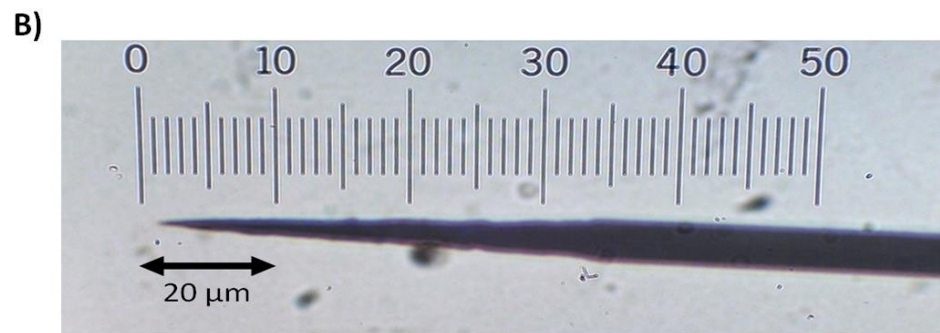
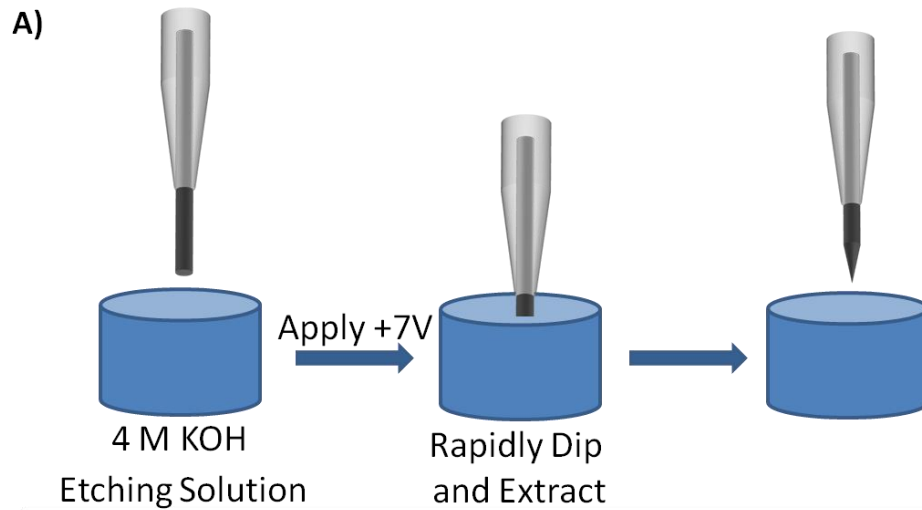


Figure 4.1 Wet etching provides a facile means for producing conical electrodes. A) Schematic depicting the wet etching process. A carbon fiber cylinder electrode is positioned directly above a solution of 4 M KOH. A potential of +7 V is applied to the carbon electrode, as it is rapidly lowered into and raised out of solution leaving the carbon fiber with a conical geometry. B) Representative optical image of an etched electrode with a conical geometry.

Even though this design made it possible to penetrate the cell wall to access the cytoplasm, a large portion of electroactive surface area remained outside of the cell. With portions of the electrode both inside and outside of the cell it would be difficult to distinguish electrochemical events occurring intra vs. extracellularly. One option to address this problem

was to remove calcium from the buffer. Without extracellular calcium present the cell would be unlikely to undergo exocytosis and any measured events could be assumed to result from vesicular lysing. However, exocytotic events generated in response to intracellular calcium stores could not be ruled out. Another approach was to insulate any electroactive portion of the electrode that would not be inserted into the cell. If the entirety of the electroactive electrode area was positioned in the cytosol, then any recorded events would necessarily be generated intracellularly.

Various attempts have been published for insulating carbon-fiber microelectrodes such that the entire fiber is insulated and the carbon tip is subsequently exposed, or an extended length of exposed carbon protrudes from the insulation and is cut to length after the insulation process.^{21, 27} These traditional approaches are not appropriate for this work, as the tip is created prior to insulation, and the remainder of the carbon must be subsequently insulated. To address this problem, the electrode tip was positioned in silicone rubber using a micropositioner, and a lock-in amplifier was used to measure the impedance across the interface and to quantify depth (Figure 4.2A). An insulating solution was dropped onto the silicon surface and a platinum reference wire was inserted in the solution next to the carbon electrode. The insulating solution was electropolymerized onto the carbon fiber to form a uniform insulating layer along the length of the exposed carbon fiber except for the masked electrode tip (Figure 4.2B). Since most chromaffin cells are approximately 20 μm or greater in diameter we determined that a sensing length of 5 μm of exposed carbon would work well for intracellular studies. A representative electrode that underwent the etching and insulation

procedure is shown in Figure 4.3. This electrode was tapered to a diameter of ~ 300 nm. A slight ridge $5 \mu\text{m}$ from the tip indicates where the insulation formed on the electrode,

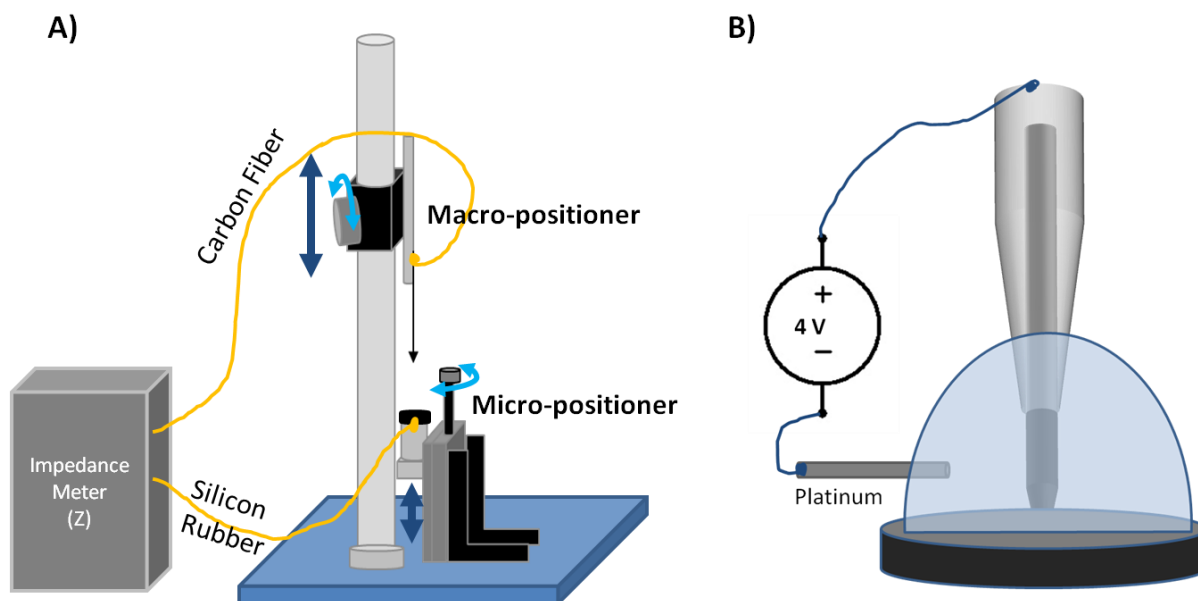


Figure 4.2 Electrodes are masked and insulated. A) Diagram of the unit used to insulate the exposed carbon. An impedance meter is used to indicate when the carbon is directly above the conductive silicon rubber. Macro- and micro-positioners are used to move the carbon fiber and the silicon rubber, respectively in a vertical direction. B) Magnified view of the carbon fiber inserted into the silicon rubber. Once the fiber is masked to the desired length, a drop of polymer solution is placed and a platinum reference electrode is inserted, the insulation is electropolymerized around the fiber.

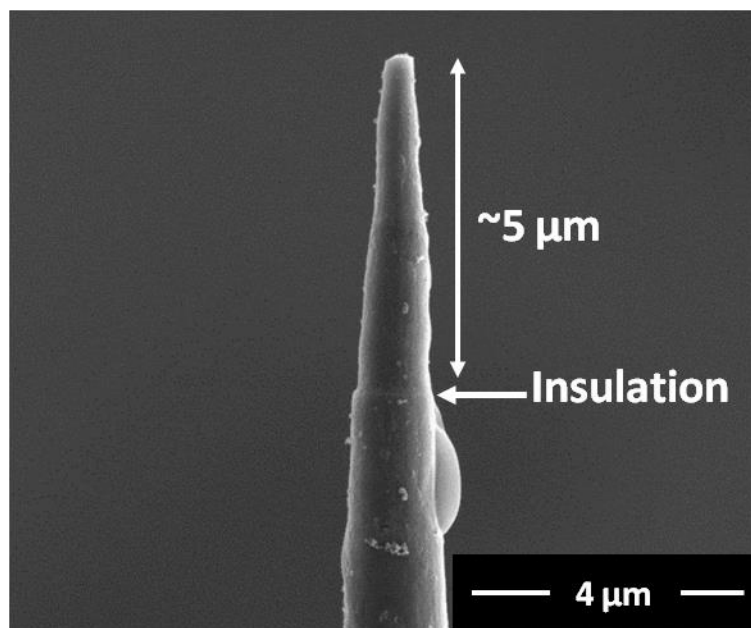


Figure 4.3 Scanning electron micrograph of an insulated conical carbon fiber. The carbon fiber is tapered to a sharp point at the tip which is necessary for insertion into cells. A thin rim of insulation can be seen $\sim 5 \mu\text{m}$ from the tip.

Before using these new electrodes for intracellular studies, we electrochemically characterized the electrodes *in vitro*, to assess their performance. Carbon-fiber electrodes are often electrochemically conditioned by repeatedly applying the potential waveform across the electrode for 10 to 20 minutes. This procedure serves to both stabilize chemical functionalities on the electrode surface and enhance analyte detection. As we conditioned these electrodes it was observed that the performance never stabilized, but instead the background voltammograms collected during the preconditioning phase gradually increased in magnitude. Steady state background current generated during a potential sweep is directly proportional to capacitance, which is dependent on electrode area (Equation 1).²⁸

$$\text{Equation 1} \quad |i_c| = C_d v$$

Thus it was determined that the insulation was not stable, and slowly dissociating from the electrode surface.

Several strategies were evaluated to improve the stability of the insulation, including thicker insulations, and altering the ratio of the components of the polymerization solution, with limited success. Thus, we reinforced the polymer insulation by adding a second insulator. Wax coatings have been shown previously to work as a sealant material for glass insulated carbon electrodes.²⁹ As a means to reinforce the polymer coating and prevent degradation, we encased the electrode tip in paraffin wax. This coated the entire tip, including the bare carbon, effectively preventing any electron transfer at the electrode surface. Figure 4.4A is the voltammogram of dopamine (1 μM) that was collected using an electrode with the wax coating. There were no identifiable redox features present in this voltammogram, indicating that the entire carbon surface was insulated. Subsequent electrochemical conditioning removes the wax at the sensor surface. Indeed, the same electrode used in Figure 4.4A was able to record current from the oxidation and reduction of dopamine after conditioning for approximately 10 minutes (Figure 4B).

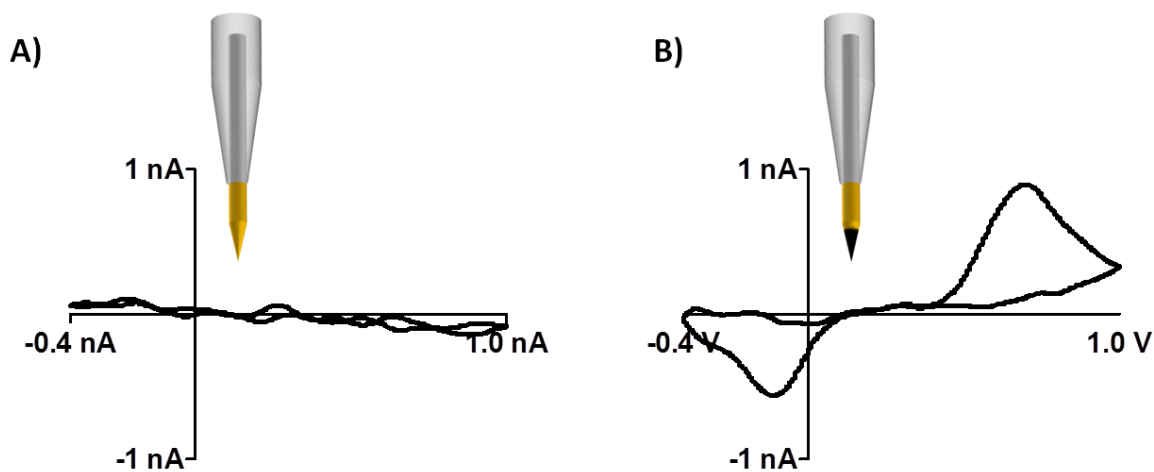


Figure 4.4 Wax coating was removed with repeated application of waveform. A) No oxidation or reduction of dopamine was observed when the electrode was fully coated in wax. B) A dopamine voltammogram showing clear oxidation and reduction peaks was observed after the wax had been removed from the portion of the fiber without the phenolic insulation.

4.3.2 Electrochemical Characterization

Insulation stability was assessed by monitoring dopamine oxidation current for three hours, at 15 min intervals. If the insulation failed, then the exposed surface area would increase and an increase in the oxidation current from dopamine would be observed, as peak current is proportional to surface area. After three hours of cycling the electrode, dopamine oxidation current remained stable ($p < 0.05$, two-tailed t-test, Figure 4.5). These results indicate that the insulation is able to prevent redox processes from the bulk solution and this insulation was stable over the course of the experiment.

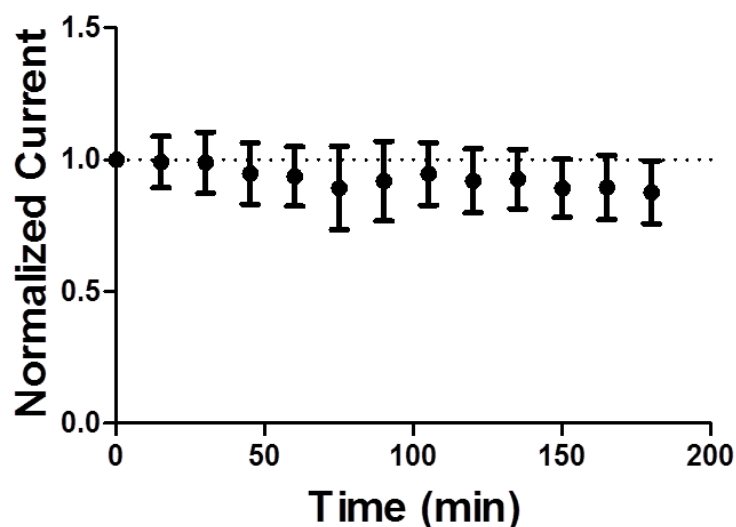


Figure 4.5 Electrodes with polymer and wax bilayer insulation show a stable response. The normalized oxidation current in response to 1 μM dopamine is plotted against collection time (N=3 electrodes). Data was normalized to the time zero response.

Fundamental electrochemistry principles dictate that the redox current generated is proportional to the scan rate (ν) of the applied waveform (Equation 2).²⁸

$$\text{Equation 2} \quad i_p = \frac{n^2 F^2}{4RT} \nu A \Gamma$$

Figure 4.6A highlights representative dopamine voltammograms collected using the same electrode but with varying scan rates. It can be seen that the peak current increases as the scan rate is raised from 400 to 2000 V/s. Additionally, a phenomena observed with molecules that have quasi-reversible electron transfer kinetics, such as dopamine, is that the separation of the oxidation and reduction peaks increases as the scan rate is increased. Figure 4.6B shows normalized dopamine voltammograms collected at different scan rates, so that

the shift in peak potentials could be seen more clearly. As expected the separation between the oxidative and reductive peaks increases with increasing scan rate. These data show that the electrodes behave according to principle and that the insulation does not interfere with the detection of dopamine.

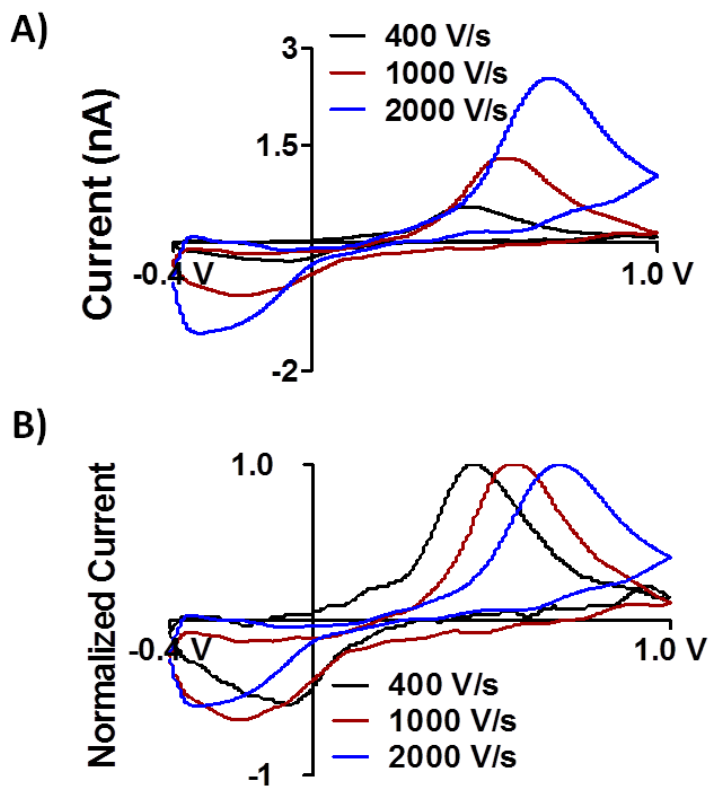


Figure 4.6 Electrochemical characterization of dopamine at conical electrodes. A) Representative voltammograms of 2 μM dopamine at multiple scan rates (blue line = 2 kV/s, red = 1 kV/s, black = 400V/s). B) Voltammograms shown in (A) that have been normalized to the oxidation peak.

As stated in the introduction, amperometry is the most commonly used electrochemical technique for measuring exocytosis at single cells. Therefore, we first

utilized amperometry to ensure that our electrodes behaved as anticipated when used to measure exocytotic events at cultured cells. With the conical electrode positioned on the surface of a cultured chromaffin cell, no electrochemical activity was recorded unless it was chemically stimulated. Figure 4.7 shows a representative amperometric recording. To stimulate exocytosis, 100 mM KCl was puffed onto the cell. Exocytotic events were recorded, indicating that the electrode had sufficient sensitivity to quantify vesicle release with amperometry.

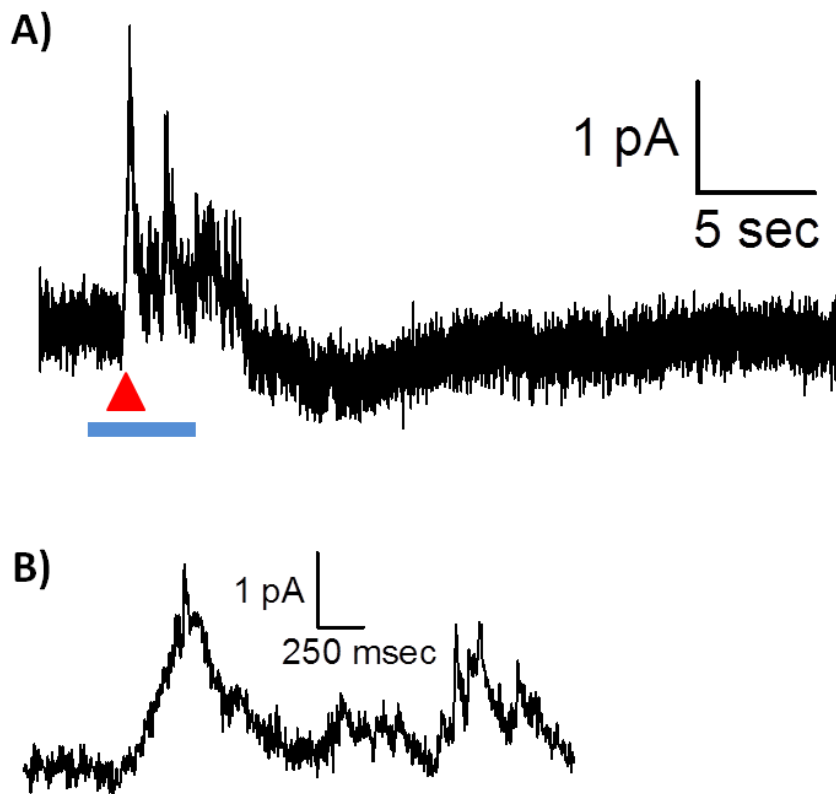


Figure 4.7 Conical electrodes detect individual exocytotic events at single cells. A) Amperometric trace recorded during potassium stimulation. The red triangle indicates the time of KCl stimulation. B) Expanded view of the region highlighted by the blue bar in Panel A.

In order to make intracellular chemical measurements, the electrode was inserted into the cell cytoplasm (Figure 4.8). Figure 4.8A shows an electrode positioned next to a cell, ready for insertion. The tip of the electrode was pressed against the cell wall and in Figure 4.8B this pressure caused an indentation of the cell wall (Figure 4.8B). Cells were chosen that were firmly attached to the bottom of the plate, to ensure that the cell would accept the force of the electrode. After enough pressure was applied, the electrode penetrated the cell wall and entered the cytoplasm, forming a seal around the electrode (Figure 4.8C). From this position it was possible to make chemical measurements intracellularly.

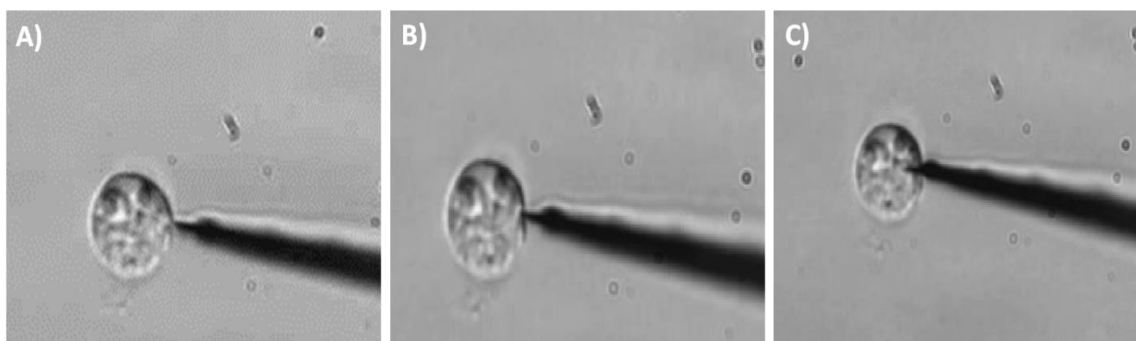


Figure 4.8 Insertion of an electrode into a single cell. A) The electrode is placed near the cell, B) pressed against the cell membrane, and C) inserted into the cell cytoplasm.

For the initial intracellular testing, we used amperometric detection to reproduce a previous finding that reported that vesicles could collide with the electrode and lyse, allowing the content to be amperometrically detected.⁸ The amperometric trace shown in Figure 4.9 was collected as the electrode moved from outside to inside the cell. The shift in the baseline is the result of moving the electrode from the buffered solution into the cytoplasm, where it

encounters a different chemical environment and is further removed from the reference electrode (positioned in the extracellular buffer). Upon entry to the cytoplasm, several amperometric spikes were observed (Figure 4.9). These correspond to individual vesicles colliding with the electrode and lysing, such that the chemical content could be detected. As shown in the inset (Figure 4.9B), these events have sharp rise and decay times, similar to exocytotic events observed with an electrode positioned extracellularly.

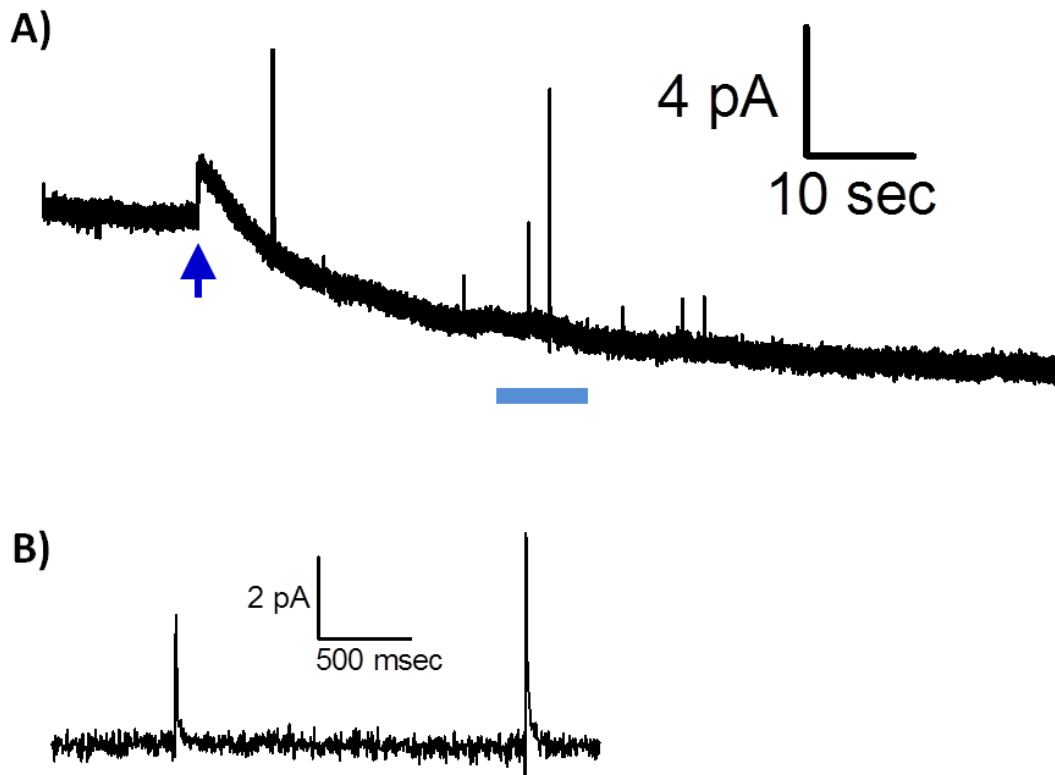


Figure 4.9 Amperometric detection of intracellular vesicle content. A) Amperometric trace recorded during cellular penetration. The blue arrow indicates the time point when the electrode gained access to the cytosol. B) Expanded view of the region highlighted by the blue bar shown in Panel A.

4.3.3 Intracellular Voltammetry

Although amperometry offers outstanding benefits for measuring release events, it does not provide information on chemical identity. By contrast voltammetry offers some qualitative information that can be used for analyte identification.¹⁷ Thus, we sought to extend the utility of our electrodes by coupling them with FSCV to make both qualitative and quantitative chemical measurements. The Axopatch potentiostat is commonly used to make electrochemical measurements at single cells because of the low-noise electronics that it utilizes. The increased signal to noise that can be attained with this instrument is valuable when trying to measure low concentrations of analytes. Therefore, for our initial investigation we used this Axopatch system. Unfortunately, the maximal potential output of the instrument is +1.0 V, so the applied waveform was limited to a 1.0V switching potential. However, higher positive potential limits result in greater sensitivity to catecholamines.^{30, 31}

Figure 4.10 shows representative data collected using FSCV, rather than amperometry, at the time that the cell was penetrated using the nanocone electrode. Upon insertion into the cell, discrete vesicular release events were recorded as shown in the color plot (Figure 4.10A). The current collected at +0.75 V, the potential where peak current for catecholamines is collected, is shown in Figure 4.10C. It is important to recognize that the peaks clearly resemble those seen with amperometric detection (Figures 4.7 and 4.9). Figure 4.10B shows a voltammogram that was taken during one of the release events (vertical dashed line in Figure 4.10A). The oxidation and reduction peaks identify the analyte as a catecholamine. Although we cannot distinguish norepinephrine and epinephrine using this

voltammetric waveform, the result is very promising in that it demonstrates the feasibility of intracellular FSCV.

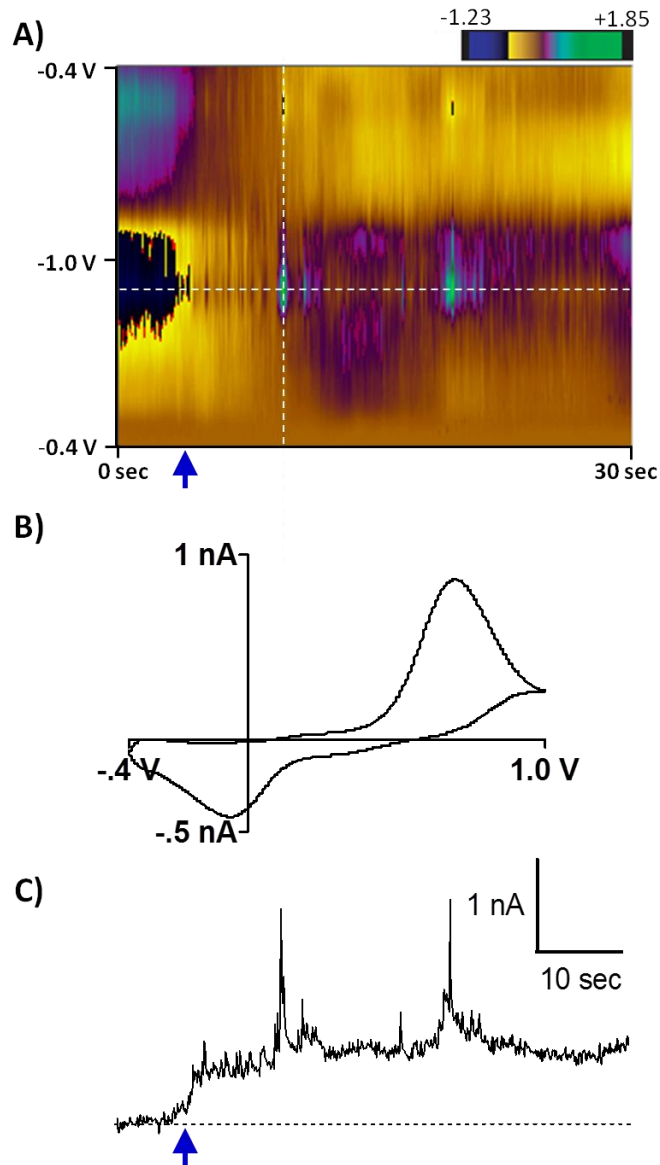


Figure 4.10 Intracellular voltammetry. A) Colorplot recorded during insertion of the electrode into the cell cytoplasm. The blue arrow indicates the time of membrane penetration. B) Voltammogram taken from (A) indicated by the vertical white dashed line. The voltammograms show a clear catecholamine signal. C) Current versus time trace taken at the potentials shown by the horizontal white dashed line in (A). The blue arrow indicates insertion into the cell.

The primary catecholamines present in chromaffin cells are norepinephrine and epinephrine. Due to their structural similarities, they produce voltammograms with oxidation and reduction peaks that are identical within the potential limits shown in the previous experiment. However, Wightman and coworkers have shown previously that a second oxidation peak for epinephrine can be observed if the applied potential is extended to approximately +1.425 V.¹⁷ Custom instrumentation was used to apply an extended waveform of +0.1 V to +1.45 V. Figure 4.11 shows representative voltammograms that demonstrate that the oxidation of norepinephrine results in a single peak, but oxidation of epinephrine clearly generates two separate peaks with this waveform. The first peak at approximately +0.65 V is thought to originate from oxidation of the hydroxyl groups to an o-quinone, and the second peak at +1.45 V arises from oxidation of the secondary amine (Scheme 1). Thus, this second peak provides a marker to distinguish norepinephrine and epinephrine contained in the vesicles.

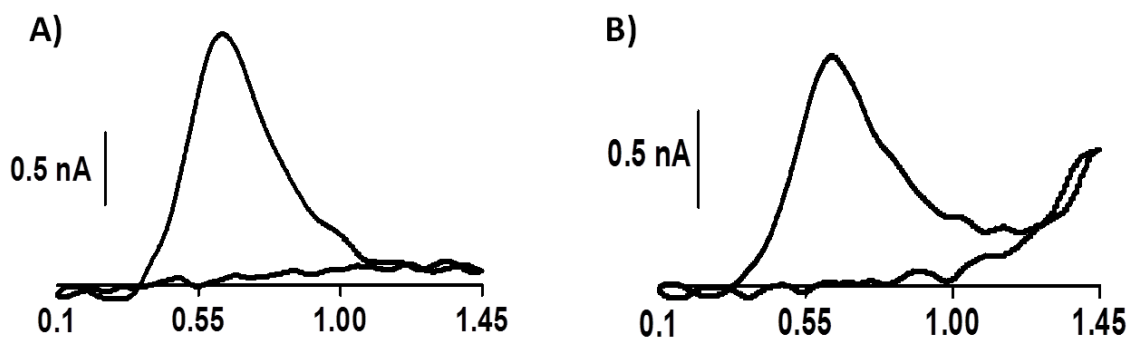
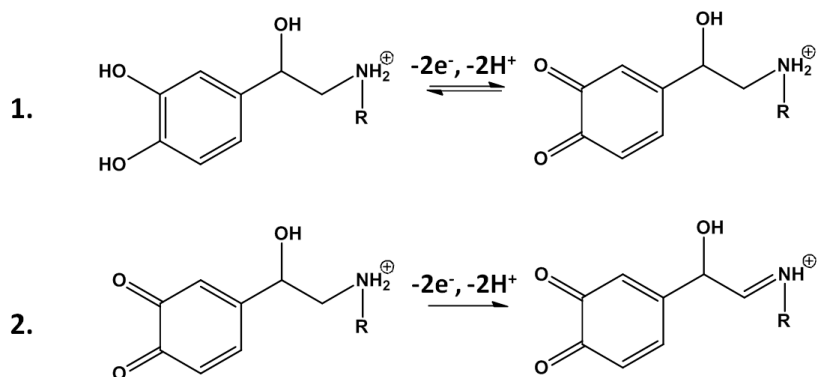


Figure 4.11 Norepinephrine and epinephrine can be distinguished voltammetrically. A) 10 μM norepinephrine. B) 10 μM epinephrine.

Scheme 4.1 Electrochemical reactions for norepinephrine and epinephrine.



R = CH₃ for epinephrine, R = H for norepinephrine

Using this extended waveform, voltammetric data were collected using FSCV and nanocone electrodes inside the confines of the chromaffin cell membrane. Representative data are shown in Figure 4.12 that highlight the electrochemical events observed. Current versus time traces were extracted from these data at two different potentials (+0.65 and +1.425 V). By comparing the peaks generated at these potentials it is possible to distinguish between the two catecholamine species. Events that generated current at both potentials indicated the presence of epinephrine, whereas events that generated current only at +0.65 V corresponded to norepinephrine containing vesicles. The concentration versus time traces show that many of the events are recorded at both potentials in this cell, indicating the presence of many epinephrine-containing vesicles. For example, the event marked by the red square is evident at both potentials. The extracted voltammogram shows the two oxidation peaks that indicate the oxidation of epinephrine (Figure 4.12 C). By contrast, the event marked by the blue square does not have a corresponding peak at +1.425 V. The

voltammogram taken from this time point is displayed in Figure 4.12 B and verifies that the event was generated from the oxidation of norepinephrine. It is interesting to note that in a cell where most of the norepinephrine has been converted to epinephrine by the PNMT enzyme, there still remains a store of intracellular norepinephrine that has not been converted.

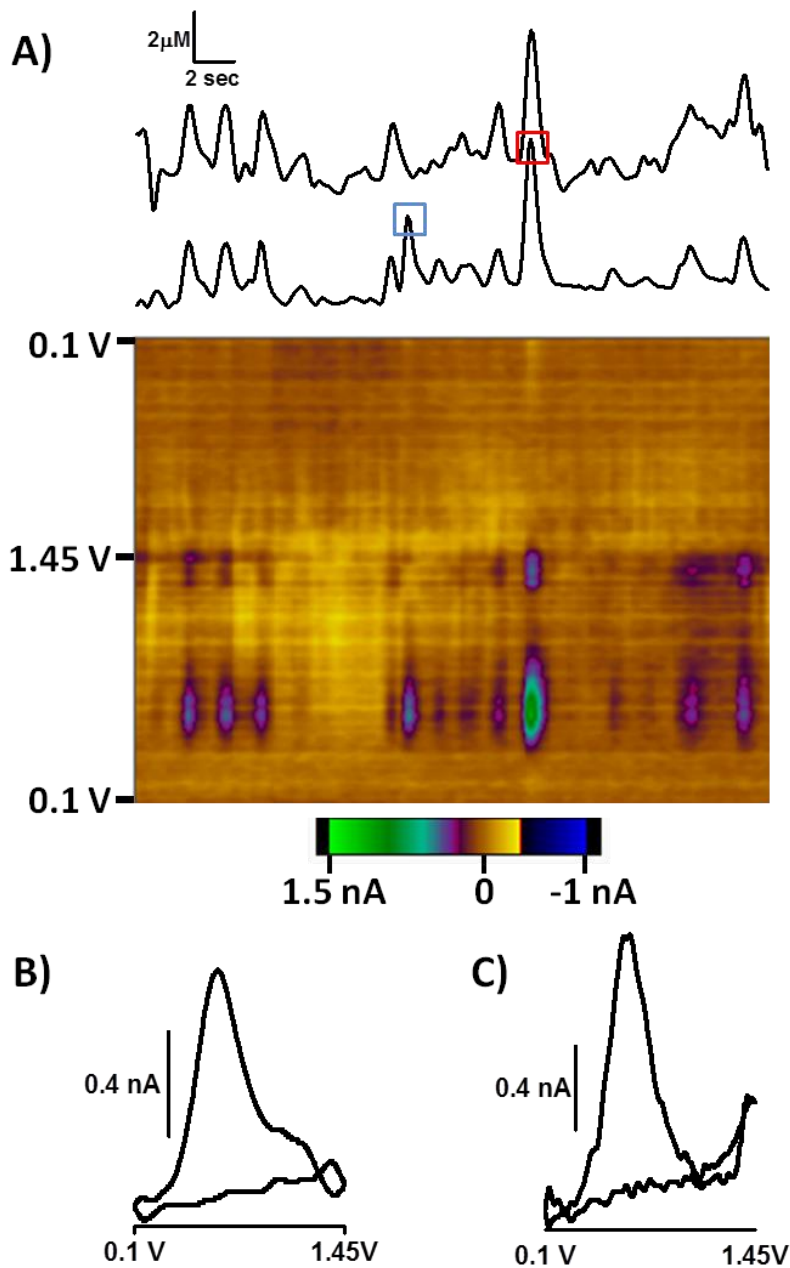


Figure 4.12 Chemical identification and quantification of intracellular vesicle content. A) Representative colorplot showing voltammetry collected intracellularly. Concentration vs. time traces are shown above the color plot, top: extracted at +1.45 V, bottom: extracted at +0.65 V. Spikes observed in the top trace correspond to vesicular epinephrine. Voltammograms extracted from the color plot are shown for B) norepinephrine and C) epinephrine, collected at the time points marked by the blue and red squares respectively.

The area under each peak was used to determine the charge associated with detection of norepinephrine and epinephrine. A histogram showing the distribution of charge for epinephrine and norepinephrine is shown in Figure 4.13. The Gaussian fit for norepinephrine has a mean of 2.24 ± 0.04 pC and the fit for epinephrine has a mean of 2.05 ± 0.06 pC. Based on these averages, norepinephrine accounted for approximately 61% of the released content. These data are in agreement with previous data that reported that both norepinephrine and epinephrine are released from a random sample of chromaffin cells.¹⁶ It is not clear at this point if the norepinephrine arises from individual vesicles lacking PNMT, however, this will be the subject of future work.

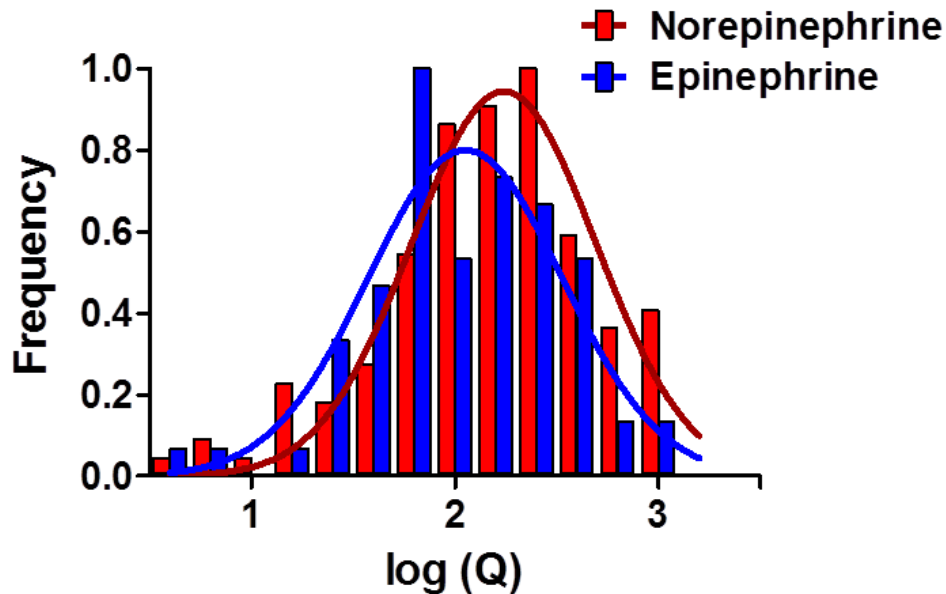


Figure 4.13 Intracellular norepinephrine and epinephrine contents. Histogram of $\log(Q)$ distribution for epinephrine (N=71 events) and norepinephrine (N=122 events) containing vesicles.

4.4 Conclusions

Nanocone carbon fiber microelectrodes were successfully fabricated and utilized for intracellular measurements to both identify and quantify vesicular content. By employing a wet etching technique, traditional cylinder carbon fibers were etched into a conical geometry with nanometer dimensions. This reduced dimensionality allowed the electrode to penetrate the cell wall and enter the cytoplasm. The length of exposed surface area was regulated with an elegant masking procedure and a bilayer insulation provided stable performance. The fabrication procedure allows the user to tailor the length of the electrode tip, for instance to investigate smaller cells. By coupling these electrodes with FSCV, intracellular vesicle content was measured with chemical selectivity for the first time. It was determined that approximately 61% of the vesicle neurotransmitter content corresponded to norepinephrine, over epinephrine. This technique can potentially be used to provide spatially resolved information on vesicular content within the cell, or to measure chemical transport across the cell membrane. It can reveal intracellular chemical dynamics associated with manipulation using a variety of pharmacological agents. Thus, this research provides a new tool that will help answer difficult questions that haven't been challenged due to technological hurdles.

4.5 References

1. Travis, E. R., and Wightman, R. M. (1998) Spatio-temporal resolution of exocytosis from individual cells, *Annual review of biophysics and biomolecular structure* 27, 77-103.
2. Chen, G., and Ewing, A. G. (1997) Chemical analysis of single cells and exocytosis, *Critical reviews in neurobiology* 11, 59-90.
3. Kim, D., Koseoglu, S., Manning, B. M., Meyer, A. F., and Haynes, C. L. (2011) Electroanalytical eavesdropping on single cell communication, *Anal Chem* 83, 7242-7249.
4. Mellander, L. J., Trouillon, R., Svensson, M. I., and Ewing, A. G. (2012) Amperometric post spike feet reveal most exocytosis is via extended kiss-and-run fusion, *Sci Rep* 2, 907.
5. Sudhof, T. C., and Rizo, J. (2011) Synaptic vesicle exocytosis, *Cold Spring Harbor perspectives in biology* 3.
6. Schulte, A., and Schuhmann, W. (2007) Single-cell microelectrochemistry, *Angewandte Chemie* 46, 8760-8777.
7. Lau, Y. Y., Wong, D. K. Y., and Ewing, A. G. (1993) Intracellular Voltammetry at Ultrasmall Platinum-Electrodes, *Microchem J* 47, 308-316.
8. Li, X., Majdi, S., Dunevall, J., Fathali, H., and Ewing, A. G. (2015) Quantitative measurement of transmitters in individual vesicles in the cytoplasm of single cells with nanotip electrodes, *Angewandte Chemie* 54, 11978-11982.
9. Dimitrievski, K., and Kasemo, B. (2008) Simulations of lipid vesicle adsorption for different lipid mixtures, *Langmuir* 24, 4077-4091.
10. Dunevall, J., Fathali, H., Najafinobar, N., Lovric, J., Wigstrom, J., Cans, A. S., and Ewing, A. G. (2015) Characterizing the Catecholamine Content of Single Mammalian Vesicles by Collision-Adsorption Events at an Electrode, *Journal of the American Chemical Society* 137, 4344-4346.
11. Travis, E. R., Wang, Y. M., Michael, D. J., Caron, M. G., and Wightman, R. M. (2000) Differential quantal release of histamine and 5-hydroxytryptamine from mast cells of vesicular monoamine transporter 2 knockout mice, *Proc Natl Acad Sci U S A* 97, 162-167.

12. Pihel, K., Hsieh, S., Jorgenson, J. W., and Wightman, R. M. (1998) Quantal corelease of histamine and 5-hydroxytryptamine from mast cells and the effects of prior incubation, *Biochemistry* 37, 1046-1052.
13. Goldstein, M., Fuxe, K., Hokfelt, T., and Joh, T. H. (1971) Immunohistochemical Studies on Phenylethanolamine-N-Methyltransferase, Dopa-Decarboxylase and Dopamine-Beta-Hydroxylase, *Experientia* 27, 951-+.
14. Axelrod, J. (1962) Purification and Properties of Phenylethanolamine-N-Methyl Transferase, *J Biol Chem* 237, 1657-&.
15. Cooper, B. R., Jankowski, J. A., Leszczyszyn, D. J., Wightman, R. M., and Jorgenson, J. W. (1992) Quantitative-Determination of Catecholamines in Individual Bovine Adrenomedullary Cells by Reversed-Phase Microcolumn Liquid-Chromatography with Electrochemical Detection, *Analytical Chemistry* 64, 691-694.
16. Ciolkowski, E. L., Cooper, B. R., Jankowski, J. A., Jorgenson, J. W., and Wightman, R. M. (1992) Direct Observation of Epinephrine and Norepinephrine Cosecretion from Individual Adrenal-Medullary Chromaffin Cells, *Journal of the American Chemical Society* 114, 2815-2821.
17. Pihel, K., Schroeder, T. J., and Wightman, R. M. (1994) Rapid and Selective Cyclic Voltammetric Measurements of Epinephrine and Norepinephrine as a Method to Measure Secretion from Single Bovine Adrenal-Medullary Cells, *Analytical Chemistry* 66, 4532-4537.
18. Troyer, K. P., and Wightman, R. M. (2002) Temporal separation of vesicle release from vesicle fusion during exocytosis, *J Biol Chem* 277, 29101-29107.
19. Lau, Y. Y., Chien, J. B., Wong, D. K. Y., and Ewing, A. G. (1991) Characterization of the Voltammetric Response at Intracellular Carbon Ring Electrodes, *Electroanalysis* 3, 87-95.
20. Meulemans, A., Poulain, B., Baux, G., Tauc, L., and Henzel, D. (1986) Micro Carbon Electrode for Intracellular Voltammetry, *Analytical Chemistry* 58, 2088-2091.
21. Kawagoe, K. T., Zimmerman, J. B., and Wightman, R. M. (1993) Principles of Voltammetry and Microelectrode Surface-States, *Journal of Neuroscience Methods* 48, 225-240.
22. Strein, T. G., and Ewing, A. G. (1992) Characterization of Submicron-Sized Carbon Electrodes Insulated with a Phenol Allylphenol Copolymer, *Analytical Chemistry* 64, 1368-1373.

23. Plattner, H., Artalejo, A. R., and Neher, E. (1997) Ultrastructural organization of bovine chromaffin cell cortex - Analysis by cryofixation and morphometry of aspects pertinent to exocytosis, *J Cell Biol* 139, 1709-1717.
24. Strand, A. M., and Venton, B. J. (2008) Flame etching enhances the sensitivity of carbon-fiber microelectrodes, *Analytical Chemistry* 80, 3708-3715.
25. Huang, W. H., Pang, D. W., Tong, H., Wang, Z. L., and Cheng, J. K. (2001) A method for the fabrication of low-noise carbon fiber nanoelectrodes, *Analytical Chemistry* 73, 1048-1052.
26. Kawagoe, K. T., Jankowski, J. A., and Wightman, R. M. (1991) Etched Carbon-Fiber Electrodes as Amperometric Detectors of Catecholamine Secretion from Isolated Biological Cells, *Analytical Chemistry* 63, 1589-1594.
27. Robinson, D., Hermans, A., Seipel, A., and Wightman, R. (2008) Monitoring rapid chemical communication in the brain, *Chemical Reviews* 108, 2554-2584.
28. Bard, A. J. F., L. R. (2001) *Electrochemical methods : fundamentals and applications*, 2nd ed., John Wiley, New York.
29. Ramsson, E. S., Cholger, D., Dionise, A., Poirier, N., Andrus, A., and Curtiss, R. (2015) Characterization of Fast-Scan Cyclic Voltammetric Electrodes Using Paraffin as an Effective Sealant with In Vitro and In Vivo Applications, *Plos One* 10.
30. Heien, M., Phillips, P., Stuber, G., Seipel, A., and Wightman, R. (2003) Overoxidation of carbon-fiber microelectrodes enhances dopamine adsorption and increases sensitivity, *Analyst* 128, 1413-1419.
31. Roberts, J., Moody, B., McCarty, G., and Sombers, L. (2010) Specific Oxygen-Containing Functional Groups on the Carbon Surface Underlie an Enhanced Sensitivity to Dopamine at Electrochemically Pretreated Carbon Fiber Microelectrodes, *Langmuir* 26, 9116-9122.

CHAPTER 5

A Double Voltammetric Waveform for Distinguishing Overlapping Signals from pH and Hydrogen Peroxide

This work was completed in collaboration with: Toups, J.V., Eyuaem, E., and Sombers, L.A.

5.1 Introduction

One of the challenges with using FSCV *in vivo* arises from changes in extracellular pH that occur from metabolic and neuronal activity.^{1, 2} The reason changes in local pH produce a challenge to measurements is that the altered environment leads to measurable changes in current that can interfere with other analytes of interest. Shifts in pH are found ubiquitously across the brain and produce characteristic cyclic voltammograms by which they can be identified.³ It is common to observe pH shifts when stimulating a particular region either behaviorally or electrically.⁴ While the presence of a pH shift might indicate some level of brain activity, the current that it generates often masks that generated by other analytes of interest such as dopamine. Indeed this is the case with the voltammetric detection of Hydrogen peroxide (H₂O₂).

H₂O₂ is a reactive oxygen species (ROS) endogenously created in oxygen metabolism and cellular respiration. ROS are usually maintained at safe levels and are part of our body's normal homeostasis.⁵ H₂O₂ is involved in many chemical signaling pathways that regulate biological processes ranging from embryonic cell development to cell death.⁶⁻⁸ The

mitochondrial electron transport chain is the most common pathway for the formation of H_2O_2 and other ROS. The release of electrons can reduce molecular oxygen to form the reactive superoxide ion.⁵ Expression of superoxide is regulated through the enzyme superoxide dismutase which converts superoxide into H_2O_2 .⁵ To prevent buildup of H_2O_2 in tissue enzymes such as glutathione (GSH) peroxidase and catalase convert H_2O_2 into H_2O and oxygen.⁵ However, various triggers can increase the levels of ROS present in tissue and can lead to oxidative stress. This can have damaging effects on cells and has been implicated in a number of neurological disorders including Parkinson's disease.^{9, 10}

H_2O_2 has also been shown to play a neuromodulatory role in the brain. For instance, H_2O_2 produced from glutamatergic activation of medium spiny neurons acts as a neuromodulator of dopamine release in the striatum.^{5, 11, 12} An increase in the levels of H_2O_2 opens K_{ATP} channels on local dopamine dendrites which inhibit dopamine release. Conversely, when H_2O_2 production is attenuated K_{ATP} channels close, which leads to greater dopamine release.¹¹

Due to the ranging impact that H_2O_2 has on biological function it is important to be able to study this molecule in tissue. The challenge is that H_2O_2 has a short lifespan in tissue before degradation and its regulation of dopamine occurs on a sub second time scale.^{12, 13} This limits the number of methods available for measuring this molecule. Fluorescence has been used to successfully monitor H_2O_2 but there are selectivity concerns for other ROS when using conventional probes.¹⁴ FSCV has been demonstrated as a powerful tool for monitoring and quantifying H_2O_2 in tissue.¹³ However, signal from pH shift, if present, will overlap and obscure the H_2O_2 signal.

One method that is commonly employed to separate overlapping signals in complex data is principle component regression (PCR).¹⁵⁻¹⁸ PCR is a multivariate chemometric technique that combines principle component analysis with inverse least-square regression. For this technique, a training set is first compiled that consists of the analytes being studied at known concentrations. This information is then transformed into principle components (PCs) which contain information for both the analytes of interest and the noise in the system. PCs containing information related to the analytes are kept and other PCs that contain noise information are discarded. A model using the relevant PCs is then calibrated to reference concentrations. A data set containing unknown concentrations of the analytes can then be analyzed by projecting the data onto the PCs and using the model to determine individual chemical concentrations.¹⁷

A key point when using this approach is assembling an adequate training set. When a proper training set is compiled this technique can be very powerful. However, if the data in the training set do not adequately represent the individual components of the unknown sample then the final results are erroneous.¹⁸ It can be difficult to compile a training set from *in vivo* data because voltammograms for an analyte of interest often suffer from interferences, such as pH shift. It is also difficult to use *in vitro* voltammograms because it is not uncommon for there to be differences between voltammograms for species collected *in vivo* and *in vitro*. This is due to the effects of the buffer used *in vitro*, which does not exactly replicate the fluid found *in vivo*. For this reason *in vitro* data is precluded from training sets.¹⁹ Therefore, having other methods available for deconvoluting complex data is desirable. In the work presented here, a double waveform is used to distinguish H₂O₂ in the

presence of pH shift. This approach exploits the inherent differences in the voltammograms for pH shift and H₂O₂, enabling the pH shift signal to be subtracted. Thus, the much smaller changes in faradaic current resulting from the redox activity of H₂O₂ are revealed.

5.2 Experimental Section

5.2.1 Chemicals

All chemicals were purchased from Sigma Aldrich Co. (St. Louis, MO) and were used without additional processing. Unless otherwise noted, electrochemical experiments were carried out in Tris buffered electrolyte (15 mM Tris, 3.25 mM KCl, 1.20 mM CaCl₂, 1.2 mM MgCl₂, 2 mM Na₂SO₄, 1.25 mM NaH₂PO₄, and 145 mM NaCl) with a pH of 7.4. Aqueous solutions were made using doubly deionized water (Barnstead Easy Pure II, Dubuque, IA).

5.2.2 Electrode Fabrication

Cylindrical carbon-fiber microelectrodes were constructed using t-650 fibers with a diameter of approximately 7.5 μm. A single carbon fiber was aspirated into a glass capillary (1.0 mm x 0.5 mm, A-M Systems, Carlsburg, WA) and a micropipette puller was used (Narishige, Tokyo, Japan) to form a tapered seal. The carbon fiber was then cut at using a scapel to approximately 100 μm in length. An electrolyte solution (4 M potassium acetate, 150 mM KCl) was used to backfill the electrode and a lead was inserted to establish an electrical connection with the fiber.

5.2.3 Flow Injection

Electrochemical data were collected using a flow injection apparatus that was housed within a custom built Faraday cage to reduce interference from outside noise. The working electrode was positioned in the electrochemical cell using a micromanipulator (World Precision Instruments, Inc., Sarasota, FL). Buffered electrolyte was passed continuously over the working and reference electrode at 1 mL/min using a syringe pump (New Era Pump Systems, Inc., Wantagh, NY). Two second bolus injections of analyte across the working electrode were made by using a digital valve interface (Valco Instruments Co., Inc., Houston, TX) to control an air actuator connected to a six-port HPLC valve.

5.2.4 Electrochemical Data Acquisition

All potentials were reported versus a Ag/AgCl reference electrode. Analyte detection was accomplished using triangular waveforms applied at 400 V/s with an application frequency of 10 Hz. A lower potential limit of -0.4 V and upper potential limit of +1.4 V was used. Experiments with a double waveform utilized two separate upper potential limits. The lower potential limit was -0.4 V. The potential was then raised to +0.8 V and lowered back to -0.4 for 12ms before raising the potential to +1.4 V and lowering it back to -0.4 V. Triangular waveform potentials were applied and current transduction was accomplished using custom instrumentation (University of North Carolina at Chapel Hill, Department of Chemistry, Electronics Facility). Waveforms were output using a DAC/ADC card (NI 6251 M) with TH-1 software (ESA, Chelmsford, MA). The flow injection system was coordinated

with the electrochemical experiment using a second card (NI 6711). Background subtraction and signal averaging was software controlled.

5.2.5 *InVivo* Data Collection

Male Sprague-Dawley rats were purchased from Charles River (Wilmington, MA). They were housed in a temperature and humidity controlled environment. Food and water were given ad libitum and the room was on a 12-hour light/dark cycle. Rats were allowed to habituate to the facility for two days prior to surgery. Sodium urethane (1.5 g/kg i.p.) was used to anesthetize the rats and they were subsequently placed in a stereotaxic frame (Kopf Instrumentation; Tujunga, CA). Body temperature was maintained using a DeltaPhase isothermal pad (Braintree Scientific, Braintree, MA). Bupivacaine was injected under the skin at the skull. The skull was then exposed and bregma and lambda were located in order to drill holes for the electrodes. The working electrodes were positioned in the dorsal striatum (+1.2 AP, +2.0 ML, -4.5—5.5 DV). Ag/AgCl reference electrodes were placed superficially in the contralateral cortex. Prior to experiments the carbon-fiber electrode was conditioned for approximately 30 minutes. Data was collected for 10 minutes prior to infusion and then 10-15 minutes after drug infusion. Rotenone was infused unilaterally at 0.5 $\mu\text{L}/\text{min}$ for 60 seconds using a syringe pump (Kent Scientific Corporation, Torrington, CT). Rotenone was administered through an infusion cannula (33 gauge) that was placed into a guide positioned 50-100 μm away from the working electrode.

5.2.6 Data Analysis

Graphical and statistical analysis was performed with Graph Pad Prism 5 (GraphPad Software, Inc., La Jolla, CA) and Matlab (The Mathworks, Inc., Natick, MA).

5.3 Results and Discussion

5.3.1 H₂O₂ and ΔpH Investigated with Single Waveform Cyclic Voltammetry

With cyclic voltammetry the current collected is plotted against the applied potential to create a voltammogram that has peak shapes characteristic of the analyte being studied. A common waveform used to study hydrogen peroxide begins at a potential of -0.4 V and has a switching potential of +1.4 V.¹³ A representative voltammogram for hydrogen peroxide collected with this waveform is shown in Figure 5.1A. A single peak from the oxidation of H₂O₂ is observed after the switching potential. The reason the peak appears on the back half of the scan arises from filtering processes occurring in both the hardware and software. The characteristic electrochemical response from a basic pH shift is shown in Figure 5.1B. While the general shape of the voltammogram for H₂O₂ is quite different from that of the pH shift, the peak current for both analytes occurs at approximately 1.3 V on the cathodic scan (shown in the dashed box in Figure 5.1). An important feature of voltammetry is that when multiple analytes are present, the current generated at a given potential is equivalent to the sum of the currents produced from the individual analytes. An example voltammogram is shown for a sample containing both H₂O₂ and pH shift in Figure 5.1C. Here it is clear that the voltammogram of the mixture is a combination of the H₂O₂ and pH voltammograms shown previously.

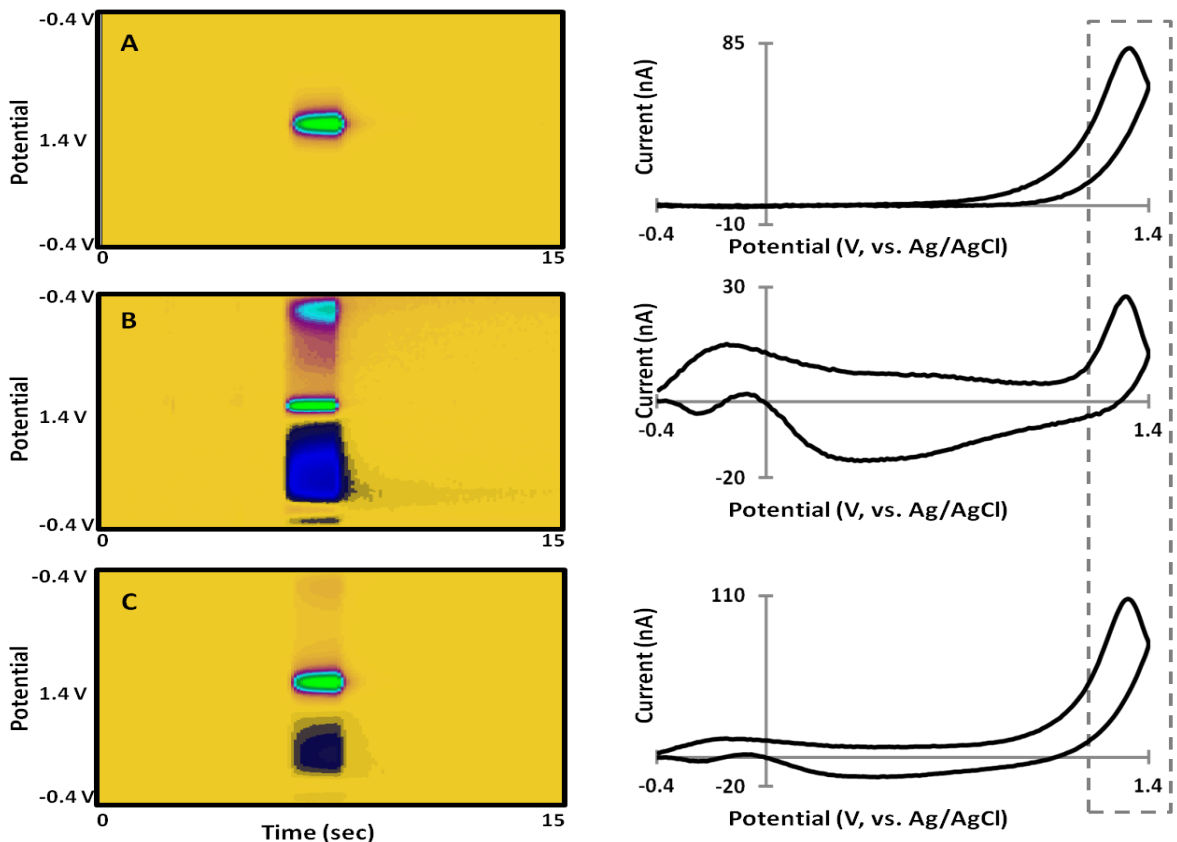


Figure 5.1 Characteristic colorplots and voltammograms for H_2O_2 and ΔpH . (A) H_2O_2 . (B) ΔpH . (C) H_2O_2 and ΔpH . The peaks used for quantifying H_2O_2 and ΔpH overlap as indicated by the dashed box. The currents from the individual samples will add together in a mixture.

With cyclic voltammetry the peak current is directly proportional to the concentration of the analyte being studied. Therefore, a linear relationship between peak current and concentration enables generation of a calibration factor to correlate the measured current to the concentration of the analyte. As shown in Figure 5.2, the peak currents for both H_2O_2 and pH shift are linear with respect to concentration, and thus, the concentration of analyte (H_2O_2 or H^+) can be calculated from an unknown sample. However, if both analytes are detected simultaneously it will be impossible to determine the concentration of the individual species

using a simple calibration. This is because, as stated above, the currents from each analyte are additive. If, however, the current arising from one of the analytes is known, it would be possible to subtract it from the total current to determine what each species contributed. From here it would again be possible to perform a simple calibration to determine the concentration of each component.

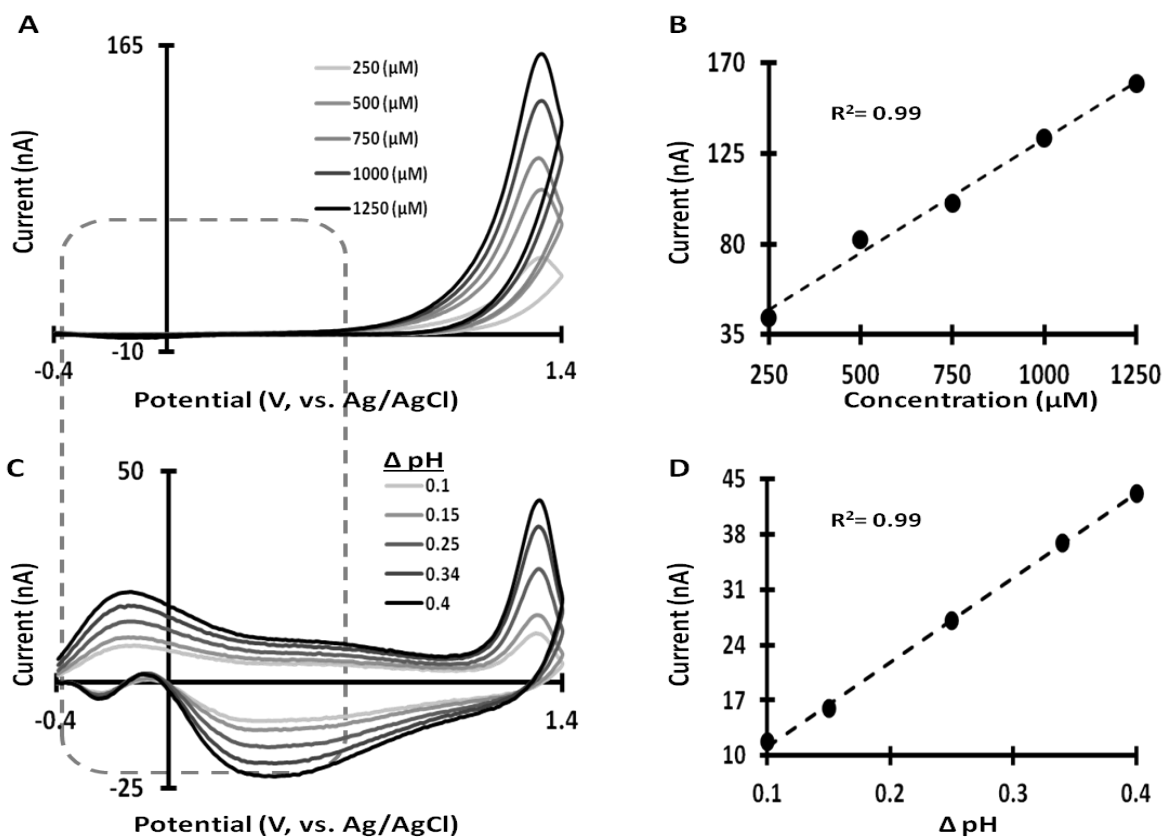


Figure 5.2 Current is linearly related to the amount of species present. (A) Cyclic voltammograms of various concentrations of H_2O_2 . (B) Linear calibration plot of H_2O_2 samples. (C) Cyclic voltammograms of various ΔpH samples. (D) Linear calibration plot of ΔpH samples. The box indicates the region where H_2O_2 is electrochemically inactive and where ΔpH is electrochemically active.

5.3.2 Cyclic Voltammetry with a Double Waveform

Based on the characteristic features in the voltammograms inherent to each species in isolation, we determined that it would be best to develop a model that could calculate the contribution in current from pH. The model we devised uses the information gathered for pH shift at potentials less than 0.8 V to predict what the current from pH would be at the higher potentials. The predicted current could then be subtracted from the total current generated from a mixture of H₂O₂ and pH shift which would leave only the current from H₂O₂.

To collect data for the model, a double waveform was implemented consisting of two consecutive triangular waveforms separated by 12 ms where the electrode is held at -0.4 V. As shown by the dashed box around the voltammograms in Figure 5.2, H₂O₂ is electrochemically silent at potentials below 0.8 V. On the other hand, pH shift produces current and has a characteristic shape at potentials in this region. Thus, the switching potential for the first (small) waveform extends to 0.8 V and the switching potential for the second (large) waveform extends to 1.4 V. Figure 5.3 shows example voltammograms that are generated by both the small and large waveforms for samples of pH shift, H₂O₂, and a mixture of both pH shift and H₂O₂. With the small waveform current is generated from pH and the mixture but any distinguishing redox wave is absent from the H₂O₂ sample. This means that in an unknown sample, any current arising in the smaller waveform is indicative of a pH shift. The second column of voltammograms shows the characteristic responses for pH shift, H₂O₂, and a mixture of both pH shift and H₂O₂ that are generated with the large waveform. These voltammograms resemble those shown in Figure 5.1.

The next step was to train the model by performing a multivariate calibration with only the pH voltammograms to correlate the data collected with the small waveform to each point of the corresponding voltammogram collected using the large waveform. In other words, a linear model is created that treats each point collected with the large waveform from pH shift as a dependent variable and the points in the pH voltammogram collected using the small waveform as independent variables. With the model calibrated in this way, data collected using the small waveform from any sample with pH shift, H₂O₂, or a mixture of the two can be used to predict what the pH contribution to the current would be using the large waveform. The modeled pH shift can then be subtracted out of the actual current collected using the large waveform to leave just the current contribution from H₂O₂. An example of this pH subtraction scheme is shown in the third column of Figure 5.3. For the samples containing just pH shift all of the current is subtracted out leaving no electrochemical response, showing that the model can completely predict the pH shift response collected using the large waveform. The samples with just H₂O₂ show no change after the subtraction, indicating that the model did not predict any current from pH shift in these samples. Finally, the voltammograms for the samples that have both pH shift and H₂O₂ have only the characteristic shape of H₂O₂ after subtraction. This demonstrates that the pH shift component of the sample was successfully subtracted and the residual is just the H₂O₂ component of the sample.

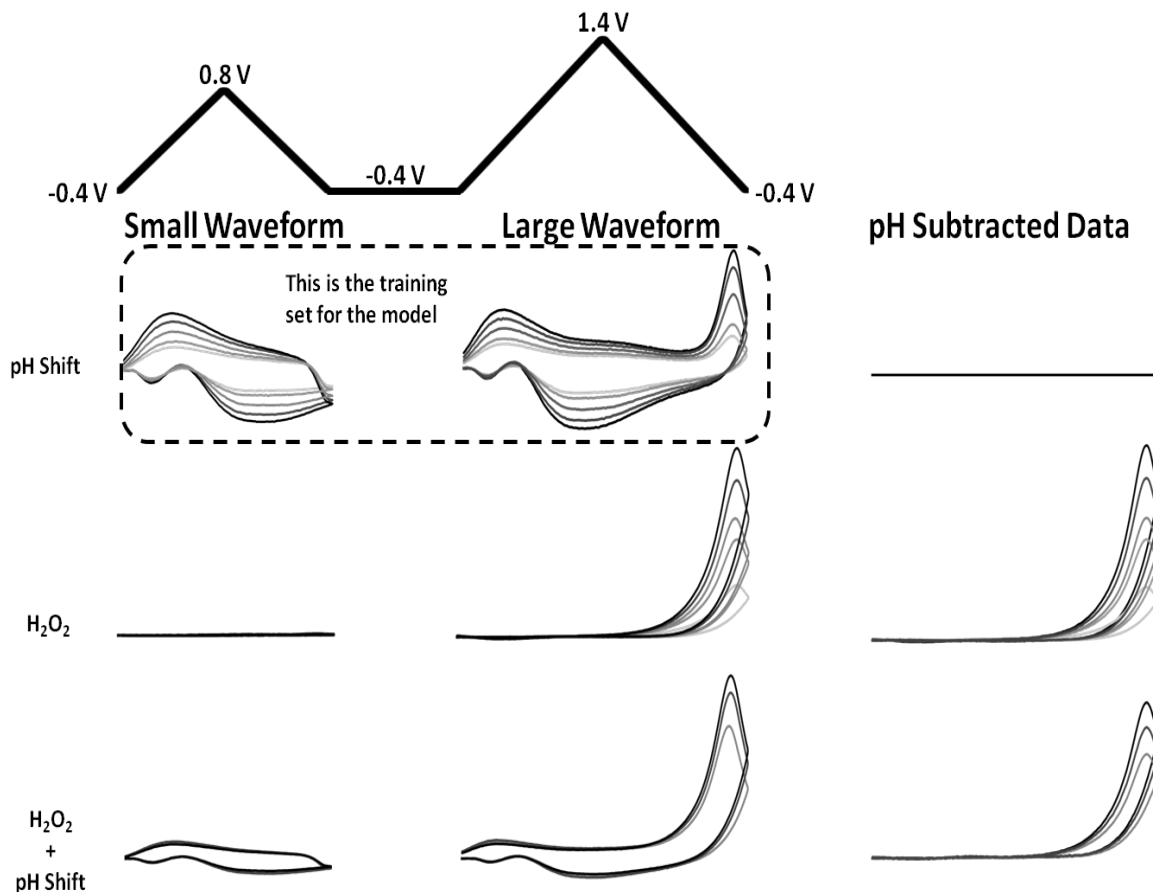


Figure 5.3 Disambiguating H_2O_2 and ΔpH with a double waveform. Current is collected using a waveform ramping from -0.4 to 0.8 V, then 12 ms later using a larger waveform ranging from -0.4 to 1.4 V. The small waveform and large waveform for different analytes is shown. The data from the ΔpH samples is used as a training set to calibrate the model. Information in the small waveform can then be used to predict the current in the large waveform. The predicted current is subtracted out of the actual current leaving just the response due to H_2O_2 . As a result, the ΔpH samples exhibit no final voltammetric shape. Signal from the H_2O_2 sample were left unchanged. The residual voltammograms for $\text{H}_2\text{O}_2 + \Delta\text{pH}$ mixtures show only the H_2O_2 component.

5.3.3 Constructing the Training Set

In order to build a training set from *in vivo* data, a method was devised to select voltammograms from an *in vivo* data set that reflect pH shift only. In Figure 5.4A the plot

shows normalized peak current along the abscissa and normalized current taken from +0.55 V during the forward scan along the ordinate. The points along the voltammogram for a pH shift that were selected are shown as circles on the inset voltammogram. Each point on the plot represents data from distinct pH shift samples. It is evident from the plot that there is a high correlation ($r^2=0.99$) among pH shift voltammograms when these two points are plotted against each other. This tight correlation actually holds true when points are taken from almost anywhere in the waveform.

Figure 5.4B uses color to show the correlation coefficient when currents collected at any two points along the waveform are selected and plotted against one another. Red color indicates a high correlation coefficient and a blue color indicates a low correlation between the points. As indicated by the plot, there is a high degree of correlation at all points along the waveform except at the beginning and ending of the waveform and near the switching potential. The star on the plot represents the intersection of the two points plotted in Figure 5.4A and is in a region where there is a high degree of correlation between all the points.

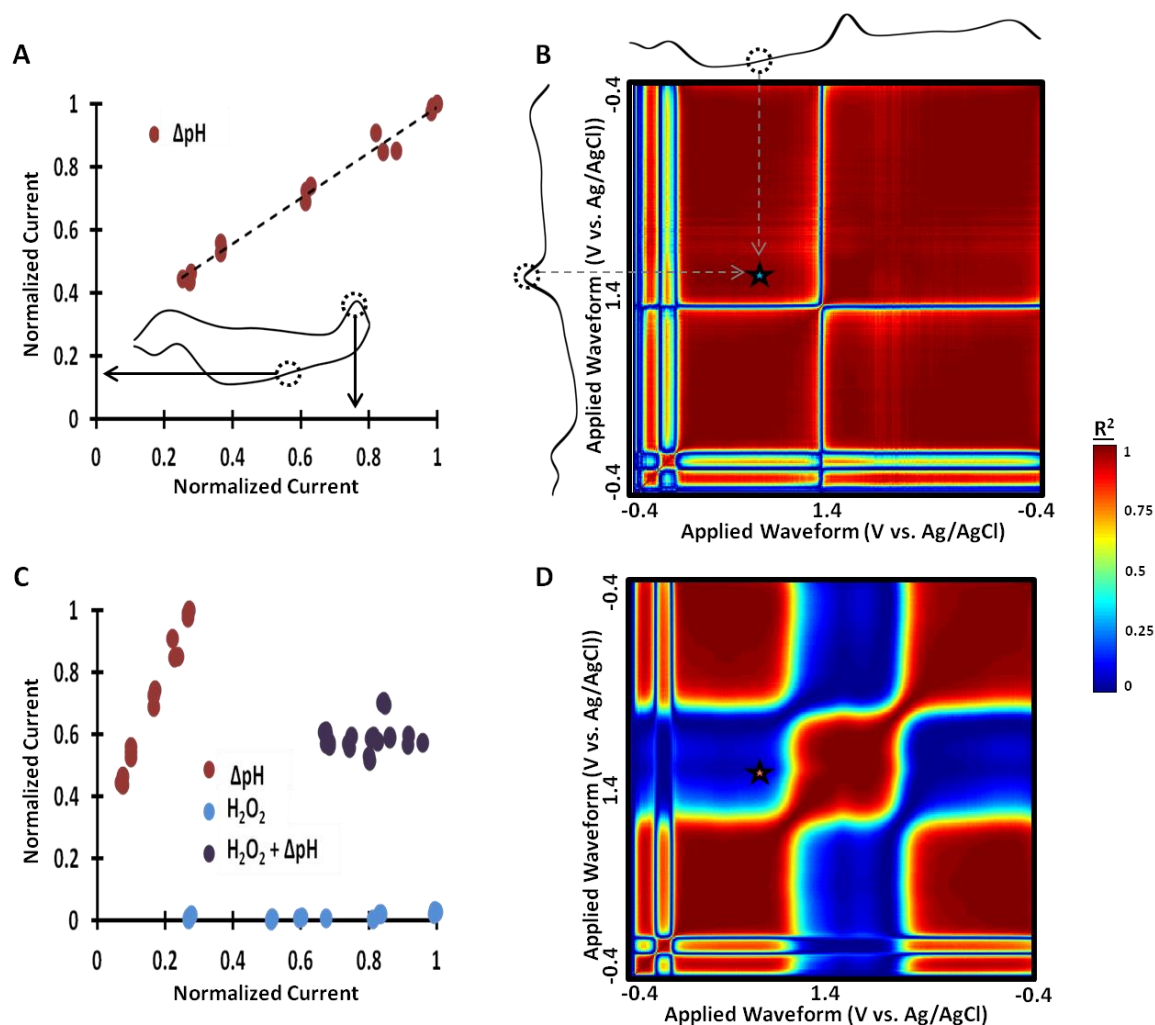


Figure 5.4 Building a training set. (A) Normalized peak current was plotted versus current collected at 0.55 V on the anodic scan for pH voltammograms collected using the larger waveform. Each point represents a different voltammogram. The circles on the inset voltammogram show what points current was taken from and which axis they were plotted against. (B) The correlation coefficient has been plotted as false color to show how every point along the waveform is related for ΔpH samples. The star indicates where the two points plotted in A would lie on this plot. (C) Same as A but now voltammograms for H_2O_2 and $\text{H}_2\text{O}_2 + \Delta\text{pH}$ have been added. (D) Same as B but now including data from H_2O_2 and $\text{H}_2\text{O}_2 + \Delta\text{pH}$. The star now lies in a blue region indicating little correlation between the samples.

Figures 5.4C-D are the same as Figures 5.4A-B except that data from samples containing just H₂O₂ and a mixture of H₂O₂ and pH shift have also been included. What is evident at first glance is that there is much more scatter among the points. The points in Fig. 8C have been color coded to show which ones were taken from pH shift, H₂O₂, and H₂O₂ and pH shift mixture samples. From this it is easy to see how data from each type of sample clusters and can be distinguished from other types of samples. The pH shift voltammograms are tightly grouped in the upper left portion of the plot. The mixed H₂O₂ + pH shift voltammograms are more to the right because of the addition of current from H₂O₂ to the pH shift current. H₂O₂ voltammograms are along the bottom of the plot because minimal current is generated along the forward scan in the waveform.

These relationships make it possible for the experimenter to classify which voltammograms best represent only pH shift when examining an unknown data set, as in data collected *in vivo*. Figure 5.4D shows that a correlation is absent in mixed samples. The star in Figure 5.4D again shows the intersection of the points chosen along the waveform. The region that was once dominated by a high degree of correlation now shows little correlation as indicated by the blue color.

5.3.4 pH Subtraction Extended to *In vivo* Data

In order to demonstrate the value and validity of this technique it was applied to a data set collected *in vivo*. A carbon-fiber electrode was lowered into the caudate putamen (CPu) of an anesthetized rat. In order to elicit a H₂O₂ response, 500 nM rotenone was microinjected adjacent to the carbon fiber in the CPu. Rotenone is an inhibitor of the

complex 1 electron transport chain found in mitochondria. This inhibition results in an increase in local production of reactive oxygen species, such as H_2O_2 .²⁰ Data collected before (Figure 5.5A-C) and after (Figure 5.5D-F) rotenone injection are shown in Figure 5.5. Each of these color plots is comprised of 300 voltammograms. Color plots both before and after the injection show large streaks indicative of a pH shift present. Indeed, cyclic voltammograms taken from each show characteristic pH shapes (Fig. 9 C,F gray line).

A large set of data was collected during this experiment (not all data is shown); and the voltammograms that best exhibited pH shifts were found using the method described above. Once the training set was compiled, the model was used to remove the pH component from the data. The results are shown in Figure 5.5(B, C, E, F). The color plot before rotenone injection (Figure 5.5B) appears smooth after the pH subtraction scheme, indicating that there was little to no current from H_2O_2 oxidation. Likewise, the extracted cyclic voltammograms (Figure 5.5C black line) show no response. The color plot after the rotenone injection (Figure 5.5E), however, shows oxidative current around the peak potential for H_2O_2 even after subtraction. Extracted voltammograms (Figure 5.5F, black line) confirm the pharmacologically evoked signal is H_2O_2 .

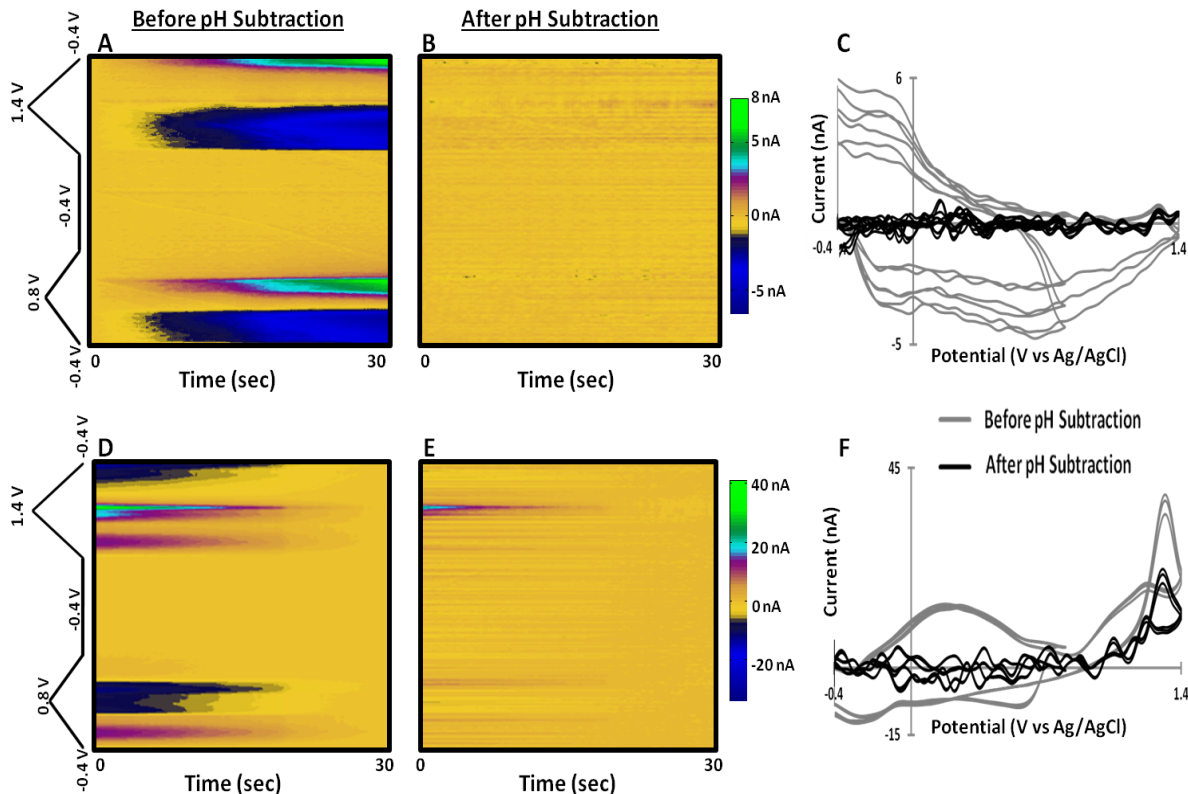


Figure 5.5 Verification of pH subtraction model with *in vivo* data. A-C) Data collected prior to rotenone injection. D-F) Data collected after 500 nM rotenone injection. A,D) Color plots of double waveform with pH components still present. B,E) Colorplots after pH has been subtracted out. C,F) Sample cyclic voltammograms extracted from color plots both before and after pH subtraction. The voltammograms after pH subtraction (black line) show how the pH has been removed from the voltammograms before subtraction (gray line).

5.4 Conclusions

Using cyclic voltammetry, voltammograms can be used to gain qualitative and quantitative information about the analytes. However, if two analytes are present that oxidize or reduce at the same potential, such as ΔpH and H_2O_2 , then the current that each generates will add together, making quantification difficult (Figure 5.5). A double waveform

was presented that was used to collect current from potentials below +0.8V, where only pH was electrochemically active. It was then shown that a multivariate calibration could be used to create a model that correlated the currents collected from the small waveform to those collected from the large waveform. The model was shown to be effective at predicting the pH component present in the large waveform and that current from pH could be subtracted out, leaving only current from H₂O₂ present (Figure 5.3).

Further, we presented a unique method for identifying voltammograms from an unknown data set that represented only pH (Figure 5.4). It was applied to *in vivo* data collected after rotenone administration and shown to be able to subtract current from pH and leave only the H₂O₂ signal (Figure 5.5). The method presented here is not limited only to the analysis of H₂O₂ and pH but should be applicable and easily adapted to the analysis of many other interfering analytes.

5.5 References

1. Chesler, M. (2003) Regulation and modulation of pH in the brain, *Physiol Rev* 83, 1183-1221.
2. Siesjo, B. K. (1972) Symposium on acid-base homeostasis. The regulation of cerebrospinal fluid pH, *Kidney international* 1, 360-374.
3. Takmakov, P., Zachek, M., Keithley, R., Bucher, E., McCarty, G., and Wightman, R. (2010) Characterization of Local pH Changes in Brain Using Fast-Scan Cyclic Voltammetry with Carbon Microelectrodes, *Analytical Chemistry* 82, 9892-9900.
4. Venton, B., Michael, D., and Wightman, R. (2003) Correlation of local changes in extracellular oxygen and pH that accompany dopaminergic terminal activity in the rat caudate-putamen, *Journal of Neurochemistry* 84, 373-381.
5. Rice, M. (2011) H₂O₂: A Dynamic Neuromodulator, *Neuroscientist* 17, 389-406.
6. Groeger, G., Quiney, C., and Cotter, T. (2009) Hydrogen Peroxide as a Cell-Survival Signaling Molecule, *Antioxidants & Redox Signaling* 11, 2655-2671.
7. D'Autreaux, B., and Toledano, M. (2007) ROS as signalling molecules: mechanisms that generate specificity in ROS homeostasis, *Nature Reviews Molecular Cell Biology* 8, 813-824.
8. Coffman, J., Coluccio, A., Planchart, A., and Robertson, A. (2009) Oral-aboral axis specification in the sea urchin embryo III. Role of mitochondrial redox signaling via H₂O₂, *Developmental Biology* 330, 123-130.
9. Orth, M., and Schapira, A. (2002) Mitochondrial involvement in Parkinson's disease, *Neurochemistry International* 40, 533-541.
10. Browne, S., and Beal, M. (2006) Oxidative damage in Huntington's disease pathogenesis, *Antioxidants & Redox Signaling* 8, 2061-2073.
11. Avshalumov, M., Patel, J., and Rice, M. (2008) AMPA receptor-dependent H₂O₂ generation in striatal medium spiny neurons but not dopamine axons: One source of a retrograde signal that can inhibit dopamine release, *Journal of Neurophysiology* 100, 1590-1601.
12. Spanos, M., Gras-Najjar, J., Letchworth, J., Sanford, A., Toups, J., and Sombers, L. (2013) Quantitation of Hydrogen Peroxide Fluctuations and Their Modulation of

- Dopamine Dynamics in the Rat Dorsal Striatum Using Fast-Scan Cyclic Voltammetry, *Acs Chemical Neuroscience* 4, 782-789.
13. Sanford, A., Morton, S., Whitehouse, K., Oara, H., Lugo-Morales, L., Roberts, J., and Sombers, L. (2010) Voltammetric Detection of Hydrogen Peroxide at Carbon Fiber Microelectrodes, *Analytical Chemistry* 82, 5205-5210.
 14. Miller, E., Tulyanthan, O., Isacoff, E., and Chang, C. (2007) Molecular imaging of hydrogen peroxide produced for cell signaling, *Nature Chemical Biology* 3, 263-267.
 15. Keithley, R., Heien, M., and Wightman, R. (2009) Multivariate concentration determination using principal component regression with residual analysis, *Trends in Analytical Chemistry* 28, 1127-1136.
 16. Heien, M., Johnson, M., and Wightman, R. (2004) Resolving neurotransmitters detected by fast-scan cyclic voltammetry, *Analytical Chemistry* 76, 5697-5704.
 17. Keithley, R. B., and Wightman, R. M. (2011) Assessing principal component regression prediction of neurochemicals detected with fast-scan cyclic voltammetry, *ACS Chem Neurosci* 2, 514-525.
 18. Johnson, J. A., Rodeberg, N. T., and Wightman, R. M. (2016) Failure of Standard Training Sets in the Analysis of Fast-Scan Cyclic Voltammetry Data, *ACS Chem Neurosci* 7, 349-359.
 19. Keithley, R., and Wightman, R. (2011) Assessing Principal Component Regression Prediction of Neurochemicals Detected with Fast-Scan Cyclic Voltammetry, *Acs Chemical Neuroscience* 2, 514-525.
 20. Votyakova, T., and Reynolds, I. (2001) Delta psi(m)-dependent and -independent production of reactive oxygen species by rat brain mitochondria, *Journal of Neurochemistry* 79, 266-277.

CHAPTER 6

Summary and Outlook

The introduction of carbon fiber microelectrodes (CFMEs) coupled with fast-scan cyclic voltammetry (FSCV) truly revolutionized the field of neuroscience by opening many new doors for research that were previously closed due to technological limitations. This work describes steps taken to further advance this analytical technique through unique characterization and modification strategies employed on the carbon-fiber microelectrode and manipulations done to the triangular waveform that is traditionally applied.

Chapter 2 highlights the characterization of the surface chemistry of CFMEs in response to applied potential waveforms. Using Raman spectroscopy and scanning electrochemical microscopy, it was shown that static potential waveforms are more effective than dynamic potential waveforms at introducing microstructural changes to the carbon fiber that enhance electrochemical performance. The dynamic nature of the carbon fiber microstructure in response to varying potentials was also demonstrated. This information will aid future researchers in the development of modified waveforms that can be targeted to the detection of specific molecules.

Chapters 3 and 4 describe unique modification strategies on CFMEs that will further advance electrochemical studies done at both brain tissue and at single cells. Chapter 3 details the fabrication steps and characterization of plasma-etched cavity CFMEs. These electrodes displayed enhanced electrochemical performance over traditional CFMEs for both

voltammetric and amperometric measurements as a result of the cavity. In addition, they were shown to provide a more accurate determination of vesicular quantal size than disk CFMEs.

Chapter 4 describes the successful implementation of nanocone CFMEs for intracellular FSCV studies in chromaffin cells. A unique bilayer insulation was used to ensure measurements were excluded from the extracellular environment. Once inserted into the cell cytoplasm, vesicles collided with the electrode surface and lysed, allowing their contents to be measured electrochemically. Using FSCV, norepinephrine and epinephrine content in individual vesicles were successfully distinguished and quantified.

Chapter 5 highlights the development of a unique double waveform that was used to enable separation of voltammetric signals from hydrogen peroxide and pH. The first part of the waveform only extended to +0.8 V, a potential at which electrochemical current is only generated from pH. The second part of the waveform extended to +1.4 V which allowed for the detection of both pH and hydrogen peroxide. A mathematical model was developed that enabled the information collected in the first waveform to be used to predict what the signal contribution from pH would be in the larger waveform. Using the predicted current, the contribution from pH was subtracted from a mixed signal of pH and hydrogen peroxide, leaving current only from the oxidation of hydrogen peroxide.

The work described here unlocks the potential for many future research opportunities. For instance, the characterization strategies employed in Chapter 2 were done on carbon fibers derived from a pitch based source. These strategies could be extended to the characterization of other carbon fiber materials used in FSCV studies, such as those derived

from a polyacrylonitrile source. It is further anticipated that the creation of the cavity and nanocone electrodes will allow for many new and exciting experiments with single cells, such as investigation of intracellular chemical dynamics that occur in response to various pharmacological manipulations. Additionally, the double waveform method used to distinguish overlapping signals of pH and hydrogen peroxide should prove adaptable to the separation of other analytes that have confounding signals. Overall, the findings presented in this work offer researchers many new tools that will enable the continued advance of FSCV for neuroscience applications.

APPENDICIES

APPENDIX A

Supplemental Information to Chapter 3

A.1 Supporting Information

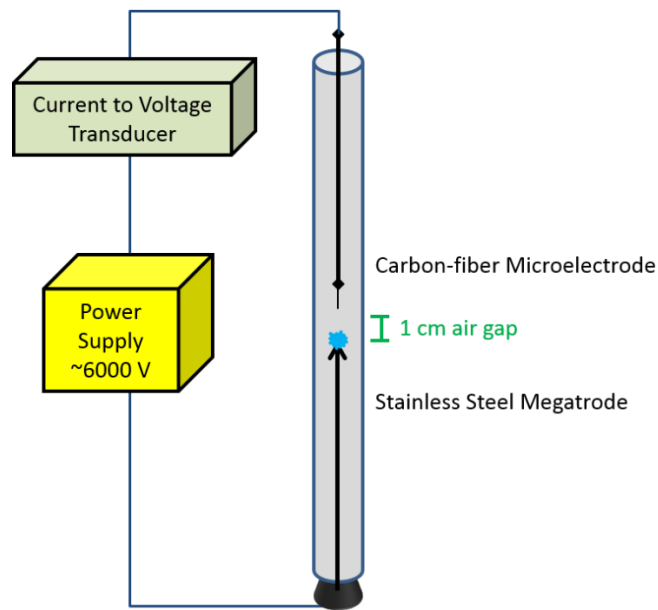


Figure A.1 Plasma etching apparatus. The carbon-fiber electrodes were mounted inside a glass chamber with a ~1 cm tip separation. The DC potential was ramped in 25V increments using a high-voltage power supply, until the desired electrical current was reached. The etch-rate at this potential was constant, and held for a given amount of time to control how far the carbon-fiber recessed.

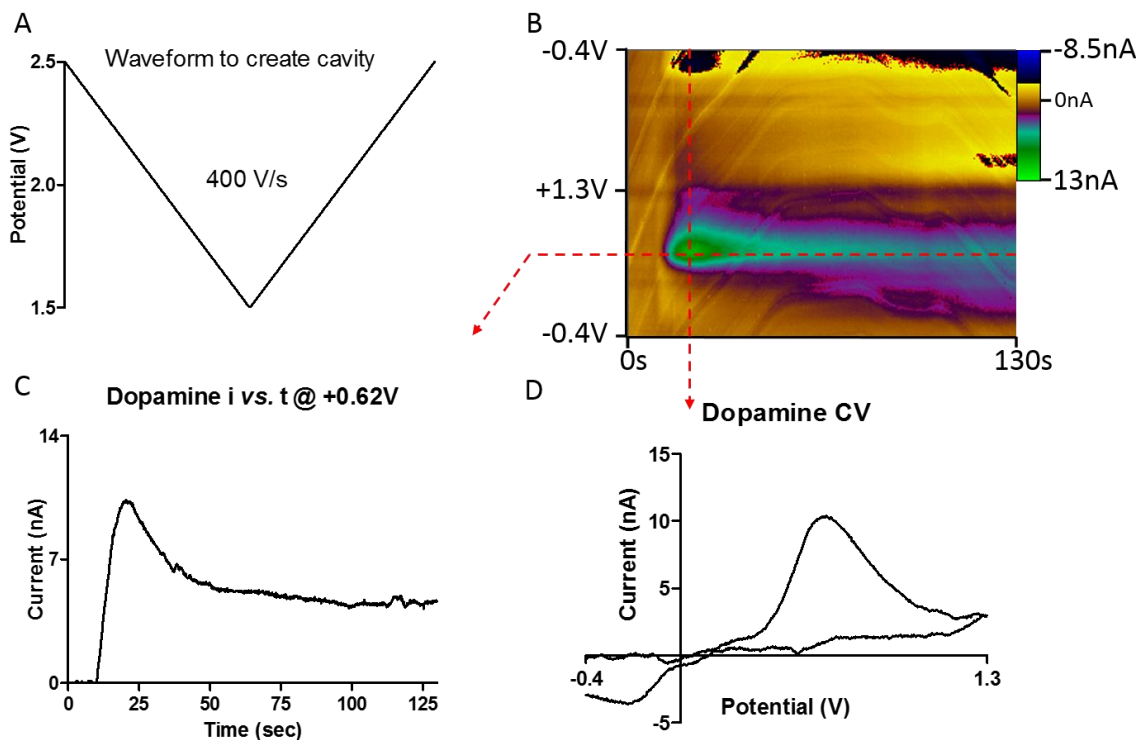


Figure A.2 Cavity carbon-fiber electrodes can be created using FSCV. (A) A holding potential of +2.5 V was applied to the electrode while it was resting in phosphate buffered saline (PBS). The potential was then scanned down to +1.5 V at 400 V/s and back up to +2.5 V repeated at 10 Hz. After successful recession of the carbon-fiber, which was determined through periodical checks with a microscope, the applied waveform was changed to one used for dopamine detection. (B) The potential was held at -0.4 V, then scanned up to +1.3 V before scanning back to -0.4 V at 400 V/s, repeated at 10 Hz. 4 μ M dopamine was then injected and the representative colorplot is shown. (C) The current vs. time trace extracted at peak oxidative current shows the limited diffusion of the analyte in the cavity. (D) The cyclic voltammogram is indicative of successful dopamine detection. However, a significant amount of noise is evident in the colorplot and the extracted current traces. Furthermore, only a few of the electrodes prepared in this manner were reliable enough to use.

APPENDIX B

Characterization of Abiotic Manganese Dioxide Reactivity Using Voltammetry

This work was completed in collaboration with: Uster, B., Sombers, L.A., Duckworth, O.W.

B.1 Introduction

Manganese dioxide (MnO_2) is a naturally occurring mineral that performs many valuable functions. It is found widely in the environment, serves as a strong oxidizing agent, and is even able to adsorb various metals.¹⁻⁶ It has also found use in various industrial applications such as battery electrodes and capacitors.⁷⁻⁹ MnO_2 can be produced through a variety of means including synthetic, bacterial, and fungal pathways. Fungi are unique because they are able to survive in extreme environments and have found use in various industrial applications.^{10, 11} This makes studying mycogenic (generated from fungi) MnO_2 of particular importance.

One of the most important properties of MnO_2 , and metallic minerals in general, that determines its reactivity is its surface chemistry.^{12, 13} Work has been done describing MnO_2 reactivity and surface properties separately, but a cohesive picture of how the two fit together still remains to be put forward. This work aims to begin the process of piecing together our understanding between structure and reactivity by examining the electrochemical properties of several MnO_2 species with varying structures. Since the majority of the reactive sites in MnO_2 are found at its surface, it serves as a useful model to begin unraveling the connection between structure and reactivity.

MnO₂ most commonly exists in a layer structure (phylломanganate) or tunnel structure (tectomanganate).¹⁴ The difference is that phylломanganates consist of Mn octahedra organized in layered sheets whereas tectomanganates contain one or more Mn octahedra chains that share corners which forms tunnels.² In addition to these large differences in crystalline structure, MnO₂ minerals also vary in the number of vacancies present, particle size, and the amount of Mn(III) present. Structural differences also arise from metal doping at various locations on MnO₂. All of these factors are thought to have an impact on the electrical properties of MnO₂ to varying degrees.^{12, 15-17}

Two abiotic manganese dioxides (δ -MnO₂ and c-disordered H⁺-birnessite) were used in this study. Both oxides were phylломanganates, however, the c-disordered H⁺-birnessite, contains a higher amount of Mn(III) than δ -MnO₂. To test the reactivity of the MnO₂ samples, voltammetric measurements were made of manganese oxides that had been cast on the surface of a carbon electrode. Variations in manganese oxide structure were made by doping the oxides with either zinc or arsenic, which bind to different surface sites on the minerals.^{18, 19} Electron transfer properties were again quantified and compared to the undoped samples as a means of relating structure and reactivity. These results are important because having a deeper understanding of the relationships between the structure and reactivity of manganese oxides is the first step in being able to strategically develop new technologies and approaches for environmental remediation systems, batteries and other applications.

B.2 Experimental Section

B.2.1 Chemicals

All chemicals were purchased from either Fisher Scientific or Sigma Aldrich Co. (St. Louis, MO) and used as purchased. Aqueous solutions were made using doubly deionized water (Barnstead Easy Pure II, Dubuque, IA). Unless otherwise stated, electrochemical experiments were carried out in phosphate-buffered saline (0.1 M PBS) at pH 7.4.

B.2.2 Preparation of Manganese Minerals

The MnO₂ minerals were supplied by Owen Duckworth as part of a collaborative effort on this project. The abiotic minerals (δ -MnO₂ and c-disordered H⁺-birnessite) were synthesized following a procedure that has been described elsewhere.²⁰ The one exception is that the final suspension was lyophilized until it was dry before storing in a freezer until further use.

B.2.3 Electrochemical Data Acquisition

All potentials were reported versus a Ag/AgCl (Low profile, 3.5 mm OD, Pine Instruments Company, Durham, NC) reference electrode. A pyrolytic graphite disk (5 mm, Pine Instruments Company, Durham, NC) was used for the working electrode. A platinum wire was used for the counter electrode. Electrochemical data was collected using a Wavedriver potentiostat (Pine Instruments Company, Durham, NC) that was operated with Aftermath software (Version 1.4.7714, Pine Instruments Company).

B.2.4 Data Analysis

Graphical and statistical analysis was performed with Graph Pad Prism 5 (GraphPad Software, Inc., La Jolla, CA) and Excel (Microsoft Office 2007). The formal potential for the different MnO₂ minerals was estimated from the average of the reductive and oxidative peak potentials. All voltammograms shown have been background subtracted.

B.3 Results and Discussion

B.3.1 Preparing the Electrode for Analysis

Electrochemical analysis is able to take place when an analyte comes in contact with an electrode surface and a sufficient potential is applied to drive an oxidation or reduction process. Therefore, in order to perform voltammetric analysis of the MnO₂ samples, it was necessary to adhere the sample to the electrode surface. In general, there are three methods that are pursued for immobilizing nanoparticles to electrode surfaces so they can be analyzed.²² First, nanoparticles can be created by applying a potential to an electrode in a metal ion solution, which can simultaneously form and adhere nanoparticles to the surface. This has been done previously with Mn²⁺ to create MnO₂ at an electrode surface.²³ Alternatively, the previous method can be separated into two steps where the metal ions in solution are first immobilized onto the surface before applying a potential to reduce the ions and form the nanoparticle. A third method, of course, is to try and immobilize nanoparticles created beforehand to the electrode surface. Since we were studying MnO₂ samples produced synthetically and from fungal species, this last method had to be undertaken.

One method that has been used previously to prepare manganese oxides for electrochemical analysis was to combine a graphitic powder with MnO_2 to form a MnO_2 electrode.^{24, 25} Due to sample considerations, this method was not feasible for our experiments. One approach for immobilizing nanoparticles involves functionalizing the electrode surface with a tether that can bind to the nanoparticle,^{26, 27} however, the most straightforward process is to dropcast the sample onto the surface.

Figure B.1 shows the dropcasting procedure we used to prepare a carbon electrode for analysis of MnO_2 samples. After homogenization in a sonicating bath, the sample was placed onto the electrode and a stream of argon gas was passed over sample to accelerate the evaporation process. When the solvent had evaporated off, the nanoparticles were left adhered to the surface. After analysis, the remaining MnO_2 could be easily wiped off to reveal a clean carbon electrode ready for analysis of another sample.

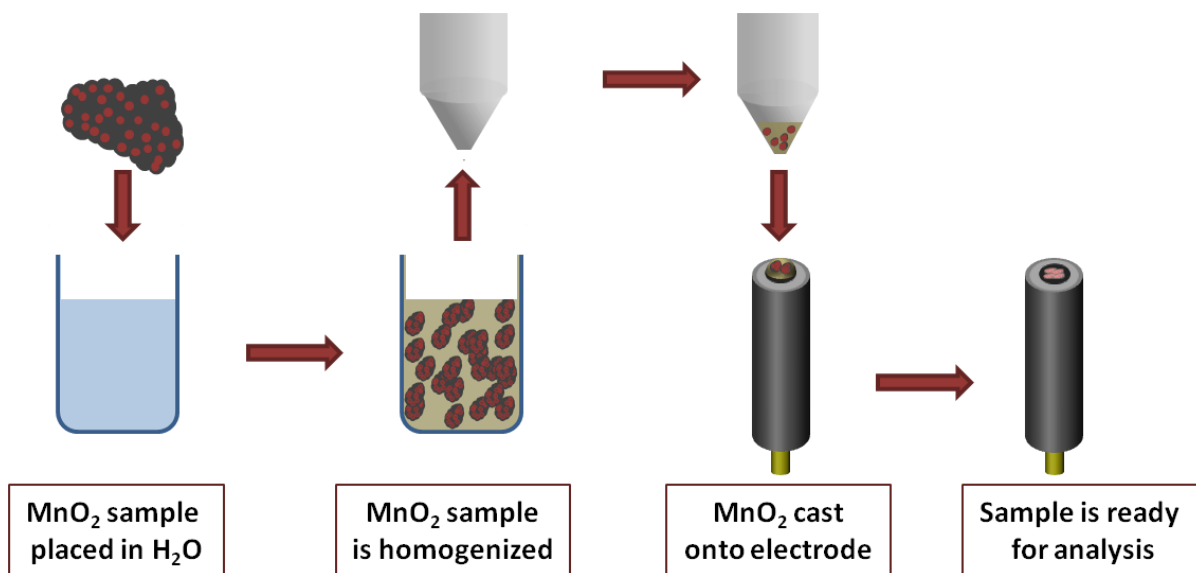


Figure B.1 Diagram depicting the process used to prepare the electrode for analysis of MnO₂. MnO₂ is dispersed in solution and then dropcast on the electrode surface

Voltammograms for both δ -MnO₂ and c-disordered H⁺-birnessite are shown in Figure B.2. As the potential was scanned negatively, a reduction peak was observed for both analytes that corresponds to the reduction of Mn(IV) to Mn(III) occurring through a proton transfer mediated step.²⁸⁻³⁰ Additionally, oxidation back to Mn(IV) was observed on the return scan. The results shown here indicated that the dropcasting method was sufficient for immobilizing MnO₂ to the electrode and that it was possible to perform voltammetry on these abiotic samples.

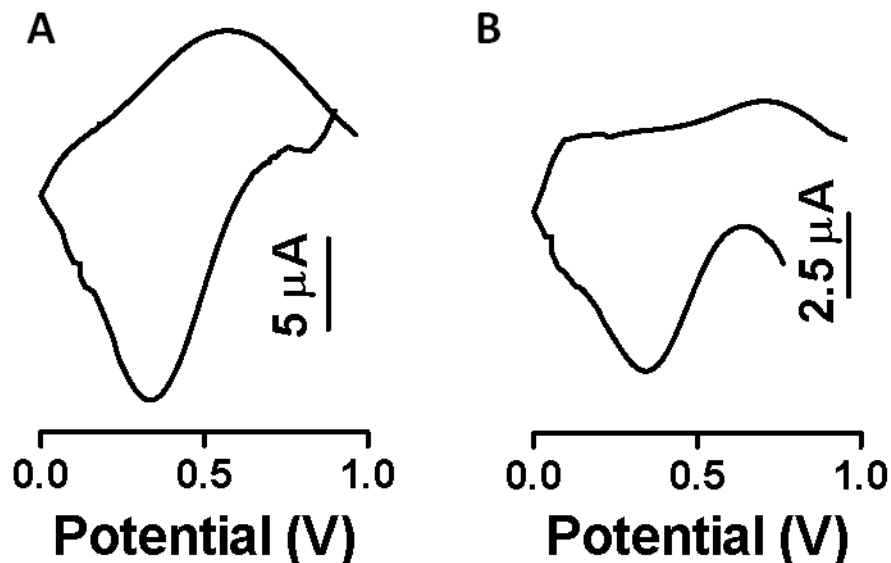


Figure B.2 Electrochemical measurements of manganese oxides. Representative cyclic voltammograms of synthetic MnO₂ samples, A) δ-MnO₂ and B) c-disordered H⁺-birnessite. Voltammograms were collected at 100 mV/s

B.3.2 Verification of the MnO₂ Voltammetric Signal

Additional experiments were done in order to verify that the voltammetric signal arose from the reduction of the MnO₂ and that it was not an artifact in the background. Equation 1 describes the current response of an adsorbed species that results from a voltammetric scan.^{31, 32}

$$\text{Equation 1} \quad i_p = \frac{n^2 F^2}{4RT} v A \Gamma$$

In this equation i_p is the peak current, n is the number of electrons transferred, F is Faradays constant, R is the ideal gas constant, T is the temperature, v is the scan rate, A is the area of the electrode and Γ is the surface coverage of the adsorbed species. If the signal

observed in Figure B.2 arises from MnO₂ adsorbed to the electrode surface, then altering the parameters in Equation 1 should lead to a predictable change in the current response.

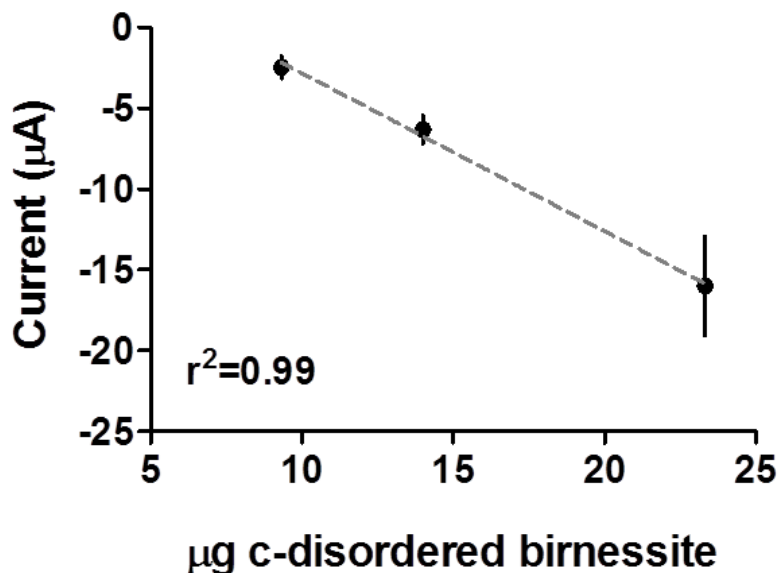


Figure B.3 Current increases linearly with surface coverage. Varying amounts of c-disordered H⁺-birnessite were cast onto the electrode surface and detected with voltammetry at 50 mV/s.

As shown in equation 1, the current generated during reduction of an adsorbed species is directly proportional to the concentration of the species on the electrode surface. To see if this relationship held true for our sample, the quantity of MnO₂ that was dropcast was systematically varied, thereby changing the surface coverage. A linear increase in peak current was observed as the amount of c-disordered H⁺-birnessite cast onto the electrode was

increased, thus following traditional voltammetric behavior for an adsorbed species (Figure B.3).

Additionally, Equation 1 also indicates that current and scan rate should vary linearly. When a consistent amount of c-disordered H⁺-birnessite was cast on the electrode a linear trend was observed between the reduction current and applied scan rate (Figure B.4). These series of tests highlighting traditional electrochemical behavior gave confidence that the observed voltammetric responses arose from the electroactivity of the MnO₂ species at the electrode surface.

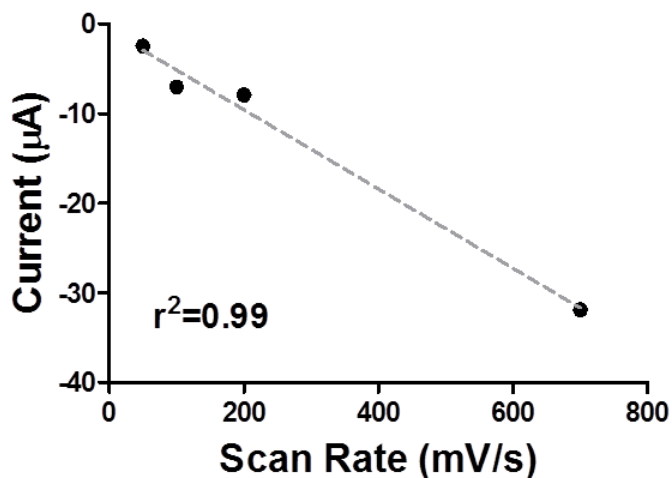


Figure B.4 Reductive current increases linearly with applied scan rate. Analysis was done on c-disordered H⁺-birnessite.

B.3.3 Zinc and Arsenic Doped MnO₂

It is well known that manganese oxides are capable of sorbing metals at different sites on their surface.^{3, 5, 33} Specifically, there are three location where metals are able to sorb;

along edges, at vacancies, or they may be incorporated into the mineral layer.^{18, 34, 35} The sorption of metals at different sites affects both the structure and reactivity of manganese oxides.^{36, 37} For this reason, doping MnO₂ with different metals provides a convenient way of probing their structure to function relationship.

The two metals used here, zinc and arsenic, are thought to bind preferentially to vacancies and edges respectively.^{18, 19} Both of the MnO₂ samples were doped with either zinc or arsenic. Figure B.5 shows voltammograms of c-disordered H⁺-birnessite both with and without metal dopant. Similar reduction and oxidation peaks were observed for the metal doped manganese oxides as for the non-doped oxides except that the peak potentials have shifted, hinting at differences in the reactivity between the samples.

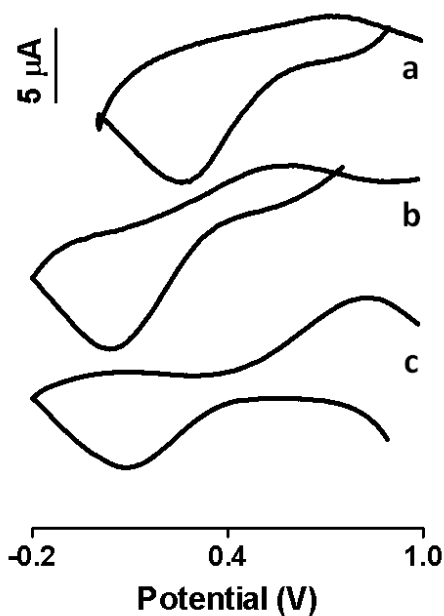


Figure B.5 Voltammetry of metal doped manganese oxides. Representative voltammograms of c-disordered H⁺-birnessite; a) no dopant added, b) Zn doped, c) As doped. Voltammograms were collected with a scan rate of 1 V/s.

B.3.4 Electron Transfer Rate Measurements

To quantitatively compare the reactivity of the different MnO₂ species, calculations of their electron transfer rates (k_{et}) were made using the Laviron method. The Laviron method is a way to mathematically calculate k_{et} for adsorbed species by analyzing the peak position as a function of scan rate.^{32, 38} To employ the Laviron method α , the transfer coefficient of the reaction, must be known, which can be determined through plotting the overpotential versus $\log(\text{scan rate})$. At higher scan rates, the data can be fit with a line that has a slope equal to:

$$\text{Equation 2} \quad \text{slope} = \frac{2.3RT}{\alpha nF}$$

The x-intercept is then used to determine v_c , which can be applied in Equation 3 to determine k_{et} .

$$\text{Equation 3} \quad k_{et} = \frac{\alpha nF v_c}{RT}$$

Figure B.6 shows a plot of $\log(v)$ versus the overpotential for the reduction of c-disordered H⁺-birnessite doped with arsenic. As the scan rate increased, the peak potential continually shifted in a negative direction. Using the method described above, k_{et} was calculated for each manganese oxide sample. The results are tabulated in Table B.1.

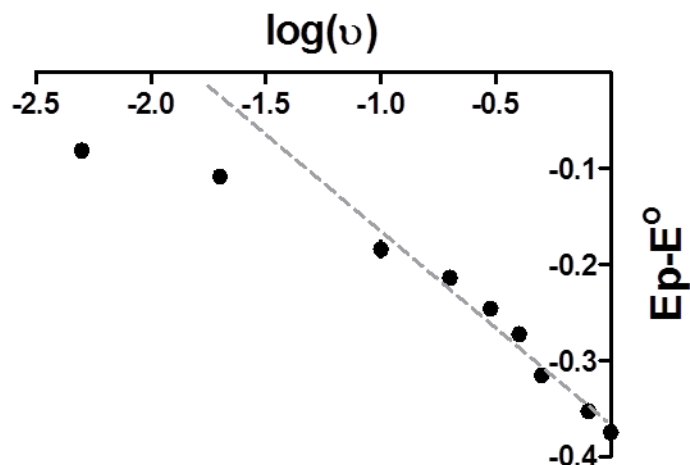


Figure B.6 Peak potential varies with scan rate. Plot of $\log(\text{scan rate})$ versus the overpotential of the reduction of c-disordered H^+ - birnessite doped with As. A line was fitted at higher overpotentials

Based on the calculated values for k_{et} , conclusions could begin to be made concerning the relative reactivity of the different MnO_2 species. The average manganese oxidation number (AMON) for the two manganese oxides is shown in Table B.2. The AMON for δ - MnO_2 is 4.02 indicating that it is virtually absent of Mn(III) whereas c-disordered H^+ -birnessite has a higher content of Mn(III) present (AMON = 3.81). The calculated electron transfer rate for c-disordered H^+ -birnessite is 50 % higher than δ - MnO_2 , suggesting that Mn(III) content may be associated with greater reactivity. In addition to Mn(III) content, comparisons could also be made between the doped and non-doped manganese oxides. It has been suggested previously that vacancies play an important role in the reactivity of MnO_2 , therefore, it is thought that if the vacancies are blocked by a sorbed ion that the electroactivity of the mineral will be reduced.²⁹ As stated above, zinc preferentially binds to vacancies and arsenic binds to edges. While the k_{et} for δ - MnO_2 appears to be affected very

little by the sorbed ions, c-disordered H⁺-birnessite shows greater variation in k_{et} with a 26% decrease when zinc is sorbed and a 38% decrease when arsenic is sorbed, thus suggesting that the reactivity of the minerals is partially controlled through the vacancies and edges. This data will be compared to future studies measuring the kinetics of the manganese oxides through chemical reactions with substituted quinones to see if similar trends in reactivity are observed. In addition, individual manganese oxide samples will be able to be compared in greater detail once computational calculations of mineral structures are complete.

Table B.1 Calculated electron transfer rates for the reduction of abiotic manganese oxides

Sample	Dopant	$k_{\text{et}}(\text{s}^{-1}) (\times 10^{-2})$
δ -MnO ₂	None	28 ± 10
	Zinc	27 ± 13
	Arsenic	25 ± 7
C-disordered H ⁺ -birnessite	None	42 ± 19
	Zinc	31 ± 17
	Arsenic	26 ± 6

Table B.2 Average manganese oxidation numbers for abiotic manganese oxides

Sample	Average Manganese Oxidation Number ³⁹
δ -MnO ₂	4.02
c-disordered H ⁺ -birnessite	3.81

B.4 Conclusions

The results presented here help take an important step forward toward further unlocking the relationship between the structure and reactivity of manganese oxides. It was shown that voltammetry is both possible and effective at investigating the reactivity of abiotic manganese oxides. As discussed, higher amounts of Mn(III) may be correlated with increases in reactivity and both vacancies and edges likely have an important role in reactivity, though the extent of each is not yet clear.

This work is part of an ongoing study that will seek to further advance understanding of the structure-to-reactivity relationship by examining a greater number of manganese oxide

samples and through probing the structural characteristics with finer detail. The foundation is laid out here to extend this work to analysis of mycogenic manganese oxides. By increasing the number of samples with varying structural properties, it will be possible to draw more concrete conclusions about how the structure and reactivity relate. The work presented here is a piece of a larger project that will characterize the manganese oxides more fully through spectroscopic, computational, and chemical reactivity measurements. By incorporating the data collected from this study with what will be collected in other studies, a much clearer picture of how structure is related to manganese oxide reactivity will begin to be pieced together.

B.5 References

1. Jenne, E. A. (1968) Controls on Mn Fe Co Ni Cu and Zn Concentrations in Soils and Water - Significant Role of Hydrrous Mn and Fe Oxides, *Adv Chem Ser*, 337-&.
2. Post, J. E. (1999) Manganese oxide minerals: Crystal structures and economic and environmental significance, *P Natl Acad Sci USA* 96, 3447-3454.
3. Miyata, N., Tani, Y., Sakata, M., and Iwahori, K. (2007) Microbial manganese oxide formation and interaction with toxic metal ions, *J Biosci Bioeng* 104, 1-8.
4. Manceau, A., Lanson, B., and Drits, V. A. (2003) Structure of heavy metal sorbed birnessite. Part III: Results from powder and polarized EXAFS spectroscopy. (vol 66, pg 2639, 2002), *Geochimica Et Cosmochimica Acta* 67, 1599-1599.
5. Goldberg, E. D. (1954) Marine Geochemistry .1. Chemical Scavengers of the Sea, *J Geol* 62, 249-265.
6. Sherman, D. M. (2005) Electronic structures of iron(III) and manganese(IV) (hydr)oxide minerals: Thermodynamics of photochemical reductive dissolution in aquatic environments, *Geochimica Et Cosmochimica Acta* 69, 3249-3255.
7. Thackeray, M. M. (1997) Manganese oxides for lithium batteries, *Prog Solid State Ch* 25, 1-71.
8. Post, J. E., and Heaney, P. J. (2014) Crystal structures of natural manganese oxide minerals, *Abstracts of Papers of the American Chemical Society* 247.
9. Wei, W. F., Cui, X. W., Chen, W. X., and Ivey, D. G. (2011) Manganese oxide-based materials as electrochemical supercapacitor electrodes, *Chem Soc Rev* 40, 1697-1721.
10. Gade, A., Ingle, A., Whiteley, C., and Rai, M. (2010) Mycogenic metal nanoparticles: progress and applications, *Biotechnol Lett* 32, 593-600.
11. Shakya, M., Sharma, P., Meryem, S. S., Mahmood, Q., and Kumar, A. (2016) Heavy Metal Removal from Industrial Wastewater Using Fungi: Uptake Mechanism and Biochemical Aspects, *J Environ Eng* 142.
12. Kwon, K. D., Refson, K., and Sposito, G. (2008) Defect-induced photoconductivity in layered manganese oxides: A density functional theory study, *Phys Rev Lett* 100.

13. Somorjai, G. A., and Li, Y. M. (2011) Impact of surface chemistry, *P Natl Acad Sci USA* 108, 917-924.
14. Santelli, C. M., Webb, S. M., Dohnalkova, A. C., and Hansel, C. M. (2011) Diversity of Mn oxides produced by Mn(II)-oxidizing fungi, *Geochimica Et Cosmochimica Acta* 75, 2762-2776.
15. Kwon, K. D., Refson, K., and Sposito, G. (2009) On the role of Mn(IV) vacancies in the photoreductive dissolution of hexagonal birnessite, *Geochimica Et Cosmochimica Acta* 73, 4142-4150.
16. Ogata, A., Komaba, S., Baddour-Hadjean, R., Pereira-Ramos, J. P., and Kumagai, N. (2008) Doping effects on structure and electrode performance of K-birnessite-type manganese dioxides for rechargeable lithium battery, *Electrochimica Acta* 53, 3084-3093.
17. Hochella, M. F., Lower, S. K., Maurice, P. A., Penn, R. L., Sahai, N., Sparks, D. L., and Twining, B. S. (2008) Nanominerals, mineral nanoparticles, and Earth systems, *Science* 319, 1631-1635.
18. Toner, B., Manceau, A., Webb, S. M., and Sposito, G. (2006) Zinc sorption to biogenic hexagonal-birnessite particles within a hydrated bacterial biofilm, *Geochimica Et Cosmochimica Acta* 70, 27-43.
19. Tani, Y., Miyata, N., Ohashi, M., Ohnuki, T., Seyama, H., Iwahori, K., and Soma, M. (2004) Interaction of inorganic arsenic with biogenic manganese oxide produced by a Mn-oxidizing fungus, strain KR21-2, *Environmental Science & Technology* 38, 6618-6624.
20. Villalobos, M., Toner, B., Bargar, J., and Sposito, G. (2003) Characterization of the manganese oxide produced by *Pseudomonas putida* strain MnB1, *Geochimica Et Cosmochimica Acta* 67, 2649-2662.
21. Toner, B., Fakra, S., Villalobos, M., Warwick, T., and Sposito, G. (2005) Spatially resolved characterization of biogenic manganese oxide production within a bacterial biofilm, *Appl Environ Microb* 71, 1300-1310.
22. Kleijn, S. E. F., Lai, S. C. S., Koper, M. T. M., and Unwin, P. R. (2014) Electrochemistry of Nanoparticles, *Angewandte Chemie-International Edition* 53, 3558-3586.

23. Rodrigues, S., Munichandraiah, N., and Shukla, A. K. (1998) A cyclic voltammetric study of the kinetics and mechanism of electrodeposition of manganese dioxide, *J Appl Electrochem* 28, 1235-1241.
24. Donne, S. W., Lawrance, G. A., and Swinkels, D. A. J. (1997) Redox processes at the manganese dioxide electrode .1. Constant-current intermittent discharge, *Journal of the Electrochemical Society* 144, 2949-2953.
25. Donne, S. W., Lawrance, G. A., and Swinkels, D. A. J. (1997) Redox processes at the manganese dioxide electrode .2. Slow-scan cyclic voltammetry, *Journal of the Electrochemical Society* 144, 2954-2961.
26. Freeman, R. G., Grabar, K. C., Allison, K. J., Bright, R. M., Davis, J. A., Guthrie, A. P., Hommer, M. B., Jackson, M. A., Smith, P. C., Walter, D. G., and Natan, M. J. (1995) Self-Assembled Metal Colloid Monolayers - an Approach to Sensing Substrates, *Science* 267, 1629-1632.
27. Li, Y. X., Cox, J. T., and Zhang, B. (2010) Electrochemical Responses and Electrocatalysis at Single Au Nanoparticles, *Journal of the American Chemical Society* 132, 3047-3054.
28. Athouel, L., Moser, F., Dugas, R., Crosnier, O., Belanger, D., and Brousse, T. (2008) Variation of the MnO₂ birnessite structure upon charge/discharge in an electrochemical supercapacitor electrode in aqueous Na₂SO₄ electrolyte, *Journal of Physical Chemistry C* 112, 7270-7277.
29. Ruetschi, P. (1984) Cation-Vacancy Model for MnO₂, *Journal of the Electrochemical Society* 131, 2737-2744.
30. Ndjeri, M., Peulon, S., Bach, S., and Chausse, A. (2011) Studies on the reduction of birnessite thin layers: Influence of medium, *Electrochimica Acta* 56, 8564-8570.
31. Bard, A. J. F., L. R. (2001) *Electrochemical methods : fundamentals and applications*, 2nd ed., John Wiley, New York.
32. Eckermann, A. L., Feld, D. J., Shaw, J. A., and Meade, T. J. (2010) Electrochemistry of redox-active self-assembled monolayers, *Coordination Chemistry Reviews* 254, 1769-1802.
33. Tebo, B. M., Bargar, J. R., Clement, B. G., Dick, G. J., Murray, K. J., Parker, D., Verity, R., and Webb, S. M. (2004) Biogenic manganese oxides: Properties and mechanisms of formation, *Annual Review of Earth and Planetary Science* 32, 287-328.

34. Duckworth, O. W., Bargar, J. R., and Sposito, G. (2008) Sorption of ferric iron from ferrioxamine B to synthetic and biogenic layer type manganese oxides, *Geochimica Et Cosmochimica Acta* 72, 3371-3380.
35. Manceau, A., Lanson, B., and Drits, V. A. (2002) Structure of heavy metal sorbed birnessite. Part III: Results from powder and polarized extended X-ray absorption fine structure spectroscopy, *Geochimica Et Cosmochimica Acta* 66, 2639-2663.
36. Zhu, M. Q., Farrow, C. L., Post, J. E., Livi, K. J. T., Billinge, S. J. L., Ginder-Vogel, M., and Sparks, D. L. (2012) Structural study of biotic and abiotic poorly-crystalline manganese oxides using atomic pair distribution function analysis, *Geochimica Et Cosmochimica Acta* 81, 39-55.
37. Grangeon, S., Manceau, A., Guilhermet, J., Gaillot, A. C., Lanson, M., and Lanson, B. (2012) Zn sorption modifies dynamically the layer and interlayer structure of vernadite, *Geochimica Et Cosmochimica Acta* 85, 302-313.
38. Laviron, E. (1979) General Expression of the Linear Potential Sweep Voltammogram in the Case of Diffusionless Electrochemical Systems, *Journal of Electroanalytical Chemistry* 101, 19-28.
39. Duckworth, O. W., and Sposito, G. (2007) Siderophore-promoted dissolution of synthetic and biogenic layer-type Mn oxides, *Chem Geol* 242, 497-508.